UNIVERSITY OF CALIFORNIA, SAN DIEGO

Electrohydrodynamics of Particles and Drops in Strong Electric Fields

A dissertation submitted in partial satisfaction of the
requirements for the degree
Doctor of Philosophy

in

Engineering Sciences (Mechanical Engineering)

by

Debasish Das

Committee in charge:

Professor David Saintillan, Chair
Professor Juan C. Lasheras
Professor Bo Li
Professor Jérémie Palacci
Professor Daniel M. Tartakovsky

2016

The Dissertation of Debasish Das is approved, and it is acceptable in quality and form for publication on microfilm and electronically:

_____

_____

_____

_____

_____

Chair

University of California, San Diego

2016

EPIGRAPH

If you keep proving stuff that others have done, getting confidence, increasing the complexities of your solutions - for the fun of it - then one day you'll turn around and discover that nobody actually did that one!

—Richard P. Feynman

TABLE OF CONTENTS

LIST OF FIGURES

LIST OF TABLES

ACKNOWLEDGEMENTS

First and foremost, I would like to thank my research adviser, David Saintillan, for his unwavering support and guidance throughout my graduate studies that began at the University of Illinois, Urbana-Champaign and ended at the University of California, San Diego. I have been very fortunate to have as insightful, patient and helpful an adviser as him. I am grateful to him for not only teaching me the fundamentals of fluid mechanics but also imbuing in me a sense of scientific inquiry and inquisitiveness that will last a lifetime. He has been an excellent role model for me both as a researcher and teacher who takes utmost interest in the learning of his students.

I begin by acknowledging the principle investigators and students who helped me in different ways in the various projects that has culminated in this thesis. I would like to thank Denis Bartolo and Petia Vlahovska for their helpful comments and suggestions on the pair interactions problem. I have also benefited a lot from discussions with Petia Vlahovska, Paul Salipante, Aditya Khair and Javier Lanauze on the drop electrohydrodynamics problem. In particular, I thank Paul Salipante, Hui He and Javier Lanauze for sharing their experimental data with me. I would like to thank Denis Bartolo for sharing his ideas on the collective motion in confinement that eventually led to a very fruitful collaboration and Jean-Baptiste Caussin for coordinating the collaborative efforts between all the contributors. I also wish to thank Jonathan Higdon, Shravan Veerapaneni and Andrew Spann for helpful discussions on the drop electrohydrodynamics boundary element problem.

I am grateful to Juan C. Lasheras, Daniel M. Tartakovsky, Jérémie Palacci and Bo Li for agreeing to serve on my thesis committee. Additionally, I would like to thank Juan C. Lasheras, Juan C. del Alamo and Daniel M. Tartakovsky for their

guidance both from an academic and personal development perspective.

The initial stages of my life as a graduate student would have been much more tumultuous if it was not for Jae Sung's help and supervision. I feel very lucky to have shared my learning space with Harishankar who was always willing to help understand difficult concepts and discuss new ideas. I would like to thank all the past and present members of Saintillan group: Shrenik, Barath, Ku Da, Adrien, Roberto, Maxime B, Maxime T, Brato and Danny.

I am grateful for having wonderful friends, Ankush, Samir and Soumit, and instructors, Prabal Ray and Alok Satapathy, at my undergraduate institute, National Institute of Technology, Roukela. The rigorous course and research work at University of Illinois was palliated by my friends there, mainly, Bhargav, Bindu, Bharat, Jakob and Gustavo. I specially thank Felipe, Carlos and Miguel who are the best roommates that anyone can hope for. I am also thankful to Norman who introduced me to Roundtable house where I lived during most of my graduate studies and met many wonderful people who became my friends making the winters at Illinois less gloomy. After I moved to San Diego, I was lucky to have met Ricardo, Lorenzo and Ernesto who quickly filled the friend's void space. This is a small and by no means an exhaustive list of friends and people who have supported me throughout my life and I am thankful to all of them.

Finally, I am ever grateful to my parents and brother for their support and belief in me at every stage of my life and the tremendous sacrifices they have made to make sure I achieve my dreams and goals.

Chapter 2 is based on the Master's Thesis of Debasish Das (2012) submitted in August 2012 at the University of Illinois, Urbana-Champaign [34] and material that has appeared in Physical Review E (2015), authored by Debasish Das and David Saintillan [35]. The dissertation author was the primary researcher and author of this paper.

Chapter 3 is based on material that has appeared in Nature Communications (2015), authored by Antoine Bricard, Jean-Baptiste Caussin, Debasish Das, Charles Savoie, Vijaykumar Chikkadi, Kyohei Shitara, Oleksandr Chepizhko, Fernando Peruani, David Saintillan and Denis Bartolo [22]. The dissertation author was the third author of this paper.

Chapter 4 is based on material that is under review in Journal of Fluid Mechanics (2016), authored by Debasish Das and David Saintillan [37]. The dissertation author was the primary researcher and author of this paper.

Chapter 5 is based on material that is submitted to Journal of Fluid Mechanics (2016), authored by Debasish Das and David Saintillan [36]. The dissertation author was the primary researcher and author of this paper.

VITA

2009	B. Tech. in Mechanical Engineering, National Institute of Technology, Rourkela (India).
2009-2010	Graduate Engineer Trainee, Research and Development, Mahindra & Mahindra Automotive, Nashik (India).
2010-2013	Graduate Research and Teaching Assistant, University of Illinois, Urbana-Champaign.
2012	M .S. in Mechanical Engineering, University of Illinois, Urbana-Champaign.
2013-2016	Graduate Research Assistant, University of California, San Diego.
2016	Ph. D. in Engineering Sciences (Mechanical Engineering), University of California, San Diego.

ABSTRACT OF THE DISSERTATION

Electrohydrodynamics of Particles and Drops in Strong Electric Fields

by

Debasish Das

Doctor of Philosophy in Engineering Sciences (Mechanical Engineering)

University of California, San Diego, 2016

Professor David Saintillan, Chair

The dynamics of dielectric rigid particles and liquid drops suspended in another liquid medium and subject to a uniform DC electric field, the study of which forms the field of electrohydrodynamics (EHD), has fascinated scientists for decades. This phenomenon is described by the much celebrated Melcher-Taylor leaky dielectric model. The model hypothesises development of interfacial charge on the application of an electric field and prescribes a balance between transient charge, jump in normal Ohmic currents due to finite conductivities of the medium and charge convection arising from interfacial velocity. While there have been numerous studies on the dynamics

of particles and drops more conducting than the surrounding liquid medium, weakly conducting particles and drops in strong electric fields, known to undergo symmetry-breaking bifurcations leading to steady rotation known as Quincke electrorotation, have received much less attention.

Recent experiments have reported a decrease in the effective viscosity of particle under Quincke rotation, thereby providing a means to tune the rheological properties of these suspensions. However, existing models based on an isolated particle, valid for dilute suspensions, have been shown to be inaccurate as the density of particles increases. Motivated to resolve these discrepancies, we develop a theoretical model to account for electrohydrodynamic interactions between a pair of spherical particles. We then turn our attention to many particles free to roll on an electrode due to Quincke rotation. Using numerical simulations, we show that electrohydrodynamic interactions between particles give rise to collective motion of these colloidal suspensions. We find emergence of a polar liquid state with a large vortical structure in circular confinement. Finally, we address the problem of electrohydrodynamics of deformable liquid drops, first studied by Taylor in 1966. We develop a transient small deformation theory for axisymmetric drops while including the nonlinear charge convection term neglected by previous researchers. We also use numerical simulations based on a novel three-dimensional boundary element method to capture large deformations. These simulations are the first to capture Quincke rotation due to inclusion of the nonlinear charge convection term and show excellent agreement with existing experimental data and theoretical predictions in the small deformation regime.

Chapter 1

Introduction

Classical physics deals with the mechanics of the fundamental states of matter namely solid, fluid, gas and plasma. Fluid mechanics is a branch of mechanics that deals with its properties and motion when subjected to forces or changes in temperature [9, 114, 87]. The governing equations for the motion of fluids is the Navier-Stokes equations that constitutes of mass, momentum and energy conservation equations,

$$\frac{D\rho}{Dt} + \rho\boldsymbol{\nabla}\cdot\boldsymbol{u} = 0, \tag{1.1a}$$

$$\rho\frac{D\boldsymbol{u}}{Dt} = -\boldsymbol{\nabla}p + \boldsymbol{\nabla}\cdot\boldsymbol{T}^H + \rho\boldsymbol{F}, \tag{1.1b}$$

$$\rho\frac{De}{Dt} = -p\boldsymbol{\nabla}\cdot\boldsymbol{u} + \boldsymbol{T}^H : \boldsymbol{\nabla}\boldsymbol{u} + \boldsymbol{\nabla}\cdot(\kappa\boldsymbol{\nabla}\Theta), \tag{1.1c}$$

where, ρ, $\boldsymbol{u}$, p, κ and e are the fluid density, velocity, pressure, thermal conductivity and internal energy respectively. $\boldsymbol{T}^H = \mu\left(\boldsymbol{\nabla}\boldsymbol{u} + \boldsymbol{\nabla}\boldsymbol{u}^T - \frac{2}{3}\boldsymbol{I}\boldsymbol{\nabla}\cdot\boldsymbol{u}\right)$ is the hydrodynamic stress, μ is the fluid viscosity, Θ is the temperature and $\boldsymbol{F}$ is the body force. The body force can be gravity, forces generated by electric or magnetic fields or internal stresses generated by swimming or flying organisms like bacteria, fish or birds. Equations of

state, $e = e(p, \Theta)$ and $p = \rho RT$ (ideal gas law) provide closure to the Navier-Stokes equations. Equations (1.1) are strictly valid for Newtonian fluids. The relationship between hydrodynamic stress and strain for a non-Newtonian fluid is more complex [13, 14, 15] and will not be considered in this thesis. Further simplifications can be made to the Navier-Stokes equations for incompressible fluids as the energy equation decouples from the rest of the Navier-Stokes equation. Using the following scales for velocity, length, time and pressure,

$$\hat{\boldsymbol{u}} = \frac{\boldsymbol{u}}{U}, \qquad \hat{\boldsymbol{x}} = \frac{\boldsymbol{x}}{L}, \qquad \hat{t} = \frac{t}{T}, \qquad \hat{p} = \frac{pL}{\mu U}, \tag{1.2}$$

we can non-dimensionalize the governing equations. To account for gravitational forces we substitute $\boldsymbol{F} = \boldsymbol{g}$. The conservation of mass, also called as continuity equation and momentum then read,

$$\boldsymbol{\nabla} \cdot \boldsymbol{u} = 0, \tag{1.3a}$$

$$\beta \frac{\partial \hat{\boldsymbol{u}}}{\partial \hat{t}} + Re\hat{\boldsymbol{u}} \cdot \hat{\boldsymbol{\nabla}}\hat{\boldsymbol{u}} = -\boldsymbol{\nabla}\hat{p} + \hat{\boldsymbol{\nabla}}\hat{\boldsymbol{u}} + \frac{Re}{Fr^2}\frac{\boldsymbol{g}}{g}. \tag{1.3b}$$

The relevant dimensionless parameters introduced in equation (1.3b) are,

$$\beta = \frac{L^2}{\nu T}, \qquad Re = \frac{UL}{\nu}, \qquad Fr = \frac{U}{\sqrt{gL}}. \tag{1.4}$$

The first term is the frequency parameter β denoting the ratio of inertial acceleration to viscous forces, second term is Reynolds number Re that denotes the ratio of inertial convective to viscous forces and the last term is the Froude's number Fr that compares the magnitude of inertial convective to body forces [127, 129].

1.1 Low Reynolds number regime: Stokes flow

When $Re \ll 1$ and $\beta \sim 1$, we can neglect the effects of convective acceleration and the Navier-Stokes equations reduce to unsteady Stokes equation,

$$\boldsymbol{\nabla} \cdot \boldsymbol{u} = 0, \qquad \frac{\partial \boldsymbol{u}}{\partial t} - \boldsymbol{\nabla} p + \mu \nabla^2 \boldsymbol{u} = 0. \tag{1.5}$$

Additionally, when $Re \ll 1$ and $\beta \ll 1$, we can neglect the unsteady term to obtain the steady Stokes equation.

$$\boldsymbol{\nabla} \cdot \boldsymbol{u} = 0, \qquad -\boldsymbol{\nabla} p + \mu \nabla^2 \boldsymbol{u} = 0. \tag{1.6}$$

Equations (1.5) and (1.6) are written in dimensional form. Physically, the unsteady Stokes equation describes flows characterized by sudden acceleration or deceleration. Few examples include the flow occurring in hydrodynamic braking, during the impact of a particle on a solid surface, and the initial stages of the flow due to a particle settling from rest in an ambient fluid [127, 129]. In this work, we only focus on phenomena occurring at the microscale level that are governed by the steady Stokes equations. The salient features of Stokes equations are described briefly below [57].

Linearity

Perhaps the most interesting feature of the steady Stokes equation is its linearity which allows one to obtain solutions using a variety of analytical methods based on separation of variables and singularity representations, for example, based on boundary element method for arbitrary geometries. A direct consequence of linearity is that *principle of superposition* of solutions may be applied by which adding different

solutions of the Stokes equations one also obtains a solution of the Stokes equations.

Reversibility

Another important consequence of linearity of Stokes is reversibility. Consider the motion of a spherical particle settling adjacent to a wall under the action of gravity. The question that one may ask is whether the sphere drifts away or towards the wall. This can be answered using principle of reversibility. Let us assume that the particle drifts towards the wall which means if the direction of gravity is reversed, the particle must drift away from the wall simply due to linearity of Stokes equation. However, reflecting this situation about the horizontal axis we get back the former situation with gravity pointing downwards, however, with the particle now moving away from the wall. This contradiction can only be resolved if the particle has no velocity perpendicular to the wall.

Instantaneity

Steady state Stokes equation has no time in it which implies that the motion is quasi-static. The motion of the fluid or particles in the fluid have no dependence on the history of the fluid flow. Mathematically, this means that the boundary motion is communicated to the entire fluid domain instantaneously. Some more important properties of Stokes flows are,

1. Pressure satisfies Laplace's equation, $\nabla^2 p = 0$,
2. Flow velocity satisfies the biharmonic equation $\nabla^4 \boldsymbol{u} = 0$,
3. Vorticity $\boldsymbol{\omega} = \boldsymbol{\nabla} \times \boldsymbol{u}$ satisfies Laplace's equation $\nabla^2 \boldsymbol{\omega} = 0$.

Additionally, axisymmetric Stokes flow can be conveniently solved with a Stokes streamfunction ϕ that satisfies the governing equation,

$$E^4\phi = 0, \qquad \text{where,} \qquad E^2 = \frac{\partial^2}{\partial r^2} + \frac{\sin\theta}{r^2}\frac{\partial}{\partial\theta}\left(\frac{1}{\sin\theta}\frac{\partial}{\partial\theta}\right) \tag{1.7}$$

Some other important properties of Stokes flow are minimum energy dissipation (also proves uniqueness) and Lorentz's reciprocal theorem. The reciprocal theorem is a very powerful tool that allows one to determine the results for one Stokes flow field from the solution of another Stokes flow in the same geometry [57]. As an example, let us consider a solid body that undergoes pure translation without rotation with velocity $\boldsymbol{U}^{(1)}$, the solution to which is denoted with superscript 1 and the same solid body that undergoes pure rotation without translation with velocity $\boldsymbol{U}^{(2)} = \boldsymbol{\Omega}^p \times \boldsymbol{x}$, the solution to which is denoted with superscript 2.

$$\begin{aligned}\int_V \boldsymbol{f}^{(1)} \cdot \boldsymbol{u}^{(2)}\,\mathrm{d}V + \int_S \boldsymbol{U}^{(2)} \cdot \boldsymbol{T}^{(1)} \cdot \boldsymbol{n}\,\mathrm{d}S \\ = \int_V \boldsymbol{f}^{(2)} \cdot \boldsymbol{u}^{(1)}\,\mathrm{d}V + \int_S \boldsymbol{U}^{(1)} \cdot \boldsymbol{T}^{(2)} \cdot \boldsymbol{n}\,\mathrm{d}S\end{aligned} \tag{1.8}$$

To simplify the problem, let us ignore the external forces, $\boldsymbol{f}^{(1)} = \boldsymbol{f}^{(2)} = 0$. We can easily see that the knowledge of the translational motion and traction in the first problem, $\boldsymbol{U}^{(1)}$, $\boldsymbol{T}^{(1)}$ and traction in the second problem, $\boldsymbol{T}^{(2)}$ can give us the rotational velocity of the particle in the second problem [57]. The reciprocal theorem is also the basis of boundary integral formulations that enables accurate computation of Stokes equation around arbitrary shaped objects. Problems in low Reynolds number regime governed by Stokes' equation can be solved using flow singularities, asymptotic solutions or numerical techniques. In the remainder of this chapter, we introduce

the concept of fundamental singularities to solve problems in Stokes flow and look at some common examples to illustrate the utility of these methods. This method is applicable to relatively simple shaped objects like sphere or ellipsoids. For arbitrary shaped objects, one needs to use a numerical technique like boundary element method, discussed briefly in section 1.3.

1.2 Fundamental singularities

A Stokeslet is the most fundamental singularity of Stokes flow. It is the free space Green's function that represents the flow field due to a point force [82, 129]. Physical examples include translating motion of a small particle sedimenting in a quiescent fluid or a charged particle translating under the action of an electric field in a fluid. The Stokes equation with a constant point force $\boldsymbol{b}$ located at $\boldsymbol{x}_0$ called as the evaluation point is,

$$-\boldsymbol{\nabla} p + \mu \nabla^2 \boldsymbol{u} + \boldsymbol{b}\delta_3(\boldsymbol{x} - \boldsymbol{x}_0) = 0, \tag{1.9}$$

where, δ_3 is the three dimensional delta function. The Stokeslet $\boldsymbol{G}$ and the flow field created by it are,

$$\boldsymbol{G}(\boldsymbol{x}; \boldsymbol{x}_0) = \frac{\boldsymbol{I}}{r} + \frac{\boldsymbol{r}\boldsymbol{r}}{r^3}, \qquad \boldsymbol{u} = \frac{1}{8\pi\mu}\boldsymbol{G} \cdot \boldsymbol{b}, \tag{1.10}$$

where, $\boldsymbol{r} = \boldsymbol{x} - \boldsymbol{x}_0$. Taking divergence of the velocity field and integrating the resulting expression over the domain of interest and using divergence theorem, we obtain an

important integral property of the Stokeslet,

$$\boldsymbol{\nabla} \cdot \boldsymbol{G} = 0, \qquad \int_S \boldsymbol{G}(\boldsymbol{x}; \boldsymbol{x}_0) \cdot \boldsymbol{n}(\boldsymbol{x}) \, \mathrm{d}S(\boldsymbol{x}) = 0. \tag{1.11}$$

Here, $\boldsymbol{x}$ is called as integration point and always lies on the boundary by definition. The identity, equation 1.11 holds true regardless of whether the evaluation point $\boldsymbol{x}_0$ lies on the boundary or not. The Stokeslet also satisfies the symmetry property,

$$\boldsymbol{G}(\boldsymbol{x}; \boldsymbol{x}_0) = \boldsymbol{G}(\boldsymbol{x}_0; \boldsymbol{x}). \tag{1.12}$$

The corresponding vorticity, pressure and stress fields associated with a Stokeslet are,

$$W_{ij} = 2\epsilon_{ijl}\frac{r_l}{r^3}, \qquad \mathcal{P}_j = 2\frac{r_j}{r^3}, \qquad T_{ijk} = -6\frac{r_i r_j r_k}{r^5}. \tag{1.13}$$

Any irrotational or potential flow field also satisfies the Stokes flow with the associated constant pressure field set to zero. The most fundamental solution to Laplace's equation, the governing equation for potential flow, is a point source. It is not hard to convince oneself that the derivatives of the point source are also solution to the Laplace's equation due to linearity. In the same way, derivatives of the point force also give rise to a family of fundamental solutions due to linearity of Stokes equation. Hence, the vorticity, pressure and stress fields constitute fundamental solutions to the Stokes flow called as rotlet, point-source and stresslet.

For example, a small particle exerting hydrodynamic torque or stress on the fluid is represented with a rotlet or a stresslet. In other words, any small particle that is under the influence of an external torque or stress can be represented as a

rotlet or stresslet respectively. For example, microorganisms such as Escherichia coli or Chlamydomonas reinhardtii that exert stresses on the surrounding fluid to propel themselves are represented by a stresslet [138]. Next, we look at some prototypical examples of particles motions in Stokes flow.

Disturbance flows created by spheres in uniform, rotational and straining flows

The disturbance flow created by a sphere held fixed in a uniform flow $\boldsymbol{U}^\infty$ is the same as a sphere translating with a velocity $\boldsymbol{U}^p = -\boldsymbol{U}^\infty$. Applying no slip and far field boundary conditions we get the desired flow and pressure fields,

$$u_i = -\frac{3a}{4}U_j^\infty\left(\frac{\delta_{ij}}{r} + \frac{r_i r_j}{r^3}\right) - \frac{a^3}{4}U_j^\infty\left(\frac{\delta_{ij}}{r^3} - \frac{3r_i r_j}{r^5}\right), \tag{1.14a}$$

$$p - p_\infty = -\frac{3\mu a}{2}\frac{U_j^\infty r_j}{r^3}. \tag{1.14b}$$

In equation (1.14a), the first tensor in the right hand side is easily recognized as the Stokeslet while the second term is a source quadrupole. The pressure field in expression (1.14b) is generated due to a dipole.

The flow and pressure field induced by a sphere rotating in an ambient flow $\boldsymbol{u}^\infty = \boldsymbol{\omega}^\infty \times \boldsymbol{x}$ or rotating at an angular velocity of $\boldsymbol{\omega}^p$ in a quiescent fluid are given by a rotlet,

$$u_i = -a^3\epsilon_{ijk}\omega_j^\infty\frac{r_k}{r^3} \qquad \text{or} \qquad a^3\epsilon_{ijk}\omega_j^p\frac{r_k}{r^3}, \tag{1.15a}$$

$$p = 0. \tag{1.15b}$$

The most interesting feature of a rotlet is that it doesn't create any pressure disturbance

in the fluid.

Finally, a stationary sphere placed in a straining flow induces flow and pressure field of the form,

$$u_i = -\frac{5a^3}{2}\frac{r_i(r_j E^{\infty}_{jk} r_k)}{r^5} - \frac{a^5}{2}E^{\infty}_{jk}\left[\frac{\delta_{ij}x_k + \delta_{ik}x_j}{r^5} - \frac{5r_i r_j r_k}{r^7}\right], \tag{1.16a}$$

$$p = -5\mu a^3 \frac{r_i E^{\infty}_{ij} r_j}{r^5}. \tag{1.16b}$$

Detailed derivations of these flow fields are omitted here for brevity and can be found in the references Guazzelli & Morris [57], Kim & Karrila [82], Pozrikidis [129].

Faxèn's laws

The generalized Faxèn's laws provide us with expressions of force, torque and stress on a spherical particle in an incident ambient flow. These expressions are very useful and used extensively in chapter 2 and 3. The hydrodynamic force and force moments of a spherical particle translating and rotating with velocities $\boldsymbol{U}^p, \boldsymbol{\Omega}^p$ in an ambient flow $\boldsymbol{u}^{\infty}, \boldsymbol{u}^{\infty} = \boldsymbol{\omega}^{\infty} \times \boldsymbol{x}$ and placed in a straining flow E^{∞}_{ij} are respectively given as,

$$F^h_i = 6\pi\mu a[(1 + \tfrac{1}{6}a^2\nabla^2)u^{\infty}_i(\boldsymbol{x} = 0) - U^p_i], \tag{1.17a}$$

$$T^h_i = 8\pi\mu a^3[\omega^{\infty}_i(\boldsymbol{x} = 0) - \Omega^p_i], \tag{1.17b}$$

$$S^h_{ij} = \tfrac{20}{3}\pi\mu a^3(1 + \tfrac{1}{10}a^2\nabla^2)E^{\infty}_{ij}(\boldsymbol{x} = 0). \tag{1.17c}$$

It is instructive to note that the isolated stresslet $\boldsymbol{S}^h$ has a linear form in the rate of strain $\boldsymbol{E}^{\infty}$ and as a consequence contributes to the bulk stress by the particles in the dilute limit. This was first discovered by Einstein who also derived the effective

viscosity of a suspension of particles as $u_{\text{eff}} = \mu[1 + 2.5\phi]$, ϕ being the particle volume fraction [47]. The Faxèn's laws discussed above are only valid for spherical particles. They can be extended to ellipsoidal particles or drops as well. However, for arbitrary shaped particles or drops in Stokes flow boundary element method is a commonly used technique discussed briefly in the next section.

1.3 Boundary element method

The boundary element method is a powerful numerical technique used to solve partial differential equations for which it is possible to compute a Green's function. This method is applicable to electromagnetic and potential problems governed by Laplace's equation, biomolecular electrostatics problems governed by linear Poisson-Boltzmann equation, fluid flow problems governed by Stokes equation, problems in acoustics governed by Helmholtz's equation and fracture mechanics problems governed by linear elasticity equation. In this work, we solve the coupled problem of electrohydrodynamics that requires boundary integral formulation of Laplace's and Stokes equations.

1.3.1 Laplace's equation

Let us consider two twice differentiable functions f and φ that satisfy Laplace's equation. Green's second identity then states,

$$f\nabla^2\varphi - \varphi\nabla^2 f = \boldsymbol{\nabla} \cdot (f\boldsymbol{\nabla}\varphi - \varphi\boldsymbol{\nabla} f). \tag{1.18}$$

We also note that the free space Green's function $\mathcal{G} = 1/(4\pi r)$ satisfies the singularly forced Laplace's equation,

$$\nabla^2 \mathcal{G}(\boldsymbol{x}; \boldsymbol{x}_0) + \delta_3(\boldsymbol{x} - \boldsymbol{x}_0) = 0. \tag{1.19}$$

Replacing f with the Green's function and using the equations 1.18 and 1.19,

$$\varphi(\boldsymbol{x})\delta_3(\boldsymbol{x} - \boldsymbol{x}_0) = \boldsymbol{\nabla} \cdot [\mathcal{G}(\boldsymbol{x}; \boldsymbol{x}_0)\boldsymbol{\nabla}\varphi(\boldsymbol{x}) - \varphi(\boldsymbol{x})\boldsymbol{\nabla}\mathcal{G}(\boldsymbol{x}; \boldsymbol{x}_0)]. \tag{1.20}$$

Equation 1.20 can then be integrated over a domain of volume V having boundary S which yields the desired boundary integral formulation after application of the divergence theorem,

$$\varphi(\boldsymbol{x}_0) = \int_S [\varphi(\boldsymbol{x})\{\boldsymbol{n}(\boldsymbol{x}) \cdot \boldsymbol{\nabla} G(\boldsymbol{x}; \boldsymbol{x}_0)\} - \mathcal{G}(\boldsymbol{x}; \boldsymbol{x}_0)\{\boldsymbol{n}(\boldsymbol{x}) \cdot \boldsymbol{\nabla}\varphi(\boldsymbol{x})\}] \, \mathrm{d}S(\boldsymbol{x}). \tag{1.21}$$

The first integral on the right hand side represents a distribution of point-sources called as a single layer potential (SLP) while the second integral represents a distribution of point-source dipoles called as double layer potential (DLP). The above equation is valid if the evaluation point is anywhere in the volume except the boundary. If the evaluation point $\boldsymbol{x}_0$ is on the boundary S, we can use integral identities to obtain,

$$\begin{aligned} \varphi(\boldsymbol{x}_0) = 2 \int_S \varphi(\boldsymbol{x})\{\boldsymbol{n}(\boldsymbol{x}) \cdot \boldsymbol{\nabla} G(\boldsymbol{x}; \boldsymbol{x}_0)\} \, \mathrm{d}S(\boldsymbol{x}) \\ - 2 \int_S^{PV} \mathcal{G}(\boldsymbol{x}; \boldsymbol{x}_0)\{\boldsymbol{n}(\boldsymbol{x}) \cdot \boldsymbol{\nabla}\varphi(\boldsymbol{x})\}] \, \mathrm{d}S(\boldsymbol{x}) \end{aligned} \tag{1.22}$$

where, PV denotes principal value [128].

1.3.2 Stokes equation

In order to derive a boundary integral formulation of Stokes equation, we need Lorentz's reciprocal theorem which is the counterpart of Green's second identity,

$$\frac{\partial}{\partial x_j}(\mu' u_i' \sigma_{ik} - \mu u_i \sigma_{ik}') = 0, \tag{1.23}$$

where, u_i, σ_{ij} and u_i', σ_{ij}' are two different solutions to the Stokes equation. Integrating over a control volume and applying divergence theorem we get,

$$\int_S [\mu' u_i'(\boldsymbol{x})\sigma_{ik}(\boldsymbol{x}) - \mu u_i(\boldsymbol{x})\sigma_{ik}'(\boldsymbol{x})] n_k(\boldsymbol{x})\, \mathrm{d}S(\boldsymbol{x}) = 0. \tag{1.24}$$

Replacing the solution with prime superscripts with the Stokeslet along with $\mu = \mu'$, we obtain,

$$\int_S [G_{ij}(\boldsymbol{x};\boldsymbol{x}_0)\sigma_{ik}(\boldsymbol{x}) - \mu u_i(\boldsymbol{x}) T_{ijk}'(\boldsymbol{x};\boldsymbol{x}_0)] n_k(\boldsymbol{x})\, \mathrm{d}S(\boldsymbol{x}) = 0. \tag{1.25}$$

A small spherical volume of infinitesimally small radius ϵ is then introduced around the evaluation point $\boldsymbol{x}_0$. The above integral is then valid over the boundary S and the small spherical volume S_ϵ. It can be shown that as the spherical volume becomes smaller $\epsilon \to 0$, the surface integral over the small spherical volume becomes equal to $8\pi\mu u_j(\boldsymbol{x}_0)$ [127, 129]. The desired boundary integral equation for Stokes flow is,

$$\begin{aligned} u_j(\boldsymbol{x}_0) = -\frac{1}{8\pi\mu}\int_S G_{ij}(\boldsymbol{x};\boldsymbol{x}_0) f_i(\boldsymbol{x})\, \mathrm{d}S(\boldsymbol{x}) \\ + \frac{1}{8\pi}\int_S u_i(\boldsymbol{x}) T_{ijk}(\boldsymbol{x};\boldsymbol{x}_0) n_k(\boldsymbol{x})\, \mathrm{d}S(\boldsymbol{x}). \end{aligned} \tag{1.26}$$

The physical interpretation of the integral formulation is the same as that of Laplace's equation. The first integral on the right hand side represents a distribution of Stokeslet on the boundaries and is also called as single layer potential while the second integral represents a distribution of stresslets and is called as double layer potential. When the evaluation point $\boldsymbol{x}_0$ is on the boundary, we get,

$$u_j(\boldsymbol{x}_0) = -\frac{1}{4\pi\mu}\int_S G_{ij}(\boldsymbol{x};\boldsymbol{x}_0) f_i(\boldsymbol{x})\,\mathrm{d}S(\boldsymbol{x}) + \frac{1}{4\pi}\int_S u_i(\boldsymbol{x}) T_{ijk}(\boldsymbol{x};\boldsymbol{x}_0) n_k(\boldsymbol{x})\,\mathrm{d}S(\boldsymbol{x}). \tag{1.27}$$

The boundary integral equation obtained for the two cases of Laplace's and Stokes equation can be solved numerically on a discretized boundary of interest. The main advantages of boundary element method over other numerical methods like finite elements, finite volume or finite differences is the reduction of the solution space by one dimension when compared to the physical space. For two-dimensional and axisymmetric domains, the integration is performed on contours while for three-dimensional domains the integration is performed over surfaces. Since the boundary integral formulation is an exact solution to the governing equations, the numerical solution tends to be highly accurate when compared to other numerical methods. However, the linear systems obtained by boundary element method are dense that can only be solved by using iterative solvers. As boundary integral equations are formed using fundamental solutions of the governing equations, they tend to be singular and these singularities need to be accurately treated numerically or analytically. Detailed derivations and applications of the boundary element method to potential and Stokes problems can be found in Pozrikidis [127, 128, 129].

1.4 Overview of current work

The main goal of this work is to develop theoretical models and numerical techniques to describe and understand the various electrohydrodynamic (EHD) phenomena observed in solid particles and liquid drops suspended in a fluid medium and subject to an electric field. All the problems considered in this work involve a complex interplay between electric and fluid forces at the microscale. The suspending fluid considered in this work are leaky dielectrics, examples of which include castor, silicone or vegetable oil. Ion dissociation is negligibly weak in these fluids as a result of which diffuse Debye layers are absent when compared to aqueous electrolytes. The associated phenomena in the latter case is called as electrokinetics (EK). While EHD and EK are very similar phenomena they have developed as independent subjects [145], however, there have been some attempts to unify the subjects [11, 147]. Electrohydrodynamics has many industrial application, particularly in designing novel microfluidic devices like microelectronics cooling pumps [7, 33, 133], jet printing [118], nanofibre fabrication [135, 175]. Electrohydrodynamic effects like electrophoresis (EP) and dielectrophoresis (DEP) have been used to manipulate particles [116, 117, 120] and cells [126] and create electronic displays by manipulating colloidal particles [30, 3, 73, 27].

Weakly conducting dielectric particles suspended in a dielectric liquid of higher conductivity can undergo a transition to spontaneous sustained rotation when placed in a sufficiently strong dc electric field. The second chapter deals with this phenomenon of Quincke rotation that has interesting implications for the rheology of these suspensions, whose effective viscosity can be controlled and reduced by application of an external field. While previous models based on the rotation of isolated particles have provided accurate estimates for this viscosity reduction in dilute suspensions, discrepancies

have been reported in more concentrated systems where particle-particle interactions are likely significant. Motivated by this observation, we extend the classic description of *Quincke rotation* based on the Taylor-Melcher leaky dielectric model to account for pair electrohydrodynamic interactions between two identical spheres using the method of reflections.

A coupled system of evolution equations for the dipole moments and angular velocities of the spheres is derived that accounts for electric dipole-dipole interactions and hydrodynamic rotlet interactions up to order $O(R^{-5})$, where R is the separation distance between the spheres. A linear stability analysis of this system shows that interactions modify the value of the critical electric field for the onset of Quincke rotation: both electric and hydrodynamic interactions can either stabilize or destabilize the system depending on the orientation of the spheres, but the leading effect of interactions on the onset of rotation is hydrodynamic. We also analyze the dynamics in the nonlinear regime by performing numerical simulations of the governing equations. In the case of a pair of spheres that are fixed in space, we find that particle rotations always synchronize in magnitude at long times, though the directions of rotation of the spheres need not be the same. The steady-state angular velocity magnitude depends on the configuration of the spheres and electric field strength and agrees very well with an asymptotic estimate derived for co-rotating spheres. In the case of freely-suspended spheres, dipolar interactions are observed to lead to a number of distinct behaviors depending on the initial relative configuration of the spheres and on any infinitesimal initial perturbation introduced in the system: in some cases the spheres slowly separate in space while steadily rotating, while in other cases they pair up and either co- or counter-rotate depending on their orientation relative to the field.

The third chapter builds on the ideas presented previously and discusses the effect of wall on Quincke electrorotation of spherical particles. When we bring a spherical particle under Quincke electrorotation closer to a wall, its angular velocity gets coupled to its translational velocity producing propulsion. We show that a single isolated particle or roller translates with a constant speed without any change in its direction. The electrohydrodynamic interactions between many such particles or rollers, however, very interestingly gives rise to collective motion first discovered in the experiments of Bricard *et al.* [23]. This relatively simple electrohydrodynamic system gives an insight into the collective motion of more complicated systems in confinement involving organisms ranging from the microscale like a colony of bacteria to much larger organisms like a school of fish or flock of birds. The pioneering work of Vicsek *et al.* [166] attempted to develop a simple pair interaction based model to understand the collective motion exhibited by these systems. Since then there have been numerous attempts to extend these models, however, many times based on ad hoc interaction rules. The most attractive feature of the Quincke rollers system is that the interactions between these rollers based on Stokes and Maxwell's equations are well defined and the parameters are easily controllable and measurable. Using a combination of theory, experiments and simulations, we explain this collective behavior.

The fourth chapter concerns with the deformation of a viscous liquid droplet suspended in another liquid and subject to an applied electric field. It is a classic multiphase flow problem best described by the Melcher-Taylor leaky dielectric model. The main assumption of the model is that any net charge in the system is concentrated on the interface between the two liquids as a result of the jump in Ohmic currents from the bulk. Upon application of the field, the drop can either attain a steady

prolate or oblate shape with toroidal circulating flows both inside and outside arising from tangential stresses on the interface due to action of the field on the surface charge distribution. Since the pioneering work of Taylor [159], there have been numerous computational and theoretical studies to predict the deformations measured in experiments. Most existing theoretical models, however, have either neglected transient charge relaxation or nonlinear charge convection by the interfacial flow. In this work, we develop a novel small-deformation theory accurate to second order in electric capillary number $O(Ca_E^2)$ for the complete Melcher-Taylor model that includes transient charge relaxation, charge convection by the flow, as well as transient shape deformation. The main result of the paper is the derivation of coupled evolution equations for the induced electric multipoles and for the shape functions describing the deformations on the basis of spherical harmonics. Our results, which are consistent with previous models in the appropriate limits, show excellent agreement with fully nonlinear numerical simulations based on an axisymmetric boundary-element formulation and with existing experimental data in the small-deformation regime.

The fifth chapter describes the formulation of a three-dimensional boundary element method for the complete leaky dielectric model to systematically study the deformation and dynamics of liquid drops in electric fields. Most of the numerical simulations in previous studies that are based on Melcher-Taylor leaky delectric model have either neglected interfacial charge convection or restricted themselves to axisymmetric drops. The inclusion of charge convection in our simulation permits us to investigate drops in the Quincke regime, in which experiments have demonstrated symmetry breaking bifurcations leading steady electrorotation. Our simulation results show excellent agreement with existing experimental data and small deformation

theories.

Finally, we conclude in chapter 6 and discuss potential extensions of the work presented in this thesis.

Chapter 2

Electrohydrodynamic interaction of spherical particles under Quincke rotation

2.1 Introduction

Electrorheological (ER) fluids, or collections of fine dielectric particles suspended in a dielectric liquid [51, 60, 119, 150], are commonly used in a wide range of technological applications such as hydraulic valves [107] and clutches, brakes [152], shock absorbers [155], as well as in various microfluidic devices [178, 106, 169]. When placed in an electric field, the particles in an ER fluid polarize and interact, causing them in most cases to form chains and larger aggregation patterns in the direction of the field [51, 61, 86, 116, 117], thereby strongly enhancing the effective viscosity of the suspension. The formation of these internal structures is reversible and can be suppressed upon switching off of the field, offering an easy way of controlling the

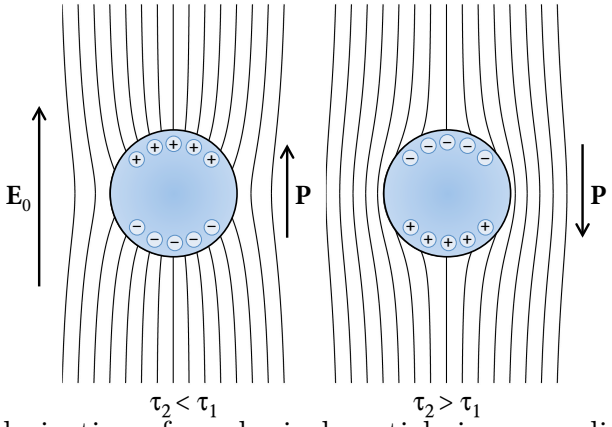

Figure 2.1: Polarization of a spherical particle in an applied electric field $\mathbf{E}_0$. (Left) If the charge relaxation time $\tau_2 = \varepsilon_2/\sigma_2$ of the particle is less than that, $\tau_1 = \varepsilon_1/\sigma_1$, of the suspending fluid, the induced dipole $\mathbf{P}$ is parallel to the applied field; (right) if it is greater, the induced dipole is antiparallel. After Ref. [76].

rheological properties of the fluid in real time. This so-called positive ER effect, by which chaining in the field direction results in a viscosity increase, is generally observed when the conductivity σ_2 of the suspended particles is larger than that of the carrier liquid, denoted by σ_1. The situation is quite different when $\sigma_1 > \sigma_2$, where chains and sheets of particles have been reported to form in directions perpendicular to the electric field and can result in an effective decrease in the apparent viscosity of the suspension [18].

Under certain conditions, application of a steady uniform electric field can also drive the spontaneous rotation of spherical particles. This peculiar phenomenon was first discovered by Weiler [171] and Quincke [130] in the late nineteenth century, and has later become known as Quincke rotation. Detailed models for this effect were subsequently developed by Tsebers [164] and Jones [76], who used Melcher and Taylor's leaky dielectric model [103, 145] and identified the following mechanism for Quincke rotation. As depicted in Fig. 2.1, the sign of the dipole induced in a spherical particle placed in a uniform electric field depends on the properties of the particle

and liquid phases. If the ratio of the dielectric permittivity to the conductivity of the material is larger in the suspending liquid than inside the particle, the induced dipole is parallel to the direction of the applied field; if it is less, the induced dipole is anti-parallel. This ratio $\tau = \varepsilon/\sigma$ also corresponds to the characteristic relaxation time for the surface charge distribution on the surface of the particle upon application of the field. If the orientation of the sphere is weakly perturbed, a mechanical torque arises as a result of the Maxwell stress in the fluid, which is restoring in the first case but destabilizing in the second case. If the electric field is strong enough to overcome the effect of the viscous torque on the particle, this can result in the steady spontaneous rotation of the particle with a constant angular velocity around an arbitrary axis perpendicular to the direction of the applied field. To summarize, Quincke rotation occurs if

$$\frac{\varepsilon_2}{\sigma_2} > \frac{\varepsilon_1}{\sigma_1}, \tag{2.1}$$

which is to say that the characteristic charge relaxation time is larger inside the particle than outside, and if the electric field strength exceeds a critical value E_c whose expression will be derived in Sec. 2.2.1 in terms of material properties. A full stability analysis of the dynamical system shows that the onset of Quincke rotation is associated with a supercritical pitchfork bifurcation. If particle inertia is significant, the dynamics of the system are formally identical to those of the classic Lorenz oscillator [101], and further increasing the field strength therefore eventually leads to a second bifurcation to unsteady chaotic dynamics [94], as has also been observed in experiments [124]. Spontaneous electrorotation followed by complex deformation dynamics has also been reported in experiments on weakly conducting droplets suspended in a less conducting fluid when placed in a strong electric field [84, 59, 141].

Quincke electrorotation in large-scale suspensions has interesting consequences for the effective rheology of the suspensions [98, 95, 112, 96, 125, 69, 70]. When an external shear flow is applied (for instance in a Couette device or in pressure-driven Poiseuille flow) together with a sufficiently strong external electric field in the flow gradient direction, Quincke rotation arises in the same direction as the external flow vorticity and thereby effectively decreases the apparent viscosity of the suspension. This effect, which is easy to interpret theoretically [21, 75, 69], has been observed in a number of experiments in both Couette and pressure-driven flow setups [98, 95, 112, 96, 125]. An increase in the effective electric conductivity of the suspension has also been observed [26, 113]. While experiments show fairly good agreement with simple dilute theoretical predictions for the change of viscosity in sufficiently strong flows of dilute suspensions [95], departures from these predictions have been reported at low shear rates and high concentrations, presumably as a result of particle-particle electrohydrodynamic interactions, which may cause structuring of the suspension in the form of chains or other types of aggregates as in previously studied ER fluids.

Particle-particle interactions in Quincke rotation have only received limited attention up to now, in part owing to the strongly nonlinear nature of the governing set of equations, which will be described below. In early work, Wan *et al.* [168] considered the electrostatic interaction of a pair of dielectric spheres, and derived the induced dipoles in both spheres using bispherical coordinates. They then used this result to evaluate the mean force on a particle when one of the two spheres was rotated at a constant angular velocity around the other one. Their study, however, did not account for the change in polarization of the particles as a result of Quincke rotation nor for

the effect of hydrodynamic interactions. More recently, a significantly more detailed analysis was proposed by Dolinsky & Elperin [40], who used a somewhat similar treatment as in the present work. They applied the method of reflections to analyze Quincke rotation of a pair of spheres in an external field. They derived expressions for the induced electric dipoles in both spheres that accounted for electric interactions as well as particle rotations, and used these expressions to draw conclusions on the effect of interactions on the angular velocity of the spheres and electric forces due to dipole-dipole interactions. Their study, however, entirely neglected hydrodynamic interactions due to the rotation and motion of the spheres; these interactions, as we show below, are as important as electric interactions as they modify the induced dipoles and resulting angular velocities at the same asymptotic order.

In the present paper, we describe a detailed asymptotic analysis of the effects of both electric and hydrodynamic interactions on Quincke rotation of a pair of identical spheres suspended in an unbounded domain when a uniform external electric field is applied. The details of the model, which is based on the leaky dielectric model of Melcher and Taylor [103] and extends previous classic studies of Quincke rotation of isolated particles [164, 76], are presented in Sec. 2.2, where a set of coupled nonlinear ordinary differential equations for the dipole moments and angular velocities of the two spheres are derived using the method of reflections [137] and are valid to order $O(R^{-5})$, where R denotes the distance between the two spheres. This set of equations is then used to study the stability of the system in Sec. 2.3, where a linear stability analysis shows that interactions can either increase or decrease the value of the critical electric field for onset of rotation depending on the configuration of the spheres. Finally, we also carry out numerical simulations of both fixed and freely suspended

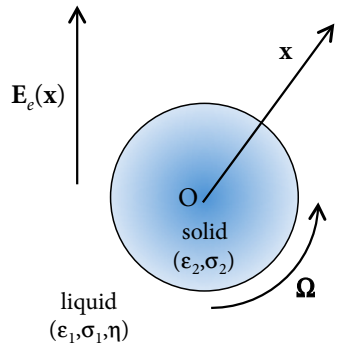

Figure 2.2: Isolated sphere undergoing Quincke rotation in a nonuniform external field $\mathbf{E}_e(\mathbf{x})$.

spheres in Sec. 2.4, and show that interactions lead to synchronization of the particle rotations and either pairing or separation of the two particles depending on their initial configuration and on the infinitesimal perturbation introduced in the system at $t = 0$. We conclude in Sec. 4.6.

2.2 Theoretical model

2.2.1 Single sphere in a nonuniform field

Governing equations and moment equations

We first analyze in detail the case of a single isolated sphere of radius a placed in an infinite liquid and subject to a nonuniform external electric field $\mathbf{E}_e(\mathbf{x}) = -\nabla\phi_e(\mathbf{x})$ as depicted in Fig. 2.2. Denote by $(\varepsilon_1, \sigma_1)$ the permittivity and conductivity of the suspending liquid, and by $(\varepsilon_2, \sigma_2)$ those of the particle. We adopt a coordinate system with the origin at the center of the sphere, and we assume that the external potential $\phi_e(\mathbf{x})$ in the absence of the sphere can be expanded in a Taylor series about the origin as

$$\phi_e(\mathbf{x}) = \phi_e(\mathbf{0}) + \mathbf{x}\cdot\nabla\phi_e(\mathbf{0}) + \frac{1}{2}\mathbf{x}\mathbf{x} : \nabla\nabla\phi_e(\mathbf{0}) + ..., \tag{2.2}$$

where we neglect higher-order terms in this discussion for reasons that will become clear in Sec. 2.2.2. The presence of the sphere perturbs the external potential as:

$$\phi(\mathbf{x}) = \begin{cases} \phi^+(\mathbf{x}) = \phi_e(\mathbf{x}) + \phi_d^+(\mathbf{x}) & \text{if } |\mathbf{x}| > a, \\ \phi^-(\mathbf{x}) = \phi_e(\mathbf{x}) + \phi_d^-(\mathbf{x}) & \text{if } |\mathbf{x}| < a, \end{cases} \tag{2.3}$$

where we wish to determine the disturbance potentials $\phi_d^+(\mathbf{x})$ and $\phi_d^-(\mathbf{x})$ outside and inside the sphere, respectively.

Following the classic Taylor-Melcher leaky dielectric model [103, 145], which was also used in previous studies of Quincke rotation [164, 76], we assume that any induced charge in the system is concentrated at the interface between the solid and liquid in the form of a surface charge distribution $q(\mathbf{x})$, which is related to the normal jump in the electric displacement field across the interface via Gauss's law [72]:

$$q(\mathbf{x}) = \mathbf{n} \cdot [\![\varepsilon \mathbf{E}(\mathbf{x})]\!] = -\mathbf{n} \cdot [\varepsilon_1 \nabla \phi^+(\mathbf{x}) - \varepsilon_2 \nabla \phi^-(\mathbf{x})], \tag{2.4}$$

where $\mathbf{n} = \mathbf{x}/x$ is a unit outward normal on the particle surface. Under this assumption, both disturbance potentials satisfy Laplace's equation since there is no net charge in the solid and liquid away from the interface:

$$\nabla^2 \phi_d^+(\mathbf{x}) = \nabla^2 \phi_d^-(\mathbf{x}) = 0. \tag{2.5}$$

This will allow us to seek solutions as expansions in spherical harmonics below. Boundary conditions on the potentials are as follows. First, the disturbance potential

outside the sphere must decay far away from the surface:

$$\phi_d^+(\mathbf{x}) \to 0 \quad \text{as} \ \ |\mathbf{x}| \to \infty. \tag{2.6}$$

Second, the potential must be continuous across the interface:

$$\phi_d^+(\mathbf{x}) = \phi_d^-(\mathbf{x}) \quad \text{if} \ \ |\mathbf{x}| = a. \tag{2.7}$$

The third boundary condition expresses charge conservation on the interface as a result of Ohmic currents from the bulk and charge convection by the moving surface:

$$\frac{\partial q}{\partial t} + \mathbf{n} \cdot [\![\mathbf{J}]\!] + \nabla_s \cdot (q\mathbf{V}) = 0 \quad \text{at} \ \ |\mathbf{x}| = a. \tag{2.8}$$

In Eq. (2.8), $\mathbf{n} \cdot [\![\mathbf{J}]\!]$ denotes the normal jump in Ohmic current across the interface:

$$\mathbf{n} \cdot [\![\mathbf{J}(\mathbf{x})]\!] = \mathbf{n} \cdot [\![\sigma\mathbf{E}(\mathbf{x})]\!] = -\mathbf{n} \cdot [\sigma_1 \nabla\phi^+(\mathbf{x}) - \sigma_2 \nabla\phi^-(\mathbf{x})]. \tag{2.9}$$

Also, $\nabla_s = (\mathbf{I} - \mathbf{nn}) \cdot \nabla$ is the surface divergence operator, and $\mathbf{V}$ is the velocity of a point on the sphere surface, which is assumed to be rotating at a yet unknown angular velocity $\mathbf{\Omega}$: $\mathbf{V} = \mathbf{\Omega} \times a\mathbf{n}$.

Solutions of Eq. (5.1) for the disturbance potentials outside and inside the sphere can be written as expansions in decaying and growing spherical harmonics,

respectively:

$$\phi_d^+(\mathbf{x}) = \frac{\mathbf{x}\cdot\mathbf{P}}{x^3} + \frac{1}{2}\frac{\mathbf{xx}:\mathbf{Q}}{x^5} + ..., \tag{2.10}$$

$$\phi_d^-(\mathbf{x}) = \frac{\mathbf{x}\cdot\mathbf{P}}{a^3} + \frac{1}{2}\frac{\mathbf{xx}:\mathbf{Q}}{a^5} + ..., \tag{2.11}$$

which automatically satisfy the two boundary conditions of Eqs. (2.6)–(2.7). In Eqs. (2.10)–(2.11), vector $\mathbf{P}$ denotes the dipole moment on the sphere, and second-order tensor $\mathbf{Q}$ denotes the quadrupole moment. We do not include any monopole in the expansions as the sphere is assumed to carry no net charge. Higher-order multipoles could also be included, though we will not consider them here as these will be negligible in the study of pair interactions in Sec. 2.2.2. Substituting these expansions into the charge conservation equation (2.8) allows one to derive evolution equations for the moments $\mathbf{P}$ and $\mathbf{Q}$ as

$$\frac{d\mathbf{P}}{dt} = \mathbf{\Omega}\times[\mathbf{P} + a^3\varepsilon_{21}\nabla\phi_e(\mathbf{0})] - \frac{1}{\tau_{\mathrm{MW}}}\left[\mathbf{P} + a^3\sigma_{21}\nabla\phi_e(\mathbf{0})\right], \tag{2.12}$$

$$\frac{d\mathbf{Q}}{dt} = \mathbf{\Omega}\times[\mathbf{Q} + a^5\varepsilon'_{21}\nabla\nabla\phi_e(\mathbf{0})] - \frac{1}{\tau'_{\mathrm{MW}}}[\mathbf{Q} + a^5\sigma'_{21}\nabla\nabla\phi_e(\mathbf{0})], \tag{2.13}$$

where τ_{MW} and τ'_{MW} are the first and second Maxwell-Wagner relaxation times:

$$\tau_{\mathrm{MW}} = \frac{\varepsilon_2 + 2\varepsilon_1}{\sigma_2 + 2\sigma_1}, \quad \tau'_{\mathrm{MW}} = \frac{2\varepsilon_2 + 3\varepsilon_1}{2\sigma_2 + 3\sigma_1}, \tag{2.14}$$

and where we have introduced the following dimensionless parameters:

$$\varepsilon_{21} = \frac{\varepsilon_2 - \varepsilon_1}{\varepsilon_2 + 2\varepsilon_1}, \quad \varepsilon'_{21} = \frac{\varepsilon_2 - \varepsilon_1}{2\varepsilon_2 + 3\varepsilon_1}, \quad \sigma_{21} = \frac{\sigma_2 - \sigma_1}{\sigma_2 + 2\sigma_1}, \quad \sigma'_{21} = \frac{\sigma_2 - \sigma_1}{2\sigma_2 + 3\sigma_1}. \tag{2.15}$$

In Eq. (2.13), the notations $\boldsymbol{\Omega} \times \mathbf{Q}$ and $\boldsymbol{\Omega} \times \nabla\nabla\phi_e(\mathbf{0})$ are used to denote the following two tensors in index notation:

$$[\boldsymbol{\Omega} \times \mathbf{Q}]_{ij} = \epsilon_{ikl}\Omega_k Q_{lj}, \quad [\boldsymbol{\Omega} \times \nabla\nabla\phi_e(\mathbf{0})]_{ij} = \epsilon_{ikl}\Omega_k \frac{\partial^2 \phi_e}{\partial x_l \partial x_j}(\mathbf{0}). \tag{2.16}$$

Equation (2.12) for the dipole moment $\mathbf{P}$ differs slightly from the dipole evolution equation appearing in previous studies of Quincke rotation [69, 70], through the presence of the term involving $\boldsymbol{\Omega} \times \nabla\phi_e(\mathbf{0})$. This discrepancy is easily resolved by realizing that the dipole $\mathbf{P}$ appearing in Eq. (2.12) is the total dipole moment on the particle, whereas previous studies have typically focused on the retarding dipole moment defined as $\mathbf{P}_r = \mathbf{P} - \mathbf{P}_\infty$, where $\mathbf{P}_\infty = -a^3\varepsilon_{21}\nabla\phi_e(\mathbf{0})$ is the instantaneous polarization. From Eq. (2.12), it is straightforward to recover the commonly used equation for $\mathbf{P}_r$:

$$\frac{d\mathbf{P}_r}{dt} = \boldsymbol{\Omega} \times \mathbf{P}_r - \frac{1}{\tau_{\mathrm{MW}}}[\mathbf{P}_r - a^3(\varepsilon_{21} - \sigma_{21})\nabla\phi_e(\mathbf{0})]. \tag{2.17}$$

Similarly, an equation can be written for the retarding quadrupole moment $\mathbf{Q}_r = \mathbf{Q} - \mathbf{Q}_\infty$ where $\mathbf{Q}_\infty = -a^5\varepsilon'_{21}\nabla\nabla\phi_e(\mathbf{0})$ as

$$\frac{d\mathbf{Q}_r}{dt} = \boldsymbol{\Omega} \times \mathbf{Q}_r - \frac{1}{\tau'_{\mathrm{MW}}}[\mathbf{Q}_r - a^5(\varepsilon'_{21} - \sigma'_{21})\nabla\nabla\phi_e(\mathbf{0})]. \tag{2.18}$$

For the purpose of studying Quincke rotation, it is equivalent to use $(\mathbf{P}, \mathbf{Q})$ or $(\mathbf{P}_r, \mathbf{Q}_r)$, as we will see below that the instantaneous dipole and quadrupole moments $\mathbf{P}_\infty$ and $\mathbf{Q}_\infty$ do not contribute to the electric torque on the particle. In this work, we make the choice of working with the total moments $\mathbf{P}$ and $\mathbf{Q}$, which satisfy Eqs. (2.12)–(2.13).

The physical interpretation of Eqs. (2.12)–(2.13) is straightforward: the retarding parts of the dipole and quadrupole moments are subject to the rotation of the particle with angular velocity $\mathbf{\Omega}$, while the total dipole and quadrupole simultaneously relax toward their steady-state values in the absence of rotation. The time scales for these relaxation processes are given by the Maxwell-Wagner relaxation times of Eq. (2.14). It is also easy to see how additional equations for higher multipole moments could also obtained, though we do not include them here.

Balance of angular momentum

In the above discussion, we have assumed that the sphere is rotating at a given angular velocity $\mathbf{\Omega}$, which is still unknown. To determine $\mathbf{\Omega}$, we write down the angular momentum balance for the sphere, which is subject to both viscous and electric torques:

$$I\frac{d\mathbf{\Omega}}{dt} = -8\pi\eta a^3\mathbf{\Omega} + \mathbf{T}^e. \tag{2.19}$$

Here, $I = 2ma^3/5$ is the moment of inertia of a sphere of mass m, η is the viscosity of the suspending liquid, and $\mathbf{T}^e$ is the electric torque on the particle. Both the dipole and quadrupole moments can contribute to the electric torque, which was previously calculated by Jones and Washizu [77] as

$$\mathbf{T}^e = -4\pi\varepsilon_1[\mathbf{P}\times\nabla\phi_e(\mathbf{0}) + (\mathbf{Q}\cdot\nabla)\times\nabla\phi_e(\mathbf{0})], \tag{2.20}$$

or, in index notation:

$$T_i^e = -4\pi\varepsilon_1\left[\epsilon_{ijk}P_j\frac{\partial\phi_e}{\partial x_k}(\mathbf{0}) + \epsilon_{ijk}Q_{jl}\frac{\partial^2\phi_e}{\partial x_l\partial x_k}(\mathbf{0})\right]. \tag{2.21}$$

From this expression, it is easy to see that the instantaneous dipole and quadrupole moments, which are collinear with $\nabla\phi_e(\mathbf{0})$ and $\nabla\nabla\phi_e(\mathbf{0})$, respectively, do not result in any torque on the particle.

In this paper, we focus on the inertialess limit where the left-hand side in Eq. (2.19) is negligible. In this case, the angular momentum balance simplifies to the following relation between angular velocity and multipole moments:

$$2\eta a^3\mathbf{\Omega} + \varepsilon_1[\mathbf{P}\times\nabla\phi_e(\mathbf{0}) + (\mathbf{Q}\cdot\nabla)\times\nabla\phi_e(\mathbf{0})] = 0. \tag{2.22}$$

Equations (2.12)–(2.13), together with Eq. (2.22), constitute a coupled system of equations for $\mathbf{P}$, $\mathbf{Q}$, and $\mathbf{\Omega}$, which can be analyzed or integrated numerically given an initial condition.

Steady-state solutions

We first seek steady-state solutions to this system of equations, with the aim of determining conditions for spontaneous steady rotation to arise. At steady state, Eqs. (2.12)–(2.13) for the dipole and quadrupole moments reduce to:

$$\mathbf{\Omega}\times\mathbf{P} - \frac{1}{\tau_{\mathrm{MW}}}\mathbf{P} = \frac{a^3\sigma_{21}}{\tau_{\mathrm{MW}}}\nabla\phi_e(\mathbf{0}) - a^3\varepsilon_{21}\mathbf{\Omega}\times\nabla\phi_e(\mathbf{0}), \tag{2.23}$$

$$\mathbf{\Omega}\times\mathbf{Q} - \frac{1}{\tau'_{\mathrm{MW}}}\mathbf{Q} = \frac{a^3\sigma'_{21}}{\tau'_{\mathrm{MW}}}\nabla\nabla\phi_e(\mathbf{0}) - a^3\varepsilon'_{21}\mathbf{\Omega}\times\nabla\nabla\phi_e(\mathbf{0}). \tag{2.24}$$

These two equations admit analytical solutions for $\mathbf{P}$ and $\mathbf{Q}$:

$$\mathbf{P} = A_1[\mathbf{\Omega}\times\nabla\phi_e(\mathbf{0}) + \tau_{\mathrm{MW}}(\mathbf{\Omega}\cdot\nabla\phi_e(\mathbf{0}))\mathbf{\Omega}] - A_2\nabla\phi_e(\mathbf{0}), \tag{2.25}$$

$$\mathbf{Q} = A_3[\mathbf{\Omega}\times\nabla\nabla\phi_e(\mathbf{0}) + \tau'_{\mathrm{MW}}(\mathbf{\Omega}\cdot\nabla\nabla\phi_e(\mathbf{0}))\mathbf{\Omega}] - A_4\nabla\nabla\phi_e(\mathbf{0}), \tag{2.26}$$

where the coefficients A_1 through A_4 are given by

$$A_1 = \frac{a^3\tau_{\mathrm{MW}}(\varepsilon_{21} - \sigma_{21})}{1 + \Omega^2\tau_{\mathrm{MW}}^2}, \quad A_2 = a^3\left[\varepsilon_{21} + \frac{\sigma_{21} - \varepsilon_{21}}{1 + \Omega^2\tau_{\mathrm{MW}}^2}\right], \tag{2.27}$$

$$A_3 = \frac{a^3\tau'_{\mathrm{MW}}(\varepsilon'_{21} - \sigma'_{21})}{1 + \Omega^2\tau_{\mathrm{MW}}'^2}, \quad A_4 = a^3\left[\varepsilon'_{21} + \frac{\sigma'_{21} - \varepsilon'_{21}}{1 + \Omega^2\tau_{\mathrm{MW}}'^2}\right]. \tag{2.28}$$

Finally, substituting Eqs. (2.25)–(2.26) into the torque balance Eq. (2.22) yields a nonlinear equation for the angular velocity $\mathbf{\Omega}$.

Obtaining an exact analytical expression for $\mathbf{\Omega}$ or its norm when the electric field is nonuniform (i.e., when $\nabla\nabla\phi_e(\mathbf{0}) \neq \mathbf{0}$) is not straightforward, though Eq. (2.22) could still be used in numerical simulations. However, the case of a uniform field can be further analyzed. If $\nabla\nabla\phi_e(\mathbf{0}) = \mathbf{0}$ and $\mathbf{Q} = \mathbf{0}$, the equation for $\mathbf{\Omega}$ simplifies to

$$2\eta a^3\mathbf{\Omega} + \varepsilon_1 A_1[\mathbf{\Omega} \times \nabla\phi_e + \tau_{\mathrm{MW}}(\mathbf{\Omega} \cdot \nabla\phi_e)\mathbf{\Omega}] \times \nabla\phi_e = \mathbf{0}. \tag{2.29}$$

Taking the dot product of Eq. (2.29) with the local potential gradient $\nabla\phi_e$ immediately yields

$$\mathbf{\Omega} \cdot \nabla\phi_e = 0, \tag{2.30}$$

i.e., any particle rotation will have an angular velocity $\mathbf{\Omega}$ normal to the direction of the external field. The exact direction of rotation is however indeterminate. The magnitude of the angular velocity can be obtained by taking the dot product of Eq. (2.29) with $\mathbf{\Omega}$:

$$2\eta a^3\Omega^2 - \varepsilon_1 A_1 \Omega^2 E_e^2 = 0, \tag{2.31}$$

where we have introduced the magnitude of the external electric field $\mathbf{E}_e = -\nabla\phi_e$. Using Eq. (2.27) for A_1, which is itself a function of Ω^2, we obtain a biquadratic

equation for $\Omega = |\mathbf{\Omega}|$:

$$\Omega^2 \left[\Omega^2 \tau_{\mathrm{MW}}^2 + 1 - \frac{\varepsilon_1 \tau_{\mathrm{MW}} (\varepsilon_{21} - \sigma_{21})}{2\eta} E_e^2 \right] = 0. \tag{2.32}$$

The solution $\Omega = 0$ always exists and corresponds to the absence of rotation. However, another solution is also given by

$$\Omega = \pm \frac{1}{\tau_{\mathrm{MW}}} \sqrt{\left(\frac{E_e}{E_c} \right)^2 - 1}, \quad \text{with} \;\; E_c = \sqrt{\frac{2\eta}{\varepsilon_1 \tau_{\mathrm{MW}} (\varepsilon_{21} - \sigma_{21})}}. \tag{2.33}$$

This solution, which is the same as that obtained in previous studies of Quincke rotation [76], only arises when the value of the external field E_e exceeds the critical value E_c. The solutions are plotted in Fig. 2.3, where we see that the steady solution with $\mathbf{\Omega} = \mathbf{0}$ bifurcates at $E_e = E_c$. From the definition of E_c, it is clear that Quincke rotation can only occur if $\varepsilon_{21} > \sigma_{21}$, which is easily shown to be equivalent to

$$\frac{\varepsilon_2}{\sigma_2} > \frac{\varepsilon_1}{\sigma_1}, \tag{2.34}$$

in agreement with the physical interpretation provided in Sec. 2.1.

A linear stability analysis of the dynamical system shows that the onset of Quincke rotation corresponds to a supercritical pitchfork bifurcation, and that the steady solution loses its stability when $E_e > E_c$. In experiments, spontaneous rotation is expected to take place in this case, around an arbitrary direction perpendicular to the field direction and with an angular velocity magnitude given by Eq. (2.33). In the absence of particle inertia, the two branches defined by Eq. (2.33) are stable for any field strength satisfying $E_e > E_c$. If inertia is retained in the angular momentum

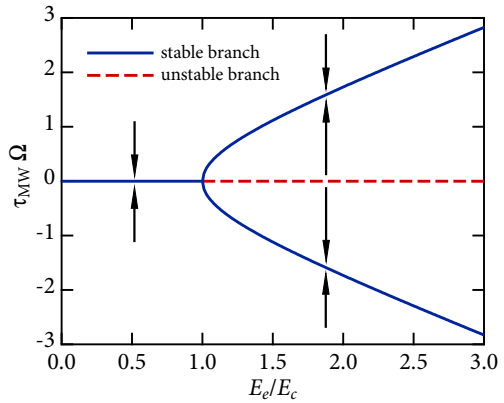

Figure 2.3: Stability diagram for the angular velocity magnitude of a single sphere. A supercritical pitchfork bifurcation occurs at $E_e = E_c$; above this value, the solution $\Omega = 0$ becomes unstable and spontaneous rotation occurs with an angular velocity given by Eq. (2.33).

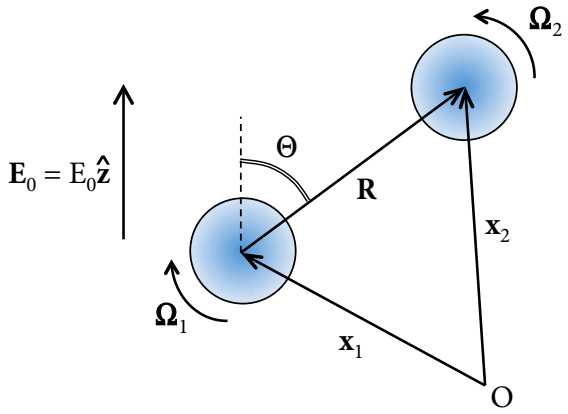

Figure 2.4: Interaction of two identical spheres undergoing Quincke rotation in a uniform field $\mathbf{E}_0$.

balance of Eq. (2.19), previous studies have shown that the governing equations for $\mathbf{P}$ and $\mathbf{\Omega}$ can be reduced to the Lorenz oscillator equations [101], and that a transition to chaos therefore occurs in very strong fields [94, 124].

2.2.2 Two spheres in a uniform field

Electric problem

We now consider the case of two identical spheres separated by a vector $\mathbf{R} = \mathbf{x}_2 - \mathbf{x}_1$ and placed in a uniform electric field $\mathbf{E}_0$ as depicted in Fig. 2.4. We also define the notations $R = |\mathbf{R}|$ and $\widehat{\mathbf{R}} = \mathbf{R}/R$. We wish to analyze the leading-order effect of electric and hydrodynamic interactions between the spheres based on the single-particle results derived in Sec. 2.2.1 and using the method of reflections. Note that because the spheres perturb the electric field around them, they really experience a non-uniform field as a result of interactions. First, each sphere polarizes under the field, and develops a dipole moment $\mathbf{P}_\alpha$ (with $\alpha = 1, 2$) obtained by a generalization of the dipole relaxation equation (2.12). For sphere 1:

$$\frac{d\mathbf{P}_1}{dt} = \mathbf{\Omega}_1 \times [\mathbf{P}_1 + a^3 \varepsilon_{21} \nabla \phi_e^1(\mathbf{x}_1)] - \frac{1}{\tau_{\mathrm{MW}}} [\mathbf{P}_1 + a^3 \sigma_{21} \nabla \phi_e^1(\mathbf{x}_1)], \tag{2.35}$$

and a similar equation can also be written for the dipole moment $\mathbf{P}_2$ of the second sphere. A relaxation equation based on Eq. (2.13) can also be written for the quadrupole moment $\mathbf{Q}_\alpha$ induced in each sphere, though we will show below that it can be neglected to leading order. In Eq. (2.35), $\nabla \phi_e^1(\mathbf{x}_1)$ denotes the external electric field (up to a minus sign) experienced by sphere 1. This electric field includes the applied uniform field $\mathbf{E}_0$, as well as a correction arising from the potential disturbance $\phi_d^{+2}(\mathbf{x})$ induced by the various multipoles generated inside sphere 2. To leading order, according to Eq. (2.10):

$$\phi_d^{+2}(\mathbf{x}) = \frac{(\mathbf{x} - \mathbf{x}_2) \cdot \mathbf{P}_2}{|\mathbf{x} - \mathbf{x}_2|^3} + ... \tag{2.36}$$

which can be expanded on the basis of growing spherical harmonics near the center of sphere 1 to obtain the correction to the applied field. All calculations done, the potential gradient $\nabla\phi_e^1(\mathbf{x}_1)$ appearing in Eq. (2.35) can be shown to be of the form

$$\nabla\phi_e^1(\mathbf{x}_1) = -\mathbf{E}_0 + \frac{1}{R^3}\boldsymbol{\Pi}\cdot\mathbf{P}_2 + O(R^{-8}), \tag{2.37}$$

where we have introduced the second-order tensorial operator $\boldsymbol{\Pi} = \mathbf{I} - 3\widehat{\mathbf{R}}\widehat{\mathbf{R}}$. The error in Eq. (2.37), which arises from neglecting the contributions of the quadrupole moment and higher multipoles to the disturbance potential, can be estimated to be of order $O(R^{-8})$. Indeed, because the applied field is uniform, the leading-order quadrupole moment induced inside the spheres arises from the second gradient of the disturbance potential ϕ_d^+ resulting from the dipole moments and is therefore of order $|\mathbf{Q}_\alpha| = O(R^{-4})$ as can be seen from Eq. (2.36). The quadrupole moment then adds an $O(R^{-7})$ correction to the disturbance potential [see Eq. (2.10)], corresponding to an $O(R^{-8})$ correction to the potential gradient in Eq. (2.37).

Torque balance

To determine the angular velocity $\boldsymbol{\Omega}_1$ appearing in Eq. (2.35), we consider the torque balance on sphere 1 in the inertialess limit, where the angular velocity of sphere 1 is modified by the hydrodynamic velocity $\mathbf{u}_2(\mathbf{x})$ induced by the motion of sphere 2 [82]:

$$\mathbf{T}_1^e - 8\pi\eta a^3\left[\boldsymbol{\Omega}_1 - \frac{1}{2}\nabla\times\mathbf{u}_2(\mathbf{x}_1)\right] = 0. \tag{2.38}$$

Here, $\mathbf{T}_1^e$ is the electric torque on sphere 1:

$$\mathbf{T}_1^e = -4\pi\varepsilon_1 \mathbf{P}_1 \times \nabla\phi_e^1(\mathbf{x}_1) + O(R^{-8}), \tag{2.39}$$

where $\nabla\phi_e^1(\mathbf{x}_1)$ is given in Eq. (2.37), and where we have neglected the torque induced by the quadrupole moment [77]. To leading order, $\mathbf{u}_2(\mathbf{x})$ is given by the rotlet flow driven be the rotation of sphere 2 with angular velocity $\mathbf{\Omega}_2$ [82]:

$$\mathbf{u}_2(\mathbf{x}) = a^3 \mathbf{\Omega}_2 \times \frac{(\mathbf{x} - \mathbf{x}_2)}{|\mathbf{x} - \mathbf{x}_2|^3} + O(R^{-5}), \tag{2.40}$$

with vorticity at the location of sphere 1 given by:

$$\nabla \times \mathbf{u}_2(\mathbf{x}_1) = -\frac{a^3}{R^3} \mathbf{\Pi} \cdot \mathbf{\Omega}_2 + O(R^{-6}). \tag{2.41}$$

The order of the error in Eqs. (2.40)–(2.41) can be understood as follows: the rotlet flow $\mathbf{u}_1$ generated by sphere 1, which scales like $O(R^{-2})$ at the center of sphere 2, induces a stresslet on sphere 2, whose magnitude scales with the gradient of $\mathbf{u}_1$ as $O(R^{-3})$ and adds a contribution to $\mathbf{u}_2$ in Eq. (2.40) that decays like $O(R^{-5})$. Substituting Eqs. (2.39) and (2.41) into the torque balance Eq. (2.38) yields

$$\mathbf{\Omega}_1 + \frac{a^3}{2R^3} \mathbf{\Pi} \cdot \mathbf{\Omega}_2 = -\frac{\varepsilon_1}{2\eta a^3} \mathbf{P}_1 \times \nabla\phi_e^1(\mathbf{x}_1) + O(R^{-6}), \tag{2.42}$$

and a similar equation can be written for the torque balance on sphere 2. These two coupled linear equations for $\mathbf{\Omega}_1$ and $\mathbf{\Omega}_2$ are easily solved analytically to leading order

as:

$$\mathbf{\Omega}_1 = \frac{\varepsilon_1}{2\eta a^3}\left\{\mathbf{P}_1 \times \left(\mathbf{E}_0 - \frac{1}{R^3}\mathbf{\Pi}\cdot\mathbf{P}_2\right) - \frac{a^3}{2R^3}\mathbf{\Pi}\cdot\left[\mathbf{P}_2 \times \left(\mathbf{E}_0 - \frac{1}{R^3}\mathbf{\Pi}\cdot\mathbf{P}_1\right)\right]\right\}, \quad (2.43)$$

$$\mathbf{\Omega}_2 = \frac{\varepsilon_1}{2\eta a^3}\left\{\mathbf{P}_2 \times \left(\mathbf{E}_0 - \frac{1}{R^3}\mathbf{\Pi}\cdot\mathbf{P}_1\right) - \frac{a^3}{2R^3}\mathbf{\Pi}\cdot\left[\mathbf{P}_1 \times \left(\mathbf{E}_0 - \frac{1}{R^3}\mathbf{\Pi}\cdot\mathbf{P}_2\right)\right]\right\}, \quad (2.44)$$

where the error in both equations is of order $O(R^{-6})$. Note that the last term in Eqs. (2.43)–(2.44) is itself of order $O(R^{-6})$; we retain it nonetheless as it is required for $\mathbf{\Omega}_1 = \mathbf{\Omega}_2 = \mathbf{0}$ to be an exact steady solution of the equations derived here.

Force balance

In the case of two freely suspended particles, translational motion is also expected to occur as a result of dielectrophoretic forces on the particles. Such forces were previously analyzed in detail using the method of reflections [170, 77, 137], and can be expressed as

$$\mathbf{F}_1 = -4\pi\varepsilon_1\left[\mathbf{P}_1\cdot\nabla\nabla\phi_e^1(\mathbf{x}_1) + \frac{1}{6}\mathbf{Q}_1 : \nabla\nabla\nabla\phi_e^1(\mathbf{x}_1) + ...\right], \quad (2.45)$$

with a similar expression for $\mathbf{F}_2$. To leading order, this expression simplifies to

$$\begin{aligned}\mathbf{F}_1 = -\frac{12\pi\varepsilon_1}{R^4}[&(\mathbf{P}_1\cdot\widehat{\mathbf{R}})\mathbf{P}_2 + (\mathbf{P}_2\cdot\widehat{\mathbf{R}})\mathbf{P}_1 + (\mathbf{P}_1\cdot\mathbf{P}_2)\widehat{\mathbf{R}} \\ &- 5(\mathbf{P}_1\cdot\widehat{\mathbf{R}})(\mathbf{P}_2\cdot\widehat{\mathbf{R}})\widehat{\mathbf{R}}] + O(R^{-9}),\end{aligned} \quad (2.46)$$

and by symmetry $\mathbf{F}_2 = -\mathbf{F}_1$. This dielectrophoretic force then enters the force balance on the sphere. Neglecting inertia, the force balance on sphere 1 is written

$$6\pi\eta a\left[\mathbf{U}_1 - \mathbf{u}_2(\mathbf{x}_1) - \frac{a^2}{6}\nabla^2\mathbf{u}_2(\mathbf{x}_1)\right] = \mathbf{F}_1. \tag{2.47}$$

where the translational velocity $\mathbf{U}_1$ of the sphere is also modified by the flow field $\mathbf{u}_2$ induced by sphere 2 according to Faxén's law [82]. Noting that $\nabla^2\mathbf{u}_2(\mathbf{x}_1) = O(R^{-7})$, this yields the following expression for the particle velocities:

$$\mathbf{U}_1 = -\frac{a^3}{R^2}\mathbf{\Omega}_2 \times \widehat{\mathbf{R}} + \frac{\mathbf{F}_1}{6\pi\eta a} + O(R^{-5}), \tag{2.48}$$

$$\mathbf{U}_2 = \frac{a^3}{R^2}\mathbf{\Omega}_1 \times \widehat{\mathbf{R}} + \frac{\mathbf{F}_2}{6\pi\eta a} + O(R^{-5}). \tag{2.49}$$

In these equations, the leading-order error arises due to the Stokeslet flows driven by forces $\mathbf{F}_1$ and $\mathbf{F}_2$, which modify the velocities to order $O(R^{-5})$ and could easily be included for higher accuracy. The translational motion arises from two different processes: first, the spheres are advected by the rotlet flows they generate, which can lead to orbiting motions as we will see in numerical simulations in Sec. 2.4.2; second, dielectrophoretic forces cause relative motions that can be either attractive or repulsive depending on the orientation of the electric dipoles on the spheres.

Non-dimensionalization and summary of the governing equations

In the remainder of the paper, we scale all variables using the particle radius a, Maxwell-Wagner relaxation time τ_{MW}, and applied electric field strength E_0 as characteristic scales for length, time, and electric field, respectively. Under these scalings, one dimensionless group appears in the equations, which is the electric Mason

number Ma characterizing the ratio of viscous to polarization forces:

$$\mathrm{Ma} = \frac{\eta}{\tau_{\mathrm{MW}} \varepsilon_1 E_0^2}. \tag{2.50}$$

The Mason number is directly related to the ratio of the applied field strength to the critical electric field E_c^0 for the onset of Quincke rotation of a single particle in the absence of interactions as

$$\mathrm{Ma} = \frac{\varepsilon_{21} - \sigma_{21}}{2} \left(\frac{E_c^0}{E_0} \right)^2. \tag{2.51}$$

After non-dimensionalization, the governing equations can be summarized as follows. The electric dipoles $\mathbf{P}_1$ and $\mathbf{P}_2$ satisfy the two coupled ordinary differential equations:

$$\frac{d\mathbf{P}_1}{dt} = \boldsymbol{\Omega}_1 \times \left[\mathbf{P}_1 + \varepsilon_{21} \left(-\widehat{\mathbf{z}} + \frac{1}{R^3} \boldsymbol{\Pi} \cdot \mathbf{P}_2 \right) \right] - \left[\mathbf{P}_1 + \sigma_{21} \left(-\widehat{\mathbf{z}} + \frac{1}{R^3} \boldsymbol{\Pi} \cdot \mathbf{P}_2 \right) \right], \tag{2.52}$$

$$\frac{d\mathbf{P}_2}{dt} = \boldsymbol{\Omega}_2 \times \left[\mathbf{P}_2 + \varepsilon_{21} \left(-\widehat{\mathbf{z}} + \frac{1}{R^3} \boldsymbol{\Pi} \cdot \mathbf{P}_1 \right) \right] - \left[\mathbf{P}_2 + \sigma_{21} \left(-\widehat{\mathbf{z}} + \frac{1}{R^3} \boldsymbol{\Pi} \cdot \mathbf{P}_1 \right) \right]. \tag{2.53}$$

The angular velocities $\boldsymbol{\Omega}_1$ and $\boldsymbol{\Omega}_2$ can also be expressed in terms of the dipole moments through the torque balance on each sphere as

$$\boldsymbol{\Omega}_1 = \frac{1}{2\mathrm{Ma}} \left\{ \mathbf{P}_1 \times \left(\widehat{\mathbf{z}} - \frac{1}{R^3} \boldsymbol{\Pi} \cdot \mathbf{P}_2 \right) - \frac{1}{2R^3} \boldsymbol{\Pi} \cdot \left[\mathbf{P}_2 \times \left(\widehat{\mathbf{z}} - \frac{1}{R^3} \boldsymbol{\Pi} \cdot \mathbf{P}_1 \right) \right] \right\}, \tag{2.54}$$

$$\boldsymbol{\Omega}_2 = \frac{1}{2\mathrm{Ma}} \left\{ \mathbf{P}_2 \times \left(\widehat{\mathbf{z}} - \frac{1}{R^3} \boldsymbol{\Pi} \cdot \mathbf{P}_1 \right) - \frac{1}{2R^3} \boldsymbol{\Pi} \cdot \left[\mathbf{P}_1 \times \left(\widehat{\mathbf{z}} - \frac{1}{R^3} \boldsymbol{\Pi} \cdot \mathbf{P}_2 \right) \right] \right\}. \tag{2.55}$$

Finally, if the spheres are freely suspended, their translational velocities are given by

$$\begin{aligned}\mathbf{U}_1 = &-\frac{1}{R^2}\boldsymbol{\Omega}_2 \times \widehat{\mathbf{R}} - \frac{4}{2\mathrm{Ma}\, R^4}[(\mathbf{P}_1 \cdot \widehat{\mathbf{R}})\mathbf{P}_2 + (\mathbf{P}_2 \cdot \widehat{\mathbf{R}})\mathbf{P}_1 \\ &+ (\mathbf{P}_1 \cdot \mathbf{P}_2)\widehat{\mathbf{R}} - 5(\mathbf{P}_1 \cdot \widehat{\mathbf{R}})(\mathbf{P}_2 \cdot \widehat{\mathbf{R}})\widehat{\mathbf{R}}]\end{aligned} \tag{2.56}$$

$$\begin{aligned}\mathbf{U}_2 = &\frac{1}{R^2}\boldsymbol{\Omega}_1 \times \widehat{\mathbf{R}} + \frac{4}{2\mathrm{Ma}\, R^4}[(\mathbf{P}_1 \cdot \widehat{\mathbf{R}})\mathbf{P}_2 + (\mathbf{P}_2 \cdot \widehat{\mathbf{R}})\mathbf{P}_1 \\ &+ (\mathbf{P}_1 \cdot \mathbf{P}_2)\widehat{\mathbf{R}} - 5(\mathbf{P}_1 \cdot \widehat{\mathbf{R}})(\mathbf{P}_2 \cdot \widehat{\mathbf{R}})\widehat{\mathbf{R}}].\end{aligned} \tag{2.57}$$

Equations (2.52)–(2.53) form a system of coupled nonlinear ordinary differential equations for the dipole moments, that are also coupled to Eqs. (2.54)–(2.57) for the angular and translational motions of the spheres. This system of equations can analyzed theoretically as we do next in Sec. 2.3, or integrated numerically as will be discussed in Sec. 2.4.

2.3 Linear stability analysis

We first analyze the effects of electrohydrodynamic interactions on the onset of Quincke rotation by performing a linear stability analysis on the equations of Sec. 4.4 in the case where the two spheres are held fixed in space, so that the separation vector $\mathbf{R}$ does not change in time and the spheres only undergo rotational motion. In this case, the system of equations reduces to Eqs. (2.52)–(2.55). A steady base state exists in the absence of rotation: $\boldsymbol{\Omega}_1 = \boldsymbol{\Omega}_2 = \mathbf{0}$, in which case both dipole moments assume

the same steady value $\mathbf{P}_0$ obtained by solution of Eqs. (2.52)–(2.53):

$$\mathbf{P}_1 = \mathbf{P}_2 = \mathbf{P}_0 = \frac{\sigma_{21}}{1 + \dfrac{\sigma_{21}}{R^3}} \left(\mathbf{I} + \frac{3\sigma_{21}}{R^3 - 2\sigma_{21}} \widehat{\mathbf{R}}\widehat{\mathbf{R}} \right) \cdot \widehat{\mathbf{z}}. \tag{2.58}$$

In this equation, we see that electric interactions modify the steady dipole with a correction scaling as $O(R^{-3})$ that can have a non-zero component perpendicular to the field depending on the orientation of the spheres. Next, we perturb the steady-state dipole by a small amount:

$$\mathbf{P}_1(t) = \mathbf{P}_0 + \epsilon \mathbf{p}_1(t), \quad \mathbf{P}_2(t) = \mathbf{P}_0 + \epsilon \mathbf{p}_2(t), \tag{2.59}$$

which induces weak rotations:

$$\mathbf{\Omega}_1(t) = \epsilon \boldsymbol{\omega}_1(t), \quad \mathbf{\Omega}_2(t) = \epsilon \boldsymbol{\omega}_2(t). \tag{2.60}$$

Linearization of the governing equations easily yields a homogeneous system of coupled linear ordinary differential equations for the perturbation dipoles:

$$\frac{d\mathbf{p}_1}{dt} = \left(1 - \frac{\varepsilon_{21}}{\sigma_{21}} \right) \boldsymbol{\omega}_1 \times \mathbf{P}_0 - \mathbf{p}_1 - \frac{\sigma_{21}}{R^3} \mathbf{\Pi} \cdot \mathbf{p}_2, \tag{2.61}$$

with a similar equation for $\mathbf{p}_2(t)$. In Eq. (2.61), the linearized angular velocity $\boldsymbol{\omega}_1$ is expressed as

$$\begin{aligned} \boldsymbol{\omega}_1 = \frac{1}{2\mathrm{Ma}} \Bigg\{ & \frac{1}{\sigma_{21}} \mathbf{p}_1 \times \mathbf{P}_0 - \frac{1}{R^3} \mathbf{P}_0 \times (\mathbf{\Pi} \cdot \mathbf{p}_2) \\ & - \frac{1}{2R^3} \mathbf{\Pi} \cdot \left[\frac{1}{\sigma_{21}} \mathbf{p}_2 \times \mathbf{P}_0 - \frac{1}{R^3} \mathbf{P}_0 \times (\mathbf{\Pi} \cdot \mathbf{p}_1) \right] \Bigg\}. \end{aligned} \tag{2.62}$$

with a similar expression for $\boldsymbol{\omega}_2$. Eqs. (2.61)–(2.62), together with equivalent expressions for $\mathbf{p}_2$ and $\boldsymbol{\omega}_2$, can be written in the form

$$\frac{d}{dt}\begin{bmatrix} \mathbf{p}_1 \\ \mathbf{p}_2 \end{bmatrix} = \mathbf{J}(\mathrm{Ma}, \varepsilon_{21}, \sigma_{21}, \mathbf{R}) \cdot \begin{bmatrix} \mathbf{p}_1 \\ \mathbf{p}_2 \end{bmatrix}, \tag{2.63}$$

where the 6×6 Jacobian matrix $\mathbf{J}$ is a function of the Mason number Ma (or equivalently of E_0/E_c^0), of the dimensionless material parameters ε_{21} and σ_{21}, and of the dimensionless separation vector $\mathbf{R}$ between the two spheres. Note that while the matrix $\mathbf{J}$ depends on the separation vector $\mathbf{R}$, its eigenvalues really only depend on the dimensionless distance R between the sphere centers and on the angle $\Theta = \cos^{-1}(\widehat{\mathbf{R}} \cdot \hat{\mathbf{z}})$ defining the orientation of the sphere pair with respect to the external field direction. The explicit form of $\mathbf{J}$, which is quite cumbersome, is omitted here for brevity.

The eigenvalues λ of the Jacobian $\mathbf{J}$, which can be calculated numerically, determine the stability of the base state with no rotation. Their real parts are the actual growth rates, and a positive growth rate indicates the exponential growth of any small perturbation of the base-state dipole moment of Eq. (2.58), subsequently leading to Quincke rotation of the particles. A numerical solution of the eigenvalue problem shows that the Jacobian has six real eigenvalues, which are all negative when there is no electric field. As the field strength is increased, some of them become positive indicating the onset of Quincke rotation. The critical field value E_c above which instability occurs is plotted as a function of the orientation Θ of the spheres in Fig. 2.5(a), where it is normalized by the critical field E_c^0 obtained in Eq. (2.33) in the absence of interactions. The effect of interactions is subtle and can either increase or decrease the value of the critical electric field depending on Θ: for spheres that are

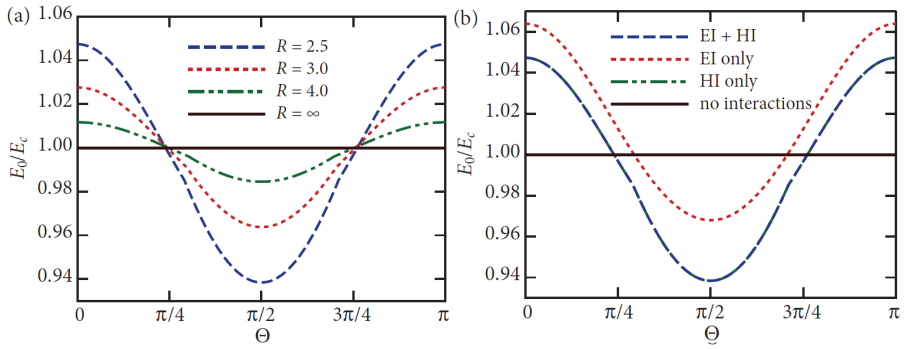

Figure 2.5: Results of the linear stability analysis. (a) Critical electric field E_c in the presence of interactions (normalized by the critical field E_c^0 for onset of Quincke rotation of an isolated particle) as a function of the orientation angle Θ between the pair of spheres and the field direction, for various values of the separation distance R. (b) Critical electric field E_c/E_c^0 as a function of Θ for $R = 2.5$, when either electric interactions (EI), hydrodynamic interactions (HI), or both are taken into account. In this figure, the materials parameters ε_{21} and σ_{21} were chosen as in the recent experiments of Lemaire and coworkers [98, 95, 112, 96] to be $\varepsilon_{21} = -0.1097$ and $\sigma_{21} = -0.5$.

nearly aligned with the field (Θ close to 0 or π), the critical electric field increases, corresponding to a stabilizing effect of interactions, whereas it decreases when the pair of spheres is aligned in a direction perpendicular to the applied field (Θ close to $\pi/2$), corresponding to a destabilizing effect. These effects are clearest when the particles are close to one another, and as the distance R increases, the critical electric field asymptotically tends to the critical field E_c^0 for an isolated sphere. The dependence of E_c on R can also be probed and shows that $E_c/E_c^0 - 1 = O(R^{-3})$ for $R \gg 1$, as could have been anticipated from the form of the governing equations.

The respective roles of electric and hydrodynamic interactions on the stability can be further analyzed by solving two additional eigenvalue problems in which either type of interaction is turned off. The results for the critical field in these various cases are plotted in Fig. 2.5(b), for a fixed distance of $R = 2.5$. When only electric interactions are taken into account, the critical electric field shows a similar dependence

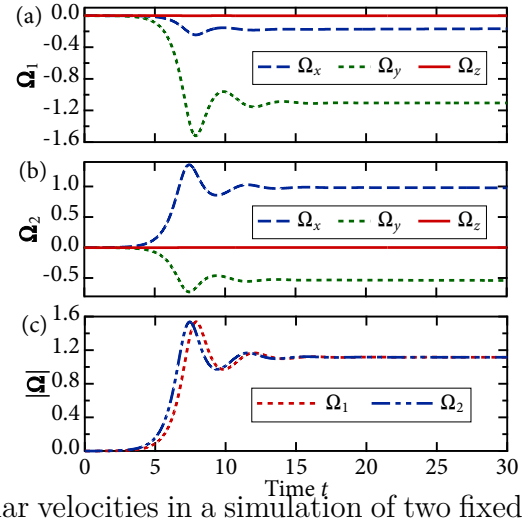

Figure 2.6: Angular velocities in a simulation of two fixed interacting spheres separated by a distance $R = 10$ undergoing Quincke rotation in an applied electric field of magnitude $E_0 = 1.5\, E_c^0$: (a) angular velocity $\mathbf{\Omega}_1$ of the first sphere as a function of time; (b) angular velocity $\mathbf{\Omega}_2$ of the second sphere; (c) angular velocity magnitudes.

on Θ as when both types of interactions are included, indicating a stabilizing effect of electric interactions for a pair of spheres aligned with the field but a destabilizing effect for spheres aligned perpendicular to the field; however, the critical value of the electric field is always larger than when hydrodynamic interactions are included, suggesting that hydrodynamic interactions play a more important role in the onset of rotation than electric interactions. This is indeed confirmed when electric interactions are turned off, in which case the critical electric field E_c is the same as for the full system of equations: this curious observation suggests that hydrodynamic modes are the ones that govern the modification of the onset of instability by interactions.

2.4 Numerical simulations

While the linear stability analysis of Sec. 2.3 provided results on the onset of rotation in the presence of interactions, nonlinear dynamics can only be studied

numerically. In this section, we present results from numerical simulations of the unsteady governing equations, which were integrated using a fourth-order Runge-Kutta time-marching scheme. We first consider the case of two spheres that are fixed in space but free to rotate in Sec. 2.4.1, and then turn to the case of freely suspended spheres in Sec. 2.4.2. In all simulations, the initial dipole moments are given by Eq. (2.58) but are weakly perturbed by infinitesimal random vectors with components of magnitude of the order of 10^{-3}. For both fixed and freely suspended spheres, we note a very strong sensitivity of the solution on the infinitesimal initial perturbation introduced in the system. Therefore, we focus the discussion on a few representative cases as well as on the statistics for the steady states obtained over many realizations with different random initial perturbations. In all of this section, the two dimensional material constants ε_{21} and σ_{21} are set to $\varepsilon_{21} = -0.1097$ and $\sigma_{21} = -0.5$, which correspond to the experiments of Lemaire and coworkers [98, 95, 112, 96] and were also the values used by Huang *et al.* [69].

2.4.1 Fixed spheres

A typical simulation in the case of two fixed spheres in a field of magnitude $E_0 = 1.5\, E_c^0$ is shown in Fig. 2.6, where both the components and magnitude of the angular velocities are plotted as functions of time. The infinitesimal perturbation introduced to the system at $t = 0$ is found to amplify with time and lead to the growth of the angular velocities, which briefly oscillate and reach steady values. The steady-state angular velocities are always found to have zero components in the field direction as in the single-sphere case. Quite interestingly, the magnitudes Ω_1 and Ω_2 of the angular velocities are found to converge to the same value, even though

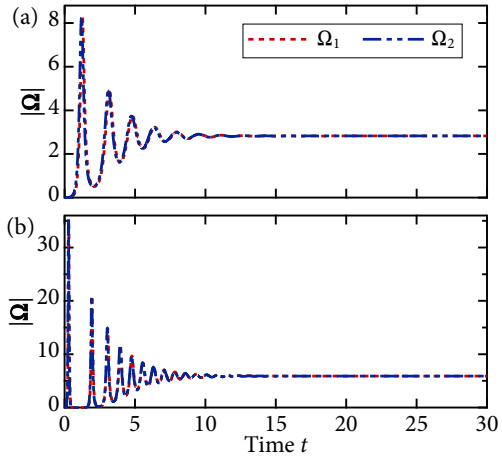

Figure 2.7: Angular velocities as functions of time in two simulations with $R = 10$ at different field strengths: (a) $E_0/E_c^0 = 3.0$, (b) $E_0/E_c^0 = 6.0$.

the directions of rotation are not the same. This peculiar result, which we cannot explain theoretically, is observed systematically in all simulations. The final direction of rotation in the x-y plane depends sensitively on the initial perturbation, but the steady magnitude of the angular velocity varies only weakly between simulations at fixed values of R, Θ, and E_0. The effect of further increasing the electric field is shown in Fig. 2.7, where Ω_1 and Ω_2 for two simulations with $E_0/E_c^0 = 3.0$ and 6.0. We find that stronger fields result in stronger and faster oscillations during the initial transient, but these oscillations always subside and give way to synchronization of the angular velocity magnitudes.

Next, we analyze statistics on the steady angular velocity reached after the initial transient oscillations. We report averages over larger numbers ($\geq$ 200) of simulations with different small random initial perturbations. Throughout this section, we also compare these statistics to an asymptotic estimate of the steady-state angular velocity derived in Appendix A.1 in the case of co-rotating spheres in the limit of $R \gg 1$:

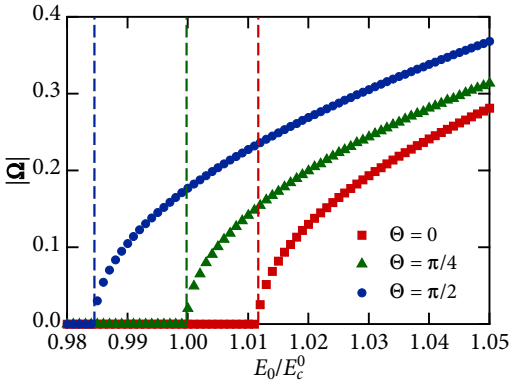

Figure 2.8: Onset of Quincke rotation of two interacting spheres: the plot shows the average steady-state angular velocity as a function of the applied electric field E_0 for two spheres separated by a distance $R = 4.0$ and for various orientations Θ. The vertical dashed lines show the critical electric field strengths E_c/E_c^0 for onset of rotation predicted by the linear stability analysis of Sec. 2.3.

$$\langle \Omega^2 \rangle = \Omega_0^2 + \frac{1 + 3\cos 2\Theta}{R^3} \left[\varepsilon_{21} \left(\frac{E_0}{E_c^0} \right)^2 + (\sigma_{21} - \varepsilon_{21}) \right], \tag{2.64}$$

where $\Omega_0^2 = (E_0/E_c^0)^2 - 1$ denotes to the steady-state angular velocity of an isolated sphere.

The onset of Quincke rotation in the case of two interacting spheres is illustrated in Fig. 2.8, where the steady-state angular velocity magnitude is plotted as a function of the applied field and is seen to undergo a pitchfork bifurcation at a critical electric field. The plot shows the average steady-state angular velocity as a function of the applied electric field E_0 for two spheres separated by a distance $R = 4.0$ and for various orientations Θ. The vertical dashed lines show the critical electric field strengths E_c/E_c^0 for onset of rotation predicted by the linear stability analysis of Sec. 2.3. In excellent agreement with the results of the linear stability analysis of Sec. 2.3, the value of the critical electric field depends on the orientation Θ of the spheres, with $\Theta = 0$ as the most stable orientation and $\Theta = \pi/2$ as the most unstable one. As the distance R between the two spheres increases, the value of Ω converges towards the

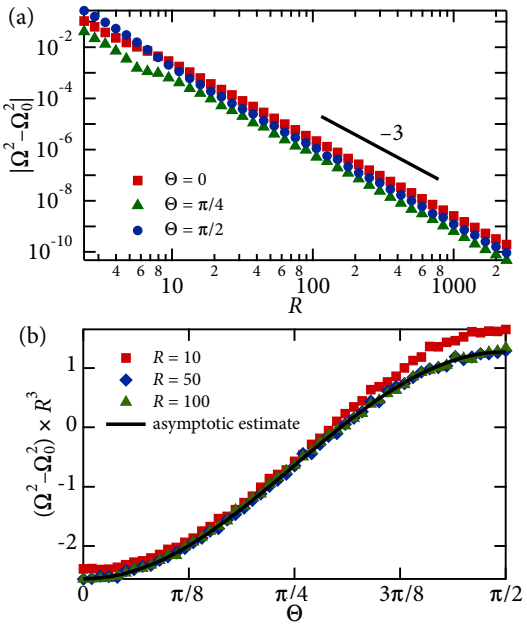

Figure 2.9: Dependence of the deviation $(\Omega^2 - \Omega_0^2)$ of the steady-state angular from the isolated sphere value as a function of (a) the distance R between the spheres, and (b) the orientation Θ of the sphere pair with respect to the field direction. Both plots were obtained for $E_0/E_c^0 = 1.5$. In (b), the simulation results are compared to the asymptotic result of Eq. (2.64).

single-sphere solution Ω_0 with a bifurcation at $E_0 = E_c^0$.

The precise dependence of the steady-state angular velocity on R and Θ is shown in Fig. 2.9. The deviation $\Omega^2 - \Omega_0^2$ between the angular velocity in the presence of interactions and that of an isolated sphere is plotted in Fig. 2.9(a) and is observed to decay rapidly as $1/R^3$, as could have easily been anticipated from the form of the governing equations and in agreement with the asymptotic estimate of Eq. (2.64). The sign of this deviation depends again on the orientation of the spheres: interactions tend to decrease the rate of rotation for spheres aligned with the field direction and increase it for spheres aligned in a perpendicular direction. The functional dependence on Θ is plotted in Fig. 2.9(b) and agrees quite well with Eq. (2.64) as soon as $R \gtrsim 10$. Both plots were obtained for $E_0/E_c^0 = 1.5$. In 2.9(b), the simulation results are compared to the asymptotic result of Eq. (2.64).

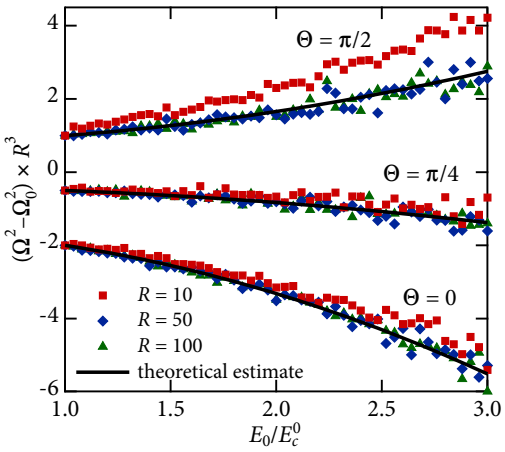

Figure 2.10: Dependence of $(\Omega^2 - \Omega_0^2) \times R^3$ on electric field strength E_0 above the onset of Quincke rotation, for different values of Θ and R. The simulation results are compared to the asymptotic prediction of Eq. (2.64).

Figure 2.10 shows the effect of field strength E_0 on the angular velocity above the bifurcation. Increasing field strength increases the effect of interactions with a quadratic dependence on E_0/E_c^0, and all the results for different values of Θ and R are found to collapse remarkably well onto the asymptotic approximation of Eq. (2.64), which provides an excellent prediction for the angular velocity regardless of the directions of rotation when R is sufficiently large.

2.4.2 Freely-suspended spheres

We now turn our attention to the dynamics of freely suspended spheres, whose relative motion results from the combination of the rotlet flows generated by the sphere rotations and of the dielectrophoretic forces (dipole-dipole interactions) as discussed in Sec. 2.2.2. As we show below, dielectrophoretic forces can result in the pairing of the particles, in which case we implement a contact algorithm to prevent particle overlap. The algorithm assumes rolling without slipping between the two sphere surfaces and is explained in more detail in Appendix A.2. It should be kept in

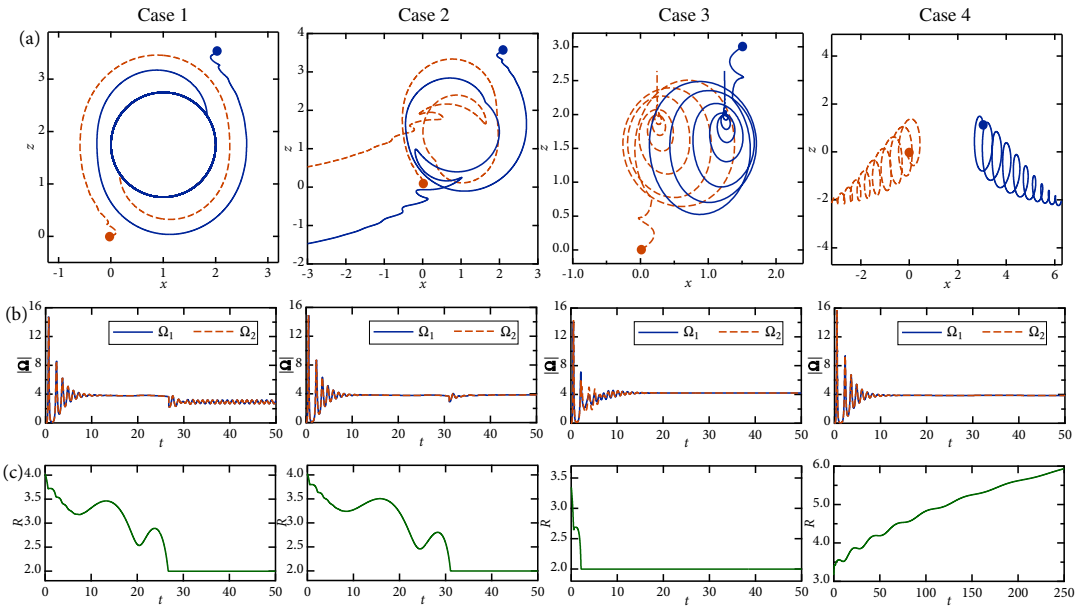

Figure 2.11: Dynamics of freely suspended spheres: (a) typical particle trajectories (where the two dots mark the initial position of the particles), (b) magnitude of the angular velocities vs time, and (c) separation distance vs time. Depending on the relative position of the spheres and on the infinitesimal initial perturbation introduced in the system, four different types of motions are observed, as illustrated in cases 1 to 4. In this plot, $E_0/E_c^0 = 4.0$, $\varepsilon_{21} = -0.1097$ and $\sigma_{21} = -0.5$.

mind that the calculation of electrohydrodynamic interactions used here is based on the assumption of widely separated spheres, and is therefore likely inaccurate when the two particles are near contact. This should be borne in mind when analyzing the simulations presented here, though we do not anticipate the results to change qualitatively if a more accurate calculation of interactions were used (for instance based on a boundary integral formulation).

As in the case of fixed spheres, we observe a strong sensitivity of the dynamics to the initial perturbation introduced in the system at $t = 0$. Using numerical experiments, we have identified four different types of qualitatively different behaviors, which are illustrated in Fig. 2.11. Depending on the relative position of the spheres and on the infinitesimal initial perturbation introduced in the system, four different types of motions are observed, as illustrated in cases 1 to 4. In this plot, $E_0/E_c^0 = 4.0$, $\varepsilon_{21} = -0.1097$ and $\sigma_{21} = -0.5$. Case 1 corresponds to the somewhat artificial situation where no perturbation is introduced in the system. In this case, the motion of the two spheres as a result of dielectrophoresis is sufficient to destabilize the system and induce rotation. The dynamics of the sphere pair is perfectly two-dimensional, and the particles are observed to undergo a spiraling motion during which their separation distance decreases leading to pairing up. The spiraling motion, which is observed in many trajectories (including in cases 2 and 3), is a consequence of the rotlet flows generated by the spinning spheres. Upon pairing, the spheres in case 1 continue to orbit around one another ad infinitum. In a physical system, small perturbations are expected to occur leading to cases 2, 3 and 4. In cases 2 and 3, the particles are also observed to pair up, though their motion is three-dimensional. In case 2, pairing up eventually leads to alignment of the two spheres in the direction of the applied field

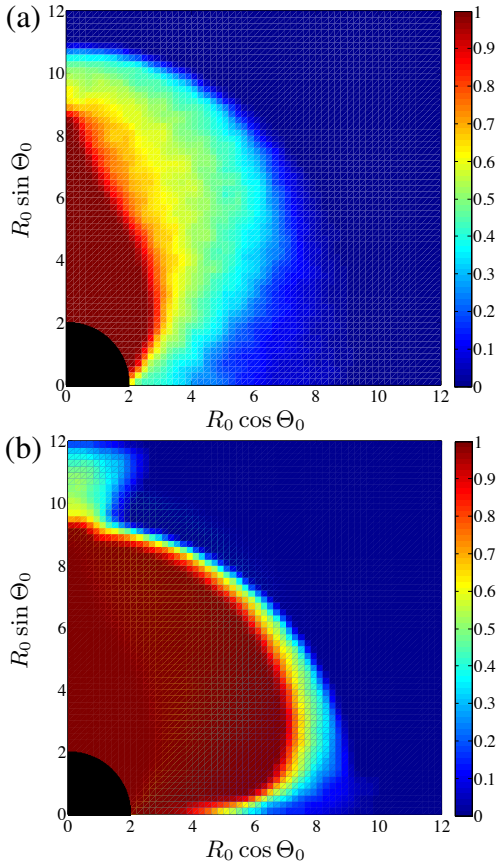

Figure 2.12: Probability of the two spheres pairing up (cases 1, 2, and 3) vs separating (case 4) as a function of $R_0 = |\mathbf{R}_0|$ and $\Theta_0 = \cos^{-1}(\mathbf{R}_0 \cdot \hat{\mathbf{z}}/R_0)$, where $\mathbf{R}_0 = \mathbf{R}(t = 0)$ is the initial separation vector between the spheres: (a) $E_0/E_c^0 = 4.0$, and (b) $E_0/E_c^0 = 6.0$. The black quarter disk centered at the origin corresponds to the region of excluded volume.

and counter-rotation in a normal direction, which causes them to translate as a pair in a horizontal direction at a constant velocity once steady state has been reached. In case 3, which is found to occur most rarely, pairing of the spheres leads to orbiting motions that eventually stabilize to a steady configuration in which the spheres are aligned in a direction perpendicular to the electric field and co-rotate around their axis of centers while remaining stationary in space. Finally, in case 4 the two spheres do not pair up but rather slowly separate in space as a result of dipolar interactions while steadily rotating.

The outcome of a particular simulation is difficult to predict based solely on the initial configuration of the spheres, as different infinitesimal perturbations can lead to any of cases 2 to 4. To quantify this subtle dependence, we show in Fig. 2.12(a) the probability of pairing (cases 1, 2, and 3) vs separation (case 4) as a function of the initial distance R_0 between the spheres and of their initial orientation Θ_0 with respect to the field direction, for the same electric field strength as in Fig. 2.11 ($E_0/E_c^0 = 0.4$). We observe that initial configurations in which the spheres are initially nearly aligned with the electric field are more likely to lead to particle pairing, which could have been anticipated based on the form of the dielectrophoretic forces which are attractive for such configurations [137, 115, 116]. However, many initial values of R_0 and Θ_0 are seen to equally lead to either pairing or separation. The effect of increasing field strength is shown in Fig. 2.12(b), where the pairing probability is plotted for $E_0/E_c^0 = 6.0$. In this stronger field, we find that the region of high pairing probability extends further away from the field axis, indicating a stronger likelihood of pairing events at high values of E_0. The black quarter disk centered at the origin in these plots corresponds to the region of excluded volume. Typical trajectories for the value of $E_0/E_c^0 = 6.0$ are shown in Fig. 2.13. These trajectories, which correspond to cases 2 and 3, show similar characteristics as in Fig. 2.11 but exhibit stronger orbiting motions, which we find to be a feature of all simulations in strong fields.

2.5 Conclusion

In summary, we have developed an analytical model for the Quincke rotation of a pair of identical spherical particles that are interacting both electrically and hydrodynamically. The modeling of Quincke rotation is based on the classic Taylor-

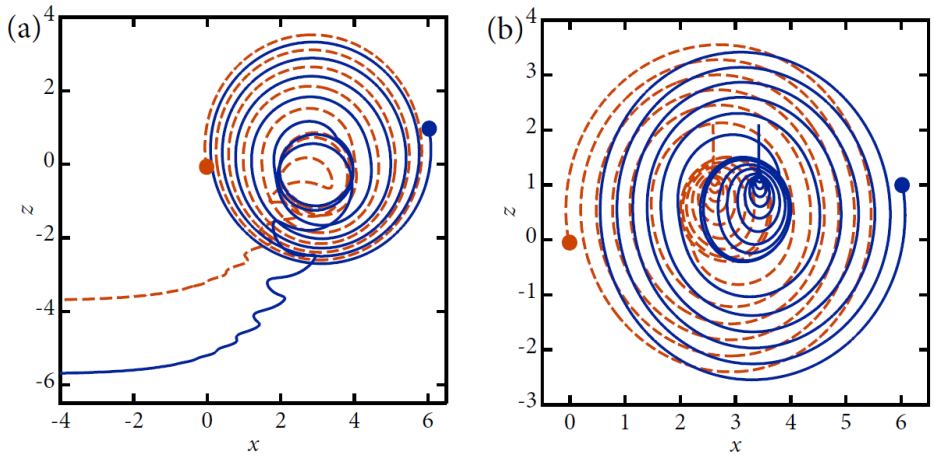

Figure 2.13: Typical particle trajectories for $E_0/E_c^0 = 6.0$, $\varepsilon_{21} = -0.1097$ and $\sigma_{21} = -0.5$: plots (a) and (b) show two different types of trajectories corresponding, respectively, to cases 2 and 3 of Fig. 2.11. In this plot, the two dots mark the initial positions of the particles.

Melcher leaky dielectric model and on an asymptotic description of interactions using the method of reflections, which is valid for widely separated particles. We have only retained leading-order electric and hydrodynamic effects, which result from electric dipole-dipole interactions and from hydrodynamic rotlet interactions due to the spinning of the spheres, respectively, and we note that both types of interactions modify the dipoles and angular velocities of the spheres to order $O(R^{-3})$. Using a linear stability analysis in the case where the two spheres are fixed in space, we have shown that interactions can either have a stabilizing or destabilizing effect on the onset for rotation depending on the orientation of the sphere pair with respect to the field direction, and that the leading effect of interactions on this onset is of hydrodynamic origin.

Numerical simulations of the governing equations have also been performed for both fixed spheres and freely suspended spheres. In all of these simulations, we always observed synchronization of the angular velocity magnitudes, though the axes

of rotation of the two spheres are not the same in general. In the case of spheres that are held fixed in space, Quincke rotation of the spheres only occurs above a critical electric field that matches the prediction of the stability analysis, and the time dynamics in the unstable regime are characterized by transient oscillations leading to synchronization at a steady angular velocity. The steady-state angular velocity magnitude and direction depend sensitively upon the configuration of the spheres and initial perturbation to the system, though we find that the statistics of the mean angular velocity magnitude $\langle \Omega^2 \rangle$ are well described by a theoretical estimate derived for co-rotating spheres.

In the case of freely suspended spheres, relative motion of the particles also occurs as a result of the hydrodynamic flow driven by particle rotations and of the dielectrophoretic forces on the particles due to multipolar electric interactions. Numerical experiments have shown that these interactions can lead to complex particle trajectories, which we categorized into four cases: (1) two-dimensional spiraling motion leading to pairing and spinning of the particle pair about the point of contact (only observed in the absence of any initial perturbation), (2) spiraling motion leading to pairing in the field direction with counter-rotation of the spheres and translation as a pair in a direction perpendicular to the field, (3) spiraling motion leading to pairing and alignment in a direction perpendicular to the field with co-rotation of the spheres about their axis of center, and (4) slow separation of the spheres accompanied with spiraling trajectories. The outcome of a particular simulation depends on both the orientation of the spheres and the initial perturbation to the system. Increasing field strength is observed to increase the probability of trajectories leading to pairing, as well as cause more pronounced spiraling motions. It should be kept in mind, however,

that the model solved is accurate for widely separated particles and that near-field interactions may lead to different dynamics in a physical experiment, in particular in cases where pairing occurs. A more accurate treatment of near-contact motions would require a different numerical model, for instance based on the boundary element method.

One important conclusion of this work is the important role of hydrodynamic interactions, which had been neglected in previous studies [168, 40]. In fact, our asymptotic model demonstrated that, perhaps surprisingly, hydrodynamic interactions modify the dipole relaxation equations at the same asymptotic order as electric dipole-dipole interactions. It was also noted that the onset of instability for two interacting spheres is primarily affected by hydrodynamic interactions, and that the spatial dynamics in simulations of freely suspended spheres show a strong influence of rotlet interactions which cause orbiting and spiraling motions.

The present study has cast new light on the effects of electrohydrodynamic interactions on Quincke rotation in the simplest case of two identical spherical particles, and demonstrated a wide variety of dynamical behaviors resulting from the strongly nonlinear nature of the system. The effects of such complex pair interactions in large-scale suspensions of many interacting particles remain, however, difficult to anticipate, and may include structure formation on multiple scales and complex chaotic or correlated motions. We also expect these dynamics and patterns to be modified by an external flow, a situation of interest for the modeling of rheological experiments [98, 95, 112, 96, 125]. Some of these effects will be addressed in future work using numerical simulations by extending efficient algorithms previously developed by Park and Saintillan [115, 116] for nonlinear electrokinetic interactions in colloidal

suspensions.

Acknowledgements

Chapter 2 is based on the Master's Thesis of Debasish Das (2012) submitted in August 2012 at the University of Illinois, Urbana-Champaign [34] and material that has appeared in Physical Review E (2015), authored by Debasish Das and David Saintillan [35]. The dissertation author was the primary researcher and author of this paper. The authors are grateful to Denis Bartolo and Petia Vlahovska for useful conversations on this work.

Chapter 3

Collective motion of Quincke rollers

3.1 Introduction

Nonequilibrium condensed systems composed of self-propelled units or active particles that consume stored or ambient energy to move or exert mechanical forces are called as soft active matter [161, 102]. These self-propelled units interact with each other and the surrounding medium that gives rise to large scale correlated collective motion. A suspension swimming microorganisms is a prototypical example of active matter. Other examples of biological systems include motor proteins and biological filaments like microtubules [143, 80, 38] and actin [146], bacterial suspensions of self-propelled microorganisms such as motile bacteria and microscopic algae [138, 139, 140, 46, 173, 93], cell layers [83, 174]. Nonliving active matter arises in layers of vibrated granular rods or discs [85, 39], colloidal particles that are self-propelled due to catalytic activity at their surface [54, 55, 66, 12], and collections of robots [52]. In

these systems, the energy input that drives the system out of equilibrium is local.

One of the first experimental realizations of self-propelled colloids was the use of asymmetric catalytic reactions to power the motion of nano-micro scale objects [121]. While there have been many attempts since then to device new experiments to produce self propelling particles as a realization of active matter, we will review only a handful here. Palacci *et al.* [111] devised light activated self-propelled colloids that lead to two dimensional living crystals. These spherical particles contain a canted antiferromagnetic hematite cube inside them. The fact that one can switch on and off the self propulsion of these particles using visible light and steer them with magnetic fields gives great control and manoeuvrability in these experiments. In a similar setup but using a different mechanism Buttinoni *et al.* [24] showed that Janus particles suspended in a critical binary liquid mixture perform active Brownian motion when illuminated by light. The illumination-borne heating induces a local asymmetric demixing of the binary mixture, generating a spatial chemical concentration gradient which is responsible for the particle's self-diffusiophoretic motion. While hydrodynamics plays an important role in most of these experiments, there have been dry experiments of self-propelled bristle-bots that are confined to a limited arena with a soft boundary. Increasing the density of these objects drives a transition from a disordered and uncoordinated motion to organized collective motion either as a swirling cluster or a collective dynamical stasis [52].

In many of these colloidal systems, the local alignment rules are difficult to control or measure that makes it difficult to develop an accurate theoretical description. Recent experiments have been able to exploit the phenomena of Quincke electro-rotation to make self-propelled colloidal rollers, henceforth referred to as Quincke

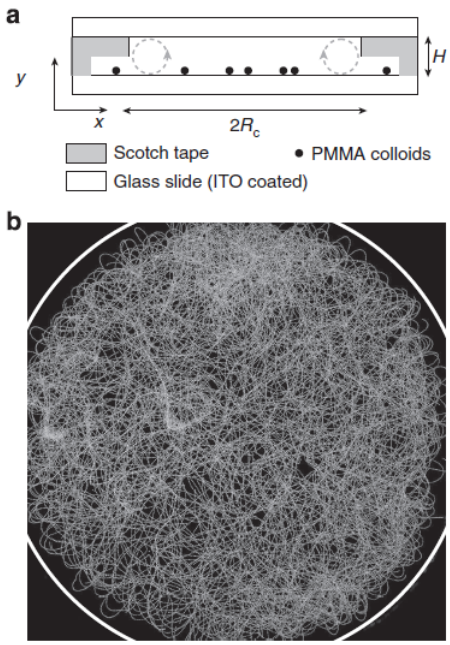

Figure 3.1: Experimental Setup: (a) Sketch of the setup. (b)Superimposed fluorescence pictures of a dilute ensemble of rollers. The colloids propel only inside a circular disc of radius $R_c = 1$mm and follow persistent random walks.

rollers [23]. The mechanism of propulsion is based on well known Maxwell and Stokes equations. The experiments make use of the electrohydrodynamic interactions between many Quincke rollers to understand the emergence of macroscopic motion in active matter. In this work we focus on the effect of confinement on these rollers. The experiments reveal self-organization of motile colloids into a macroscopic steadily rotating vortex that lives on the verge of a phase separation.

3.2 Experimental Setup

The experiments are performed in the Laboratoire de Physique, Ecole Normale Supérieure de Lyon, Université de Lyon. Fluorescent PMMA colloids (Thermo scientific G0500, 2.4 μm radius), dispersed in a 0.15 mol l^{-1} AOT/hexadecane solution are used, see figure 3.1. The suspension is injected in a wide microfluidic chamber made

of double-sided scotch tapes. The tape is sandwiched between two ITO-coated glass slides (Solems, ITOSOL30, 80 nm thick). An additional layer of scotch tape including a hole having the desired confinement geometry is added to the upper ITO-coated slide. The holes are made with a precision plotting cutter (Graphtec robo CE 6,000). The gap between the two ITO electrodes is constant over the entire chamber $H = 220$ mm. The electric field is applied by means of a voltage amplifier (Stanford Research Systems, PS350/5000 V-25 W). All the measurements were performed 5 min after the beginning of the rolling motion, when a steady state was reached for all the observables. The colloids are observed with a $\times 4$ microscope objective for particle tracking, particle imaging velocimetry (PIV) and number-density measurements. High speed movies are recorded with a CMOS camera (Basler ACE) at a frame rate of 190 fps. All images are 2,000 $\times$ 2,000 8-bit pictures. The particles are detected to sub-pixel accuracy and the particle trajectories are reconstructed using a MATLAB version of a conventional tracking code [32]. The PIV analysis was performed with the mpiv MATLAB code. A block size of 44 μm was used. More details on the experimental setup can be found in Bricard *et al.* [23, 22].

3.3 An isolated Quincke roller

We first turn our attention to the dynamics of a single isolated sphere under Quincke rotation on an electrode. The sphere's considered here are perfect insulators so that they have zero conductivity, $\sigma_2 = 0$ and $\sigma_{21} = -1/2$. The dipole moment relaxation equation of a Quincke roller then reads (see chapter 2, section 2.2.1 for

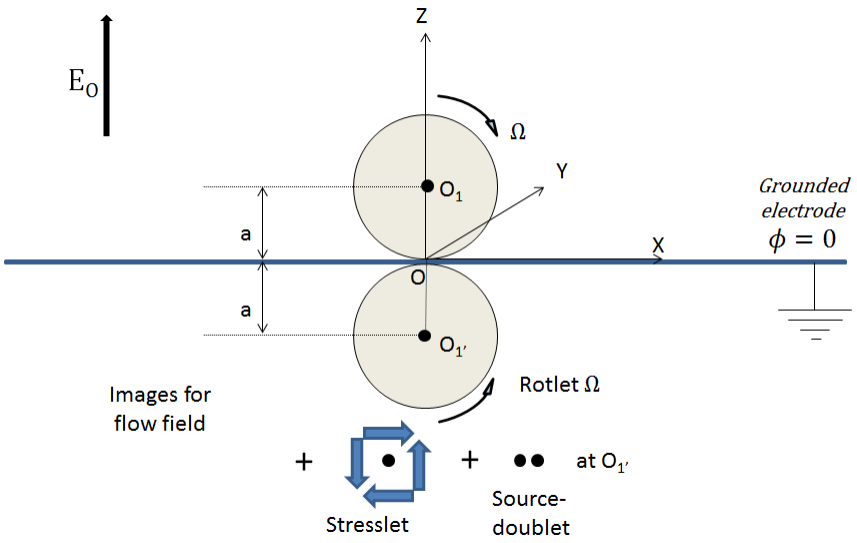

Figure 3.2: Single spherical particle placed on an electrode and its image flow singularities

derivation of a single spherical particle under Quincke rotation),

$$\frac{d\boldsymbol{P}}{dt} + \frac{1}{\tau_{MW}}\boldsymbol{P} = -\frac{1}{\tau_{MW}} 2\pi\epsilon_0 a^3 \boldsymbol{E}_0 + \boldsymbol{\Omega} \times \left(\boldsymbol{P} - 4\pi\epsilon_0 a^3 \epsilon_{21} \boldsymbol{E}_0\right) \tag{3.1}$$

The dipole moment is non-dimensionalised with $4\pi\epsilon_0 a^3 E_0$. The torque acting on the sphere is $\boldsymbol{T}_e = (\epsilon_l/\epsilon_0)\boldsymbol{P} \times \boldsymbol{E}_0$ and the DEP force acting on it is $\boldsymbol{F}_e = (\epsilon_l/\epsilon_0)(\boldsymbol{P}\cdot\nabla)\boldsymbol{E}_0$. In the remainder of the chapter, we only consider the retarding part of the dipole moment i.e. $\boldsymbol{P} = \boldsymbol{P}_\infty + \boldsymbol{P}_r$. The electric field around the sphere is not uniform and is perturbed by the presence of the image dipole, $\boldsymbol{E} = \boldsymbol{E}_0 + \boldsymbol{\delta E}_w$. However, we shall consider it to be small and neglect it in the dipole moment equation. Hence, the role of the electrode is solely to propel the sphere by coupling its angular velocity to its translational velocity. The dipole moment relaxation equation for the retarding part is,

$$\frac{d\boldsymbol{P}_r}{dt} + \frac{1}{\tau_{MW}}\boldsymbol{P}_r = -\frac{1}{\tau_{MW}} 4\pi\epsilon_0 a^3 E_0 \left(\epsilon_{21} + \frac{1}{2}\right)\hat{\boldsymbol{z}} + \boldsymbol{\Omega} \times \boldsymbol{P}_r. \tag{3.2}$$

The electric torque acting on the roller is,

$$\boldsymbol{T}_e^{||} = \frac{\epsilon_l}{\epsilon_0} E_0 \left(\boldsymbol{P} \times \hat{\boldsymbol{z}}\right). \tag{3.3}$$

It is clear from the above equation that $T_e^z = 0$ and therefore, $\Omega^z = 0$, implying a Quincke roller does not rotate in the direction of the applied field. The angular and translational velocity are then given as,

$$\boldsymbol{\Omega}^{||} = \mu_r \boldsymbol{T}_e^{||} = \mu_r \frac{\epsilon_l}{\epsilon_0} E_0 \left(\boldsymbol{P}_r \times \hat{\boldsymbol{z}}\right), \tag{3.4a}$$

$$\frac{\boldsymbol{v}_0}{a} = \frac{\widetilde{\mu}_t}{\mu_r} \boldsymbol{\Omega}^{||} \times \hat{\boldsymbol{z}}. \tag{3.4b}$$

The coefficients $\mu_r, \tilde{\mu}_t$ are found by asymptotic lubrication theory [53]. Substituting the angular velocity in the retarding dipole moment equation, we get,

$$\frac{d\boldsymbol{P}_r}{dt} + \frac{1}{\tau_{MW}} \boldsymbol{P}_r = -\frac{1}{\tau_{MW}} 4\pi\epsilon_0 a^3 E_0 \left(\epsilon_{21} + \frac{1}{2}\right) \hat{\boldsymbol{z}} + \mu_r \frac{\epsilon_l}{\epsilon_0} E_0 \left(\boldsymbol{P}_r \times \hat{\boldsymbol{z}}\right) \times \boldsymbol{P}_r. \tag{3.5}$$

The dipole moment equation in z-direction and x-y plane are:

$$\frac{dP_r^z}{dt} + \frac{1}{\tau_{MW}} P_r^z = -\frac{1}{\tau_{MW}} 4\pi\epsilon_0 a^3 E_0 \left(\epsilon_{21} + \frac{1}{2}\right) + \frac{\epsilon_l}{\epsilon_0} \mu_r E_0 \left[\left(\boldsymbol{P}_r \cdot \boldsymbol{P}_r\right) - \left(P_r^z\right)^2\right], \tag{3.6a}$$

$$\frac{d\boldsymbol{P}_r^{||}}{dt} + \frac{1}{\tau_{MW}} \boldsymbol{P}_r^{||} = -\frac{\epsilon_l}{\epsilon_0} \mu_r E_0 P_r^z \boldsymbol{P}_r^{||}. \tag{3.6b}$$

Denoting the in-plane dipole moment as $\boldsymbol{P}_r^{||} = P_r^{||} \hat{\boldsymbol{p}}$, where $\hat{\boldsymbol{p}}$ is a unit vector in the direction of $\boldsymbol{P}^{||}$, we obtain an evolution equation for the roller's orientation,

$$\hat{\boldsymbol{p}} \frac{dP_r^{||}}{dt} + P_r^{||} \frac{d\hat{\boldsymbol{p}}}{dt} + \frac{1}{\tau_{MW}} P_r^{||} \hat{\boldsymbol{p}} = -\frac{\epsilon_l}{\epsilon_0} \mu_r E_0 P_r^z P_r^{||} \hat{\boldsymbol{p}}. \tag{3.7}$$

Denoting $\hat{\boldsymbol{p}} = (\cos\theta, \sin\theta)$, the above vector equation yields two scalar equations,

$$\frac{dP_r^{||}}{dt} + \frac{1}{\tau_{MW}} P_r^{||} = -\frac{\epsilon_l}{\epsilon_0} \mu_r E_0 P_r^z P_r^{||}, \tag{3.8a}$$

$$\frac{d\theta}{dt} = 0 \tag{3.8b}$$

We can find that a steady state solution for the above equation,

$$P_r^z = -\frac{\epsilon_0}{\epsilon_l \tau_{MW} \mu_r E_0}. \tag{3.9}$$

Substituting this expression in equation (3.8a), and using the expression for critical velocity $E_c = \left[4\pi\epsilon_l a^3 \left(\epsilon_{21} + \frac{1}{2}\right) \mu_r \tau_{MW}\right]^{-\frac{1}{2}}$, we can find the steady state translational velocity of the roller,

$$P_r^{||} = \frac{\epsilon_0}{\epsilon_l} \frac{1}{\tau_{MW} \mu_r E_0} \sqrt{\left(\frac{E_0}{E_c}\right)^2 - 1}, \tag{3.10a}$$

$$\frac{\boldsymbol{v}_0}{a} = \widetilde{\mu}_t \boldsymbol{T}_e^{||} \times \hat{\boldsymbol{z}} = -\widetilde{\mu}_t \frac{\epsilon_l}{\epsilon_0} E_0 \boldsymbol{P}_r^{||}. \tag{3.10b}$$

The translational velocity of the sphere is in the opposite direction as that of the in-plane dipole moment and its magnitude is,

$$v_0 = \frac{a\widetilde{\mu}_t}{\tau_{MW} \mu_r} \sqrt{\left(\frac{E_0}{E_c}\right)^2 - 1}. \tag{3.11}$$

The main result of this section is that a single Quincke roller propels at a velocity of v_0 without changing its orientation. In the next section, we will see how a roller undergoes slow orientational dynamics due to the effect of electrohydrodynamic interactions with other rollers.

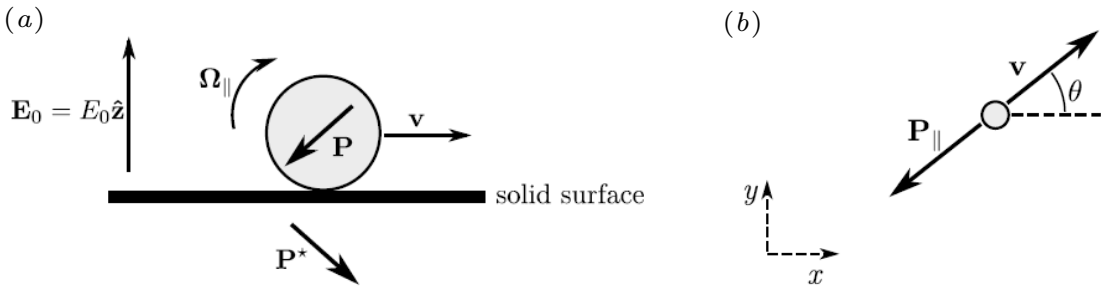

Figure 3.3: An isolated Quincke roller: (a) Coupling between rotational and translational velocity of the Quincke roller (b) In the plane of the surface, the direction of the translation velocity is defined by the angle θ. Reproduced from [23]

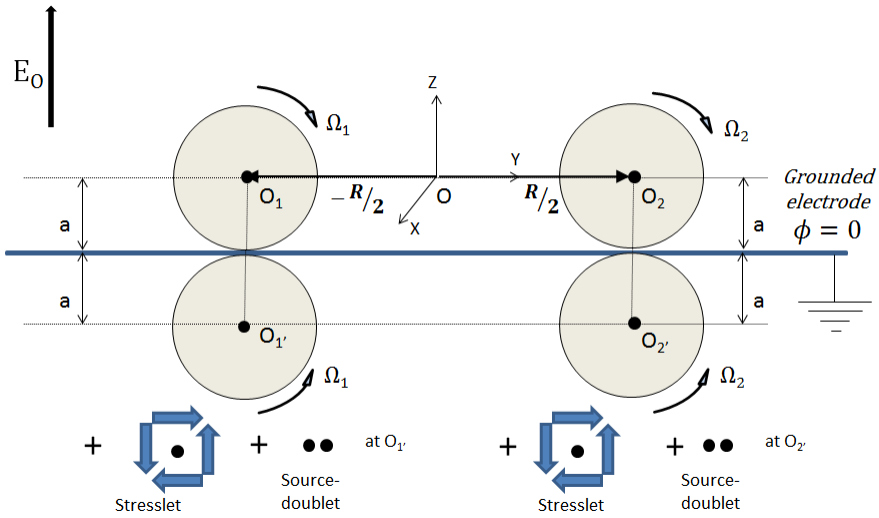

Figure 3.4: Electrohydrodynamic interactions between two Quincke rollers and their image flow singularities.

3.4 Electrohydrodynamic interactions of Quincke rollers

In this section, we analyze the electrohydrodynamic interaction between two spheres rolling on the electrode. The electric field perturbed around sphere 1 due to the sphere 2 is denoted as $\boldsymbol{\delta E}$.

The retarding dipole moment equation is,

$$\frac{d\boldsymbol{P}_r}{dt} + \frac{1}{\tau_{MW}}\boldsymbol{P}_r = -\frac{1}{\tau_{MW}} 4\pi\epsilon_0 a^3 \left(\epsilon_{21} + \frac{1}{2}\right)(E_0\hat{\boldsymbol{z}} + \delta\boldsymbol{E}) + \boldsymbol{\Omega} \times \boldsymbol{P}_r. \tag{3.12}$$

The mobility matrix of the Quincke roller is,

$$\begin{pmatrix} \frac{v_0}{a} \\ \boldsymbol{\Omega}^{||} \\ \Omega_z \end{pmatrix} = \begin{pmatrix} \mu_t \boldsymbol{I} & \widetilde{\mu}_t \boldsymbol{\Lambda} & 0 \\ -\widetilde{\mu}_r \boldsymbol{\Lambda} & \mu_r \boldsymbol{I} & 0 \\ 0 & 0 & \mu_\perp \end{pmatrix} \cdot \begin{pmatrix} a\boldsymbol{F}_e^{||} \\ \boldsymbol{T}_e^{||} \\ T_e^z \end{pmatrix} + \begin{pmatrix} \mu_s \partial_z \boldsymbol{v}_0^{||}|_{z=0} \\ \widetilde{\mu}_s \hat{\boldsymbol{z}} \times \partial_z \boldsymbol{v}_0^{||}|_{z=0} \\ 0 \end{pmatrix}. \tag{3.13}$$

The hydrodynamic effect of a Quincke roller next to a wall is captured by placing a rotlet next to a wall with no-slip boundary conditions. This flow field was computed by Blake and Chwang [17] using image singularity method and takes into account hydrodynamic interactions. In the experiments it is observed that the translational speed of the rollers does not alter greatly due to interactions. This observation leads us to simplify the model further and assume that a particle i moves at a constant velocity v_0 on the surface and undergoes a slow orientational dynamics due to electrohydrodynamic interactions. The expressions for electric force, torque and velocity field experienced by a single roller due to interactions are given in [23] and omitted here for brevity. These interactions can be conveniently expressed as an effective potential that governs the dynamics of these rollers. The simplified equations

of motions are:

$$\dot{\boldsymbol{r}}_i = v_0 \hat{\boldsymbol{p}}_i \tag{3.14}$$

$$\dot{\theta} = \frac{1}{\tau} \frac{\partial}{\partial \theta_i} \sum_{j \neq i} \mathcal{H}_{\text{eff}}(\boldsymbol{r}_i - \boldsymbol{r}_j, \hat{\boldsymbol{p}}_i, \hat{\boldsymbol{p}}_j) + \xi_i, \tag{3.15}$$

$$\text{where,} \quad \mathcal{H}_{\text{eff}} = A(r)\hat{\boldsymbol{p}}_i \cdot \hat{\boldsymbol{p}}_j + B(r)\hat{\boldsymbol{r}} \cdot \hat{\boldsymbol{p}}_i + C(r)\hat{\boldsymbol{p}}_j \cdot (2\hat{\boldsymbol{r}}\hat{\boldsymbol{r}} - \boldsymbol{I}) \cdot \hat{\boldsymbol{p}}_i \tag{3.16}$$

In the orientation flux equation (3.15) $\mathcal{H}_{\text{eff}}$ is the global interaction potential and ξ accounts for the rotational diffusion of the particles. They are uncorrelated white noise variables with zero mean and variance $\langle \xi_i(t)\xi_j(t') \rangle = 2D\delta(t - t')\delta_{ij}$. the various interactions terms contained in the interaction potential are:

$$A(r) = 3\tilde{\mu}_s \frac{a^3}{r^3} + 9\left(\frac{\mu_\perp}{\mu_r} - 1\right)\left(\epsilon_{21} + \frac{1}{2}\right)\left(1 - \frac{E_c^2}{E_0^2}\right)\frac{a^5}{r^5}, \tag{3.17a}$$

$$B(r) = 6\left(\frac{\mu_\perp}{\mu_r} - 1\right)\sqrt{\frac{E_0}{E_c^2} - 1}\left[\left(\epsilon_{21} + \frac{1}{2}\right)\frac{E_c^2}{E_0^2} - \epsilon_{21}\right]\frac{a^4}{r^4}, \tag{3.17b}$$

$$C(r) = 3\tilde{\mu}_s \frac{a^3}{r^3} + 15\left(\frac{\mu_\perp}{\mu_r} - 1\right)\left(\epsilon_{21} + \frac{1}{2}\right)\left(1 - \frac{E_c^2}{E_0^2}\right)\frac{a^5}{r^5}. \tag{3.17c}$$

The exact derivation of these terms can be found in the supplmentary material of [23] and omitted here for brevity. The first term $A(r)$ stems from hydrodynamic interactions and promotes alignment between particles. The second term $B(r)$ arises from electrostatic interactions and gives rise to repulsive torques causing the particles to point away from each other. The last term $C(r)$ arises from both hydrodynamic and electrostatic interactions and can cause both alignment or repulsion based on the separation vector $\boldsymbol{r}$ and has a less intuitive meaning. Particle positions and rolling directions are initialized randomly inside a circular domain. Integration is done using an Euler scheme with an adaptive time step. A torque is applied near the circular

boundary to capture the bouncing off of particles as seen in experiments. The particles that do reach the circular boundary are reflected back into the domain. With the diffusion coefficient of the particles fixed, there is only free parameter b which is the range of repulsive forces between particles due to steric interactions.

The simulations are performed by numerically integrating the equations of motion, (3.14) and (3.15). Particle positions and rolling directions are initialized randomly inside a circular domain. Integration is done using an Euler scheme with an adaptive time step dt, and the diffusive term in the equation for the rotational dynamics is modelled as a Gaussian variable with zero mean and with variance $2D/dt$. Steric exclusion between particles is captured by correcting particle positions after each time step so as to prevent overlaps. Bouncing off of particles at the confining boundary is captured using a phenomenological torque that reorients the particles towards the centre of the disc; the form of the torque was chosen so at the reproduce the bouncing trajectories observed in the experiments.

3.5 Results

As a test of our simulation method, we numerically integrate these equations of motion in a ring and square confinement for qualitative comparison with the experiments of Bricard *et al.* [23], see Fig. 3.5. The particle density in these simulations are set at $\phi_0 = 0.1$. In the case of ring, we find the formation of bands that eventually merge to form a single band and propagate along the ring in qualitative agreement with experiments of Bricard *et al.* [23] in racetrack confinement. On confining these particles in a square box geometry, we find correlated motion on the length scale of the box in the transient state while in the steady state there is a steady vortex of

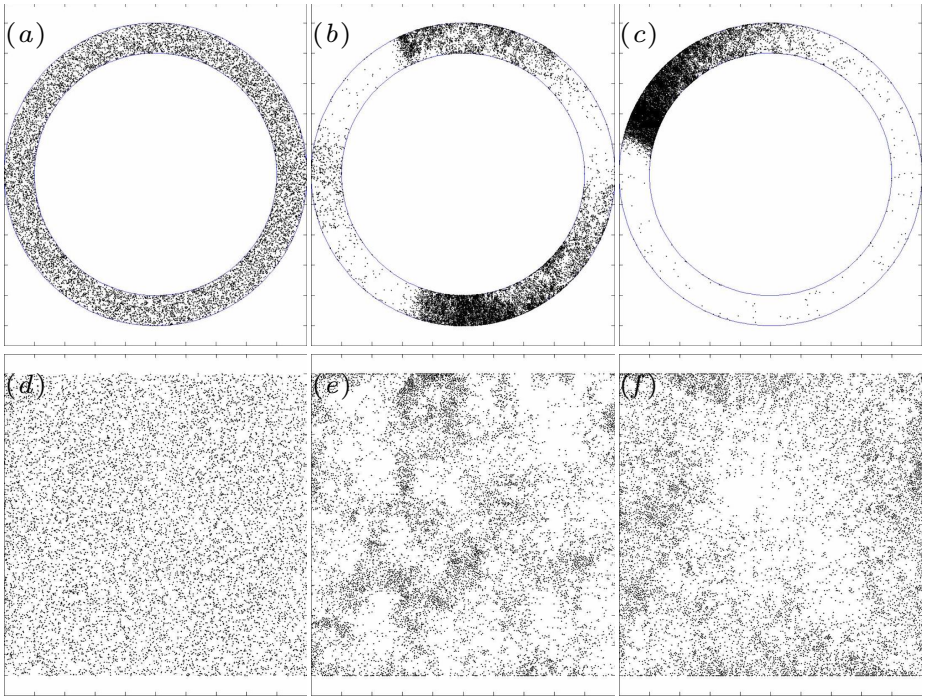

Figure 3.5: Collective dynamics of Quincke rollers confined in a ring and square confinement ($\phi_0 = 0.1$): (a) Initial particle positions in ring confinement, (b) transient particle positions arranged in two bands, (c) steady state particle positions with on band propagating along the ring, (d) Initial particle positions in a square confinement, (e) transient state in which particles show density fluctuations, (f) steady vortex rotating in a counterclockwise direction.

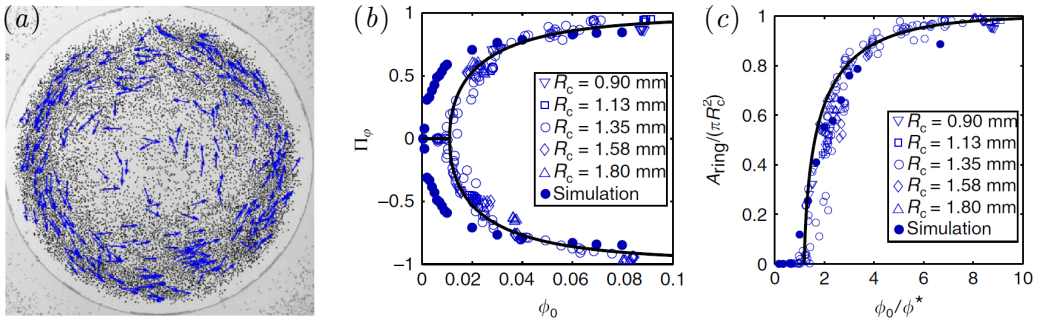

Figure 3.6: Collective dynamics experiments: (a) Snapshot of a vortex of rollers. The dark dots show the position of one half of the ensemble of rollers. The blue vectors represent their instantaneous speed ($R_c = 1.35$mm, $\phi_0 = 5 \times 10^{-2}$) (b) Average polarization plotted versus the average packing fraction for different confinement radii. Open symbols: experiments. Full line: best fit from the theory. Filled circles: numerical simulations ($b = 3a$, $R_c = 1$mm), (c) Fraction of the disc where $\Pi_\varphi > 0.5$ versus the average packing fraction. Open symbols: experiments. Full line: theoretical prediction with no free fitting parameter. Filled circles: numerical simulations ($b = 3a$, $R_c = 1$mm).

particles rotating around the box center.

In order to quantify the effect of confinement on Quincke rollers, we perform a thorough comparison of theory, experiments and simulations in a circular geometry. As the area fraction is increased above ϕ^* in this circular confinement, collective motion emerges spontaneously at the entire population level. When the electric field is applied, large groups of rollers akin to the band-shaped swarms reported in [23] form and collide. However, unlike what was observed in periodic geometries, the colloidal swarms are merely transient and ultimately self-organize into a single vortex pattern spanning the entire confining disc as shown in Fig. 3.6(a). Once formed, the vortex is very robust, rotates steadily and retains an axisymmetric shape. To go beyond this qualitative picture, we measured the local colloid velocity field $\boldsymbol{v}(r,t)$ and use it to define the polarization field $\Pi(r,t) = \boldsymbol{v}/v_0$ which quantifies local orientational ordering. The spatial average of $\Pi(r,t)$ vanishes when a coherent vortex forms, therefore we use

its projection $\Pi(r,t)_\varphi = \langle \Pi \cdot \hat{\boldsymbol{e}}_\varphi \rangle$ along the azimuthal direction as a macroscopic order parameter to probe the transition from an isotropic gas to a polar-vortex state. As illustrated in Fig. 3.6(b), $\Pi(r,t)_\varphi(\phi_0)$ displays a sharp bifurcation from an isotropic state with $\Pi(r,t)_\varphi = 0$ to a globally ordered state with equal probability for left- and right-handed vortices above $\phi = \phi^*$ Furthermore, Fig. 3.6(b) demonstrates that this bifurcation curve does not depend on the confinement radius R_c. Open symbols denotes experiments, full line denote theoretical prediction with no free fitting parameter and filled circles denote numerical simulations ($b = 3a$, $R_c = 1$ mm). We define A_{ring} as the area of the region where the order parameter exceeds 0.5, and none of the results reported below depend on this arbitrary choice for the definition of the outer-ring region. A_{ring} also bifurcates as ϕ_0 exceeds ϕ^*, and increases with R_c. Remarkably, all the bifurcation curves collapse on a single master curve when A_{ring} is rescaled by the overall confinement area πR_c^2 , Fig. 3.6(c).

Simulations of Quincke rollers revealed a richer phenomenology than the experiments, as captured by the phase diagram in Fig. 3.7(a). By systematically varying the range of the repulsive forces and the particle concentration, we found that the (ϕ_0, b) plane is typically divided into three regions, swarm coexisting with a gaseous phase, and vortex state. At small packing fractions, the particles hardly interact and form an isotropic gaseous phase. At high fractions, after a transient dynamics strikingly similar to that observed in the experiments, the rollers self-organize into a macroscopic vortex pattern, Fig. 3.7(b). However, at intermediate densities, we found that collective motion emerges in the form of a macroscopic swarm cruising around the circular box through an ensemble of randomly moving particles, Fig. 3.7(c). These swarms are akin to the band patterns consistently reported for polar active

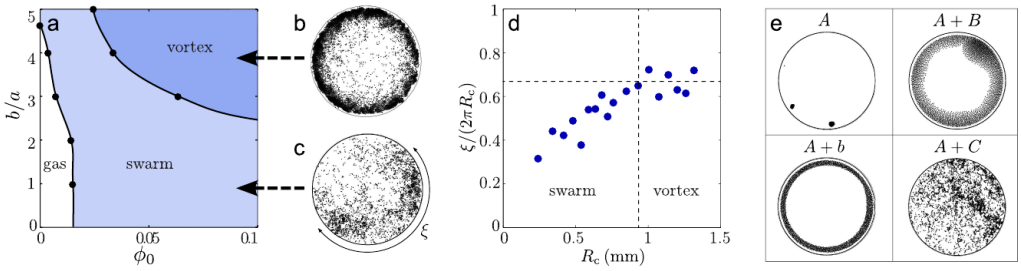

Figure 3.7: Collective dynamics simulations: (a) The numerical phase diagram of the confined population is composed of three regions: isotropic gas (low ϕ_0, small b), swarm coexisting with a gaseous phase (intermediate ϕ_0 and b) and vortex state (high ϕ_0 and b). $R_c = 0.5$mm, (b) Snapshot of a vortex state, (c) Snapshot of a vortex state. Numerical simulation for $\phi_0 = 0.1$ and $b = 5a$, (d) Variation of the density correlation length as a function of R_c. Above $R_c = 1$mm, ξ plateaus and a vortex is reached ($\phi_0 = 3 \times 10^{-2}$, $b = 3a$), (e) Four numerical snapshots of rollers interacting via: alignment interactions only (A), alignment interactions and repulsive torques ($A + B$, where the magnitude of B is five times the experimental value), alignment and excluded volume interactions ($A + b$, where the repulsion distance is $b = 5a$), alignment and the C-term in equation 3 ($A + C$). Polarized vortices emerge solely when repulsive couplings exist ($A + B$ and $A + b$).

particles at the onset of collective motion in periodic domains [56, 23]. This seeming conflict between our experimental and numerical findings is solved by looking at the variations of the swarm length ξ_s with the confinement radius R_c in Fig. 3.7(d). We define ξ_s as the correlation length of the density fluctuations in the azimuthal direction. The angular extension of the swarms ξ_s/R_c increases linearly with the box radius. Therefore, for a given value of the interaction parameters, there exists a critical box size above which the population undergoes a direct transition from a gaseous to an axisymmetric vortex state. For $b = 3a$, which was measured to be the typical interparticle distance in the polar liquid state [23], this critical confinement is $R_c = 1$ mm. This value is close to the smallest radius accessible in our experiments where localized swarms were never observed, thereby solving the apparent discrepancy with the experimental phenomenology.

More quantitatively, we systematically compare our numerical and experimental measurements in Fig. 3.6(b, c) for $R_c = 1$ mm. Even though a number of simplifications were needed to establish equations (3.14) and (3.15), the simulations account very well for the sharp bifurcation yielding the vortex patterns as well as their self-similar structure. This last point is proven quantitatively in Fig. 3.6(c), which demonstrates that the concentration increases away from the vortex core, where $\phi(r = 0) = \phi^*$ over a scale that is solely set by the confinement radius (Above $R_c = 1$ mm, ξ plateaus and a vortex is reached ($\phi_0 = 3\times\ 10^{-2}$, $b = 3a$). We shall note however that the numerical simulations underestimate the critical packing fraction ϕ^* at which collective motion occurs, which is not really surprising given the number of approximations required to establish the interaction parameters in the equations of motion, (3.14) and (3.15). We unambiguously conclude from this set of results that equations (3.14) and (3.15) include all the physical ingredients that chiefly dictate the collective dynamics of the colloidal rollers.

We now exploit the opportunity offered by the numerics to turn on and off the four roller-roller interactions one at a time, namely the alignment torque, A, the repulsion torque B and force b, and the dipolar coupling C. Snapshots of the resulting particle distributions are reported in Fig. 3.7(e). None of these four interactions alone yields a coherent macroscopic vortex. We stress that when the particles solely interact via pairwise-additive alignment torques, $B = C = b = 0$, the population condenses into a single compact polarized swarm. Potential velocity-alignment interactions are not sufficient to yield macroscopic vortical motion. We evidence in Fig. Fig. 3.7(e) (top-right and bottom-left panels) that the combination of alignment ($A \neq 0$) and of repulsive interactions ($B \neq 0$ and $b \neq 0$) is necessary and sufficient to observe

spontaneously flowing vortices. The different interaction terms in Fig. 3.7(e) are : alignment interactions only (A), alignment interactions and repulsive torques (A + B, where the magnitude of B is 5 times the experimental value), alignment and excluded volume interactions (A + b, where the repulsion distance is $b = 5a$), alignment and the C-term in Eq. (3.16) (A + C). Polarized vortices emerge solely when repulsive couplings exist (A + B and A + b). The details of the coarse grain theory have not been discussed in this thesis and can be found in [22].

3.6 Conclusion

In this work, we took advantage of the Quincke electrotation phenomena in which a particle can undergo sustained spontaneous rotation in an infinite fluid medium. The mechanism of spontaneous rotation was intertwined with spontaneous translation by hydrodynamic coupling with a wall (in this case an electrode). Using this simple idea, we devised a model experimental system where ensembles of self-propelled colloids with well-established interactions self-organize into macrosopic vortices when confined by circular geometric boundaries. We identify the physical mechanism that chiefly dictates this emergent behaviour. Thanks to a combination of numerical simulations and analytical theory, we demonstrate that orientational couplings alone cannot account for collective circular motion. Repulsion between the motile individuals is necessary to balance the centrifugal flow intrinsic to any ordered active fluid and to stabilize heterogeneous yet monophasic states in a broad class of active fluids. A natural challenge is to extend this description to the compact vortices observed in the wild, for example, in shoals of fish. In the absence of confining boundaries, the centrifugal force has to be balanced by additional density-regulation mechanisms

[31, 122]. A structural investigation akin to the one introduced here for roller vortices could be a powerful tool to shed light on density regulation in natural flocks, which remains to be elucidated. One of the present challenges in the active matter research is to develop a robust system of self-propelled particles in three-dimensions. Due to the ease of manipulation and control offered by electric (or magnetic) fields, electro (or magneto) hydrodynamic systems hold tremendous potential in devising these kind of desired self-propelled colloids.

Contributions

A.B. and V.C. carried out the experiments and processed the data. D.D., C.S., O.C., F.P. and D.S. carried out the the numerical simulations. J.-B.C., K.S. and D.B. established the analytical model. All the authors discussed and interpreted results. D.B., J.-B.C. and D.S. wrote the manuscript. D.B. conceived the project. A.B. and J.-B.C. have equally contributed to this work.

Acknowledgments

Chapter 3 is based on material that has appeared in Nature Communications (2015), authored by Antoine Bricard, Jean-Baptiste Caussin, Debasish Das, Charles Savoie, Vijaykumar Chikkadi, Kyohei Shitara, Oleksandr Chepizhko, Fernando Peruani, David Saintillan and Denis Bartolo [22]. The dissertation author was the third author of this paper. We benefited from valuable discussions with Hugues Chaté, Nicolas Desreumaux, Olivier Dauchot, Cristina Marchetti, Julien Tailleur and John Toner. This work was partly funded by the ANR program MiTra, and Institut Universitaire de France. D.S. acknowledges partial support from the Donors of the American Chemical

Society Petroleum Research Fund and from NSF CAREER Grant No. CBET-1151590. K.S. was supported by the JSPS Core-to-Core Program 'Non-equilibrium dynamics of soft matter and information'.

Chapter 4

Electrohydrodynamics of axisymmetric drops

4.1 Introduction

Electric fields, when applied to weakly conducting dielectric liquids, can give rise to fluid motions, the study of which forms the field of electrohydrodynamics [103, 145]. In contrast with aqueous electrolytes, ion dissociation in the presence of electric fields is typically negligible in dielectric liquids, so that diffuse Debye layers are absent and fluid motions instead result from the coupling of electric and hydrodynamic stresses acting on interfaces. Electrohydrodynamic phenomena find widespread industrial applications, such as: inkjet printing [8, 118], electrospraying and atomization of liquids [158, 160, 25], solvent extraction [148], electrohydrodynamic pumps [92], and fiber electrospinning [71], among others.

We focus here on the simple problem of electrohydrodynamic deformations of an uncharged leaky dielectric drop suspended in an infinite weakly conducting fluid

medium and subject to a steady uniform electric field. This problem, first studied by Wilson & Taylor [172], was originally analyzed under the premise that normal electric stresses acting on an uncharged interface are responsible for deformations [108, 62]. Normal stresses, however, can only result in prolate deformations, while experiments have been known to show both prolate and oblate shapes depending on material properties [4]. This paradox was resolved in the pioneering work of Taylor [159], who recognized that dielectric liquids, while poor conductors, still carry some free charges, which upon application of the field accumulate at the liquid-liquid interface in the form of a surface charge distribution due to the mismatch in electrical properties. Taylor realized that the existence of this surface charge can then give rise to tangential stresses that drive circulatory toroidal currents inside the drop, now known as Taylor vortices. Taylor's theory was able to predict both oblate and prolate shapes and showed good agreement with experiments in weak fields.

Having discovered the importance of surface charge and its contribution to tangential stresses on the interface, Melcher & Taylor [103] developed a complete framework for studying the electrohydrodynamics of leaky dielectric drops. The central result of their model is a surface charge conservation equation that prescribes a balance between transient charge relaxation, the jump in normal Ohmic currents arising from the weak but finite conductivities of the two media, and charge convection on the drop surface by the interfacial fluid velocity. The original model of [159], however, neglected transient effects and charge convection and only accounted for first-order deformations in the limit of vanishing electric capillary number Ca_E, which compares the magnitude of electric stresses to surface tension. As a result, agreement with experiments was limited to very small deformations, and a number of more detailed

theories have been proposed over the years to improve upon this. First, Ajayi [2] extended Taylor's theory by retaining terms to second order in capillary number, but also neglected transients and charge convection. His results, quite surprisingly, showed worse agreement with experiments than the simpler model of Taylor in the case of oblate drops, which is a consequence of the latter approximation.

Including charge convection, however, is quite challenging as it couples the charge distribution to the resulting fluid flow in a nonlinear fashion. A few computational studies considered its effects [49, 156, 100, 90] and showed that convection tends to increase deformation in the case of prolate drops but decrease it for oblate drops. The complete Melcher-Taylor model was also used in finite-element simulations to study the closely related phenomenon of electrohydrodynamic tip streaming and disintegration of electrified drops [28, 29]. On the theoretical side, Shutov [154] and Shkadov & Shutov [153] attempted to include charge convection in a small-deformation theory; however, these authors neglected it at first order and only included it at second order, which as we will show below is incorrect. Very recently, Bandopadhyay *et al.* [6] studied the dynamics of a drop sedimenting under gravity while subject to an electric field using double asymptotic expansions in electric capillary number Ca_E and electric Reynolds number Re_E, which compares electric to viscous stresses. Their theory included linearized charge convection and was limited to small Re_E.

Transient dynamics were also addressed in a few models by including temporal derivatives of shape modes, first by Moriya *et al.* [105] for perfectly conducting drops, followed by Esmaeeli & Sharifi [48] for weakly conducting drops. The latter theory predicted a monotonic drop deformation leading to the steady drop shape predicted by Taylor [159]. Yet, both experiments [90] and numerical simulations [63, 156] show

non-monotonic deformations in cases leading to steady oblate shapes, suggesting an inconsistency in the model. This discrepancy was recently resolved by Lanauze *et al.* [89], who showed using a small-deformation theory that either transient charge relaxation or fluid acceleration, combined with transient shape deformations, needs to be included in the model to capture the correct behavior.

In this work, we present an extension to previous small-deformation theories valid to order $O(Ca_E^2)$ that captures unsteady dynamics. The novelty of our model lies in the theoretical formulation for the complete Melcher-Taylor leaky dielectric model, in which we include transient shape deformation, transient charge relaxation and nonlinear charge convection. As we demonstrate by comparison with boundary element simulations and existing experiments, including both transient phenomena is critical in order to capture the correct shape evolution, and accounting for charge convection leads to improved accuracy in the model predictions as the electric field strength increases. We present the governing equations in §4.2. Details of the asymptotic theory are provided in §4.3 and summarized in §4.4, and results of the theory are discussed in §5.4, where we compare them to experiments as well as boundary element simulations based on an algorithm outlined in appendix B.3. We conclude and discuss potential extensions of this work in §4.6.

4.2 Problem formulation

We analyze the deformation of a neutrally buoyant liquid drop suspended in another liquid and subject to a uniform electric field $\boldsymbol{E}_0 = E_0\hat{\boldsymbol{e}}_z$ as shown in figure 4.1. Streamlines show the direction of the flow at steady state in the case of an oblately deformed drop. The drop, with undeformed radius a, is assumed to carry no net

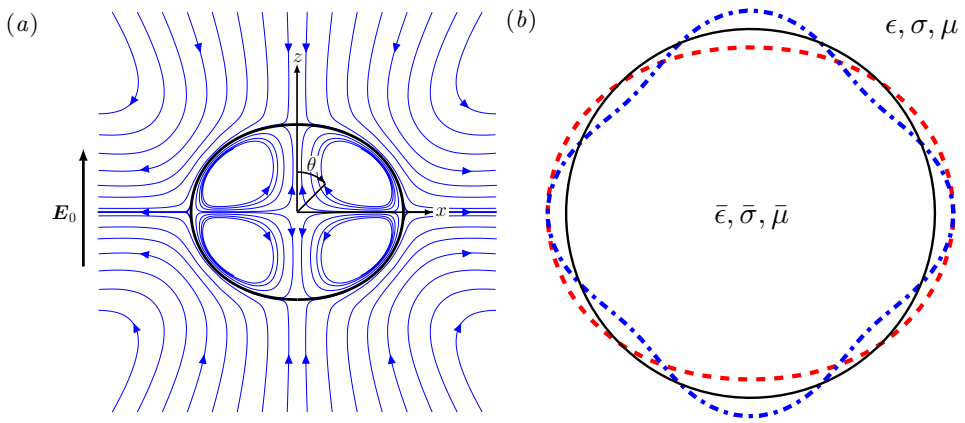

Figure 4.1: Problem definition: a liquid drop is placed in a uniform electric field $\boldsymbol{E}_0$. (a) Spherical coordinates (r, θ) used in axisymmetric geometry. Streamlines show the direction of the flow at steady state in the case of an oblately deformed drop. (b) Drop shape expanded on the basis of spherical harmonics. The full line corresponds to the spherical shape, while the dashed line and dash-dotted line correspond to second-order $\mathcal{L}_2$ and fourth-order $\mathcal{L}_4$ deformation modes, respectively.

charge. Both liquids are Newtonian and are treated as leaky dielectrics with constant material properties. The dielectric permittivity, electric conductivity, and dynamic viscosity of the carrying liquid are denoted by $(\epsilon,\ \sigma,\ \mu)$, respectively, whereas those of the drop are denoted by $(\bar{\epsilon},\ \bar{\sigma},\ \bar{\mu})$. The interface S between the two liquids has uniform surface tension γ and outward unit normal $\boldsymbol{n}$.

Following the Melcher-Taylor leaky dielectric model [103], we assume that any net charge in the system is concentrated at the interface between the two liquids. Under this condition, the electric potentials φ and $\bar{\varphi}$ outside and inside the drop both satisfy Laplace's equation:

$$\nabla^2 \varphi = 0, \qquad \nabla^2 \bar{\varphi} = 0. \tag{4.1}$$

The potential is continuous across the interface:

$$\varphi(\boldsymbol{x}) = \bar{\varphi}(\boldsymbol{x}) \qquad \text{for} \quad \boldsymbol{x} \in S, \tag{4.2}$$

and approaches the externally applied potential far away from the drop:

$$\varphi(\boldsymbol{x}) \to \varphi_e(\boldsymbol{x}) = -\boldsymbol{E}_0 \cdot \boldsymbol{x} \quad \text{as} \quad |\boldsymbol{x}| \to \infty. \tag{4.3}$$

Due to the mismatch in material properties, a surface charge density $q(\boldsymbol{x})$ develops at the interface between the two liquids as the drop polarizes and is given by Gauss's law:

$$q(\boldsymbol{x}) = \boldsymbol{n} \cdot [\![\epsilon \boldsymbol{E}(\boldsymbol{x})]\!] = \epsilon E^n(\boldsymbol{x}) - \bar{\epsilon}\bar{E}^n(\boldsymbol{x}), \tag{4.4}$$

where $\boldsymbol{E} = -\boldsymbol{\nabla}\varphi$ is the local electric field and $E^n = \boldsymbol{n} \cdot \boldsymbol{E}$ its normal component. The charge density q evolves due to two distinct mechanisms: Ohmic currents $\boldsymbol{j} = \sigma \boldsymbol{E}$ from the bulk, and surface charge convection by the fluid flow with velocity $\boldsymbol{v}$ along the interface. Accordingly, it satisfies the conservation equation

$$\partial_t q + \boldsymbol{n} \cdot [\![\boldsymbol{j}]\!] + \boldsymbol{\nabla}_s \cdot (q\boldsymbol{v}) = 0, \tag{4.5}$$

where $\boldsymbol{\nabla}_s \equiv (\boldsymbol{I} - \boldsymbol{nn}) \cdot \boldsymbol{\nabla}$ is the surface gradient operator. The flow velocity, which is driven by electric stresses on the interface, satisfies the Stokes equations in both liquids:

$$-\mu\nabla^2\boldsymbol{v} + \boldsymbol{\nabla}p^H = \boldsymbol{0}, \quad \boldsymbol{\nabla} \cdot \boldsymbol{v} = 0, \tag{4.6a}$$

$$-\bar{\mu}\nabla^2\bar{\boldsymbol{v}} + \boldsymbol{\nabla}\bar{p}^H = \boldsymbol{0}, \quad \boldsymbol{\nabla} \cdot \bar{\boldsymbol{v}} = 0, \tag{4.6b}$$

and is continuous across the interface. Here, p^H denotes the hydrodynamic pressure in the fluid. In the absence of Marangoni effects, the jumps in electric and hydrodynamic tractions balance interfacial tension forces:

$$[\![\boldsymbol{f}^E]\!] + [\![\boldsymbol{f}^H]\!] = \gamma(\boldsymbol{\nabla}_s \cdot \boldsymbol{n})\boldsymbol{n} \quad \text{for } \boldsymbol{x} \in S, \tag{4.7}$$

where $\boldsymbol{\nabla}_s \cdot \boldsymbol{n}$ is the total surface curvature. The jumps in tractions are expressed in terms of the Maxwell stress tensor $\boldsymbol{T}^E$ and hydrodynamic stress tensor $\boldsymbol{T}^H$ as

$$[\![\boldsymbol{f}^E]\!] = \boldsymbol{n} \cdot [\![\boldsymbol{T}^E]\!] = \boldsymbol{n} \cdot [\![\epsilon(\boldsymbol{E}\boldsymbol{E} - \tfrac{1}{2}E^2\boldsymbol{I})]\!], \tag{4.8a}$$

$$[\![\boldsymbol{f}^H]\!] = \boldsymbol{n} \cdot [\![\boldsymbol{T}^H]\!] = \boldsymbol{n} \cdot [\![-p^H\,\boldsymbol{I} + \mu\left(\boldsymbol{\nabla}\boldsymbol{v} + \boldsymbol{\nabla}\boldsymbol{v}^T\right)]\!]. \tag{4.8b}$$

The jump in electric tractions can be further simplified as

$$\begin{aligned}[\![\boldsymbol{f}^E]\!] &= [\epsilon E^n - \bar{\epsilon}\bar{E}^n]\boldsymbol{E}^t + \tfrac{1}{2}[\epsilon(E^{n2} - E^{t2}) - \bar{\epsilon}(\bar{E}^{n2} - E^{t2})]\boldsymbol{n} \\ &= q\boldsymbol{E}^t + [\![p^E]\!]\boldsymbol{n}.\end{aligned} \tag{4.9}$$

Here, $\boldsymbol{E}^t = (\boldsymbol{I} - \boldsymbol{n}\boldsymbol{n}) \cdot \boldsymbol{E}$ is the tangential electric field, which is continuous across the interface. The first term on the right hand side captures the tangential electric force arising from the action of the tangential field on the interfacial charge. The second term captures normal electric stresses and can be interpreted as a jump in an electric pressure p^E [88].

In the remainder of the paper, we scale all lengths by the radius a and times by the Maxwell-Wagner relaxation time τ_{MW}, which is the characteristic time scale

for polarization of the drop:

$$\tau_{MW} = \frac{\bar{\epsilon} + 2\epsilon}{\bar{\sigma} + 2\sigma}. \tag{4.10}$$

Electric and hydrodynamic stresses are non-dimensionalized by ϵE_0^2 and μ/τ_{MW}, respectively. Upon scaling of the governing equations, five dimensionless parameters emerge, three of which are ratios of material properties:

$$Q = \frac{\bar{\epsilon}}{\epsilon}, \quad R = \frac{\sigma}{\bar{\sigma}}, \quad \lambda = \frac{\bar{\mu}}{\mu}. \tag{4.11}$$

The product RQ, which sets the type of deformation and direction of the flow at steady state [88], can also be interpreted as the ratio of the inner and outer charge relaxation times:

$$RQ = \frac{\bar{\tau}}{\tau} \qquad \text{where} \qquad \tau = \frac{\epsilon}{\sigma}, \quad \bar{\tau} = \frac{\bar{\epsilon}}{\bar{\sigma}}. \tag{4.12}$$

The two remaining dimensionless parameters are chosen as the electric capillary number Ca_E denoting the ratio of electric to capillary forces, and the Mason number Ma denoting the ratio of viscous to electric stresses:

$$Ca_E = \frac{a\epsilon E_0^2}{\gamma}, \qquad Ma = \frac{\mu}{\epsilon \tau_{MW} E_0^2}. \tag{4.13}$$

The Mason number is directly related to the electric Reynolds number Re_E [103, 141, 90] as:

$$Re_E = \frac{1}{Ma} \frac{1 + 2R}{R(Q + 2)}. \tag{4.14}$$

It is instructive to note that the definition of the Mason number is based on the suspending fluid viscosity. In most cases the strength of charge convection is inversely proportional to the Mason number; however, for drop-fluid systems with high viscosity

ratios ($\lambda \gg 1$), the strength of charge convection can be weak even for small values of Ma.

4.3 Problem solution by domain perturbation

We solve the governing equations for axisymmetric shapes in the limit of small deformations [159, 2, 131], which occurs when surface tension is strong enough to overcome deformations due to electric stresses. This corresponds to the limit of $Ca_E \to 0$, and allows us to use an asymptotic approach in which we expand the drop deformation about the spherical shape and all the field variables in a small shape parameter δ whose relation with Ca_E we explain later. We employ the domain perturbation technique pioneered by Joseph [78], which was also used in a number of previous models for the dynamics of charged drops [163, 123].

4.3.1 Shape parametrization and expansion

In axisymmetric geometry, we parametrize the drop shape as a curve $\xi(r, \eta) = 0$, where $r = |\boldsymbol{x}|$ is the distance from the drop center and $\eta = \cos\theta$ is the cosine of the polar angle $\theta \in [0, \pi]$ measured from the field direction. For small deviations from sphericity, the drop shape is expanded on the basis of spherical harmonics as

$$\xi(r, \eta) = r - (1 + \delta f_1 + \delta^2 f_2) + O(\delta^3). \tag{4.15}$$

The first- and second-order shape functions are linear combinations of Legendre polynomials $\mathcal{L}_n$ of order n:

$$f_1 = f_{12}\mathcal{L}_2(\eta), \tag{4.16a}$$

$$f_2 = f_{20} + f_{22}\mathcal{L}_2(\eta) + f_{24}\mathcal{L}_4(\eta), \tag{4.16b}$$

where the deformations corresponding to $\mathcal{L}_2$ and $\mathcal{L}_4$ are illustrated in figure 4.1(b). The full line corresponds to the spherical shape, while the dashed line and dash-dotted line correspond to second-order $\mathcal{L}_2$ and fourth-order $\mathcal{L}_4$ deformation modes, respectively. We note the orthogonality condition

$$\int_0^\pi \mathcal{L}_i(\eta)\mathcal{L}_j(\eta)\sin\theta\,\mathrm{d}\theta = \frac{2}{2i+1}\delta_{ij}, \tag{4.17}$$

which will become useful later. The choice of Legendre functions in equations (4.16a)–(4.16b) is a consequence of the quadratic nature of the Maxwell electric stresses acting on the fluid-drop interface, which in a uniform electric field only excite shape modes of order 2^n ($n \in \mathbb{Z}^+$). In equations (4.16a)–(4.16b) and in the rest of the paper, pairs of indices in coefficients of the form f_{ij} refer to the order i in the small deformation expansion and to the order j of the Legendre polynomial they multiply, respectively. In equation (4.16b), the constant term f_{20} is added to the second-order shape function f_2 to negate the perturbation in the drop volume due to the first-order shape function f_1:

$$2\pi\int_0^\pi\int_0^r \rho^2\sin\theta\,\mathrm{d}\rho\,\mathrm{d}\theta = \frac{4\pi}{3} + 4\pi\delta^2\left(\frac{f_{12}^2}{5} + f_{20}\right) + O(\delta^3). \tag{4.18}$$

Requiring terms of order δ^2 to vanish, we get $f_{20} = -f_{12}^2/5$. The outward unit normal, tangent vector and curvature of the interface are also obtained as [2]

$$\boldsymbol{n} = \hat{\boldsymbol{e}}_r - \delta\,\partial_\theta f_1\,\hat{\boldsymbol{e}}_\theta + O(\delta^2), \quad \boldsymbol{t} = \hat{\boldsymbol{e}}_\theta + \delta\,\partial_\theta f_1\,\hat{\boldsymbol{e}}_r + O(\delta^2), \tag{4.19a}$$

$$\boldsymbol{\nabla}_s \cdot \boldsymbol{n} = 2 - \delta L[f_1] - \delta^2\{L[f_2] - 2f_1(L[f_1] - f_1)\} + O(\delta^3), \tag{4.19b}$$

where the differential operator L is defined as $L[f] = \partial_\eta\{(1-\eta^2)\partial_\eta f\} + 2f$.

Using the above parametrization, the normal and tangential components of any vector $\boldsymbol{v}$ and second-order tensor $\boldsymbol{T}$ on the drop surface are related to their components in spherical coordinates by

$$v^n = v_0^r + \delta(v_1^r + f_1\partial_r v_0^r - \partial_\theta f_1 v_0^\theta) + O(\delta^2), \tag{4.20a}$$

$$v^t = v_0^\theta + \delta(v_1^\theta + f_1\partial_r v_0^\theta + \partial_\theta f_1 v_0^r) + O(\delta^2), \tag{4.20b}$$

$$T^{nn} = T_0^{rr} + \delta(T_1^{rr} + f_1\partial_r T_0^{rr} - 2\partial_\theta f_1 T_0^{r\theta}) + O(\delta^2), \tag{4.20c}$$

$$T^{nt} = T_0^{r\theta} + \delta[T_1^{r\theta} + f_1\partial_r T_0^{r\theta} + \partial_\theta f_1(T_0^{rr} - T_0^{\theta\theta})] + O(\delta^2), \tag{4.20d}$$

where the terms on the right-hand side are to be evaluated at $r = 1$. These expressions will be useful below in determining the electric field, fluid velocity and stress distributions on the drop surface.

4.3.2 Electric problem

Spherical harmonic expansion

We first present the solution to the electric problem, which consists in solving equations (5.1)–(4.3) asymptotically. The electric potential outside and inside the drop can be expanded in powers of δ as

$$\varphi = \varphi_e(r,\theta) + \varphi_0(r,\theta) + \delta\varphi_1(r,\theta) + O(\delta^2), \tag{4.21a}$$

$$\bar{\varphi} = \varphi_e(r,\theta) + \bar{\varphi}_0(r,\theta) + \delta\bar{\varphi}_1(r,\theta) + O(\delta^2), \tag{4.21b}$$

which automatically satisfies the far-field boundary condition (4.3). We have yet to enforce continuity of the potential across the interface. To this end, we employ a domain perturbation approach in which all the boundary conditions are enforced approximately on the undeformed spherical surface $r = 1$. The potential on the interface is first expanded in the neighborhood of $r = 1$ using Taylor series:

$$\varphi = \varphi_e + \varphi_0 + \delta\left[\varphi_1 + f_1\partial_r(\varphi_e + \varphi_0)\right] + O(\delta^2), \tag{4.22a}$$

$$\bar{\varphi} = \bar{\varphi}_e + \bar{\varphi}_0 + \delta\left[\bar{\varphi}_1 + f_1\partial_r(\varphi_e + \bar{\varphi}_0)\right] + O(\delta^2). \tag{4.22b}$$

Applying continuity (4.2) and matching terms of zeroth- and first-order in δ provides two boundary conditions at $r = 1$:

$$\varphi_0 = \bar{\varphi}_0, \tag{4.23a}$$

$$\varphi_1 + f_1\partial_r(\varphi_e + \varphi_0) = \bar{\varphi}_1 + f_1\partial_r(\varphi_e + \bar{\varphi}_0). \tag{4.23b}$$

The zeroth-order problem, which is identical to the case of a sphere, is easily solved using decaying and growing spherical harmonics in terms of electric dipoles P_{01}, $\bar{P}_{01}$:

$$\varphi_0 = P_{01}r^{-2}\mathcal{L}_1(\eta), \tag{4.24a}$$

$$\bar{\varphi}_0 = \bar{P}_{01}r\mathcal{L}_1(\eta), \tag{4.24b}$$

and we require that $\bar{P}_{01} = P_{01}$ to satisfy (4.23a); solving for P_{01} will require application of the charge conservation equation (5.4) as detailed below. After substitution into equation (4.23b), we obtain a new first-order boundary condition:

$$\varphi_1 - \bar{\varphi}_1 = 3f_1 P_{01}\mathcal{L}_1(\eta) = 3f_{12}P_{01}\mathcal{L}_1(\eta)\mathcal{L}_2(\eta) = \tfrac{3}{5}f_{12}P_{01}[2\mathcal{L}_1(\eta) + 3\mathcal{L}_3(\eta)]. \quad (4.25)$$

The order of the polynomials appearing on the right-hand side suggests representing the first-order potentials in terms of both dipoles P_{11}, $\bar{P}_{11}$ and octupoles P_{13}, $\bar{P}_{13}$:

$$\varphi_1 = P_{11}r^{-2}\mathcal{L}_1(\eta) + P_{13}r^{-4}\mathcal{L}_3(\eta), \quad (4.26a)$$

$$\bar{\varphi}_1 = \bar{P}_{11}r\mathcal{L}_1(\eta) + \bar{P}_{13}r^3\mathcal{L}_3(\eta), \quad (4.26b)$$

and application of the boundary condition (4.25) yields the relations

$$\bar{P}_{11} = P_{11} - \tfrac{6}{5}f_{12}P_{01}, \qquad \bar{P}_{13} = P_{13} - \tfrac{9}{5}f_{12}P_{01}. \quad (4.27)$$

Having determined the electric potential, we can also obtain asymptotic expressions for the normal and tangential electric fields $E^n = -\boldsymbol{n}\cdot\boldsymbol{\nabla}\varphi$ and $E^t = -\boldsymbol{t}\cdot\boldsymbol{\nabla}\varphi$ on the drop surface. Applying equation (4.20a), we find

$$E^n = E_0^n + \delta E_1^n + O(\delta^2) = E_{01}^n\mathcal{L}_1(\eta) + \delta[E_{11}^n\mathcal{L}_1(\eta) + E_{13}^n\mathcal{L}_3(\eta)] + O(\delta^2), \quad (4.28)$$

with a similar expansion for $\bar{E}^n$. Finally, the expansion for the tangential electric field, which is continuous across the interface, is obtained using equation (4.20b) as

$$E^t = E_0^t + \delta E_1^t + O(\delta^2) = E_{00}^t\sin\theta + \delta[E_{10}^t + E_{12}^t\mathcal{L}_2(\eta)]\sin\theta + O(\delta^2), \quad (4.29)$$

The detailed expressions for the coefficients appearing in equations (4.28)–(4.29) are provided in appendix B.1.

Charge conservation and moment equations

To complete the solution of the electric problem, equations must be derived for the moments P_{01}, P_{11} and P_{13}, which are time-dependent. These can be obtained as ordinary differential equations by application of the charge conservation equation (5.4). First, we expand the charge density in powers of δ as

$$q = q_0 + \delta q_1 + O(\delta^2) = q_{01}\mathcal{L}_1(\eta) + \delta[q_{11}\mathcal{L}_1(\eta) + q_{13}\mathcal{L}_3(\eta)] + O(\delta^2). \tag{4.30}$$

Similarly, we expand the jump in Ohmic currents $\boldsymbol{n}\cdot[\![\boldsymbol{j}]\!] = [\![j]\!]^n$, scaled here by $\bar{\sigma}E_0$, as

$$[\![j]\!]^n = [\![j]\!]^n_0 + \delta[\![j]\!]^n_1 + O(\delta^2) = [\![j]\!]^n_{01}\mathcal{L}_1(\eta) + \delta\{[\![j]\!]^n_{11}\mathcal{L}_1(\eta) + [\![j]\!]^n_{13}\mathcal{L}_3(\eta)\} + O(\delta^2). \tag{4.31}$$

Expansion coefficients for both q and $[\![j]\!]^n$ are provided in appendix B.1. Finally, we formally expand the charge convection term in equation (5.4) as

$$\begin{aligned}\boldsymbol{\nabla}_s\cdot(q\boldsymbol{v}) &= [\boldsymbol{\nabla}_s\cdot(q\boldsymbol{v})]_0 + \delta[\boldsymbol{\nabla}_s\cdot(q\boldsymbol{v})]_1 + O(\delta^2),\\ &= [\boldsymbol{\nabla}_s\cdot(q\boldsymbol{v})]_{01}\mathcal{L}_1(\eta) + \delta\{[\boldsymbol{\nabla}_s\cdot(q\boldsymbol{v})]_{11}\mathcal{L}_1(\eta) + [\boldsymbol{\nabla}_s\cdot(q\boldsymbol{v})]_{13}\mathcal{L}_3(\eta)\} + O(\delta^2)\end{aligned} \tag{4.32}$$

where we have introduced the Legendre coefficients

$$[\boldsymbol{\nabla}_s\cdot(q\boldsymbol{v})]_{ij} = \frac{2j+1}{2}\int_0^\pi [\boldsymbol{\nabla}_s\cdot(q\boldsymbol{v})]_i\mathcal{L}_j(\eta)\sin\theta\,\mathrm{d}\theta. \tag{4.33}$$

Detailed expressions for these coefficients require knowledge of the interfacial velocity $\boldsymbol{v}$, whose calculation is presented in §5.3.2. Note that the zeroth-order charge convection term arising from the nonlinear product of the charge density q_0 and interfacial velocity $\boldsymbol{v}_0$ also involves an additional term of the form $[\boldsymbol{\nabla}_s \cdot (q\boldsymbol{v})]_{03}\mathcal{L}_3(\eta)$, which has been neglected here. To consider its effect, one would need to include a zeroth-order octupole P_{03} in equation (4.24), which in turn would generate charge convection terms of orders $1, 3, 5, 7, ...$ thus requiring additional higher-order odd multipoles. These multipoles becomes stronger with increasing electric Reynolds number or decreasing Mason number. Our theory is therefore valid in the limit of high Mason number, i.e. for drop-fluid systems in which charge convection is relatively weak.

Substituting the expansions (4.30), (4.31) and (4.32) into the charge conservation equation (5.4), matching powers of δ, and applying orthogonality of Legendre polynomials leads to a set of relaxation equations for the charge coefficients. In dimensionless form, these read

$$\dot{q}_{ij} + \frac{Q+2}{1+2R}\,[\![j]\!]^n_{ij} + [\boldsymbol{\nabla}_s \cdot (q\boldsymbol{v})]_{ij} = 0, \tag{4.34}$$

where the dot in the first term denotes differentiation with respect to time. If we further express q_{ij} and $[\![j]\!]^n_{ij}$ in terms of P_{01}, P_{11} and P_{13} using (B.3) and (B.4), we arrive at a set of hierarchical differential equations for the dipole and octupole moments:

$$\dot{P}_{01} + P_{01} = \frac{1-R}{1+2R} - \frac{1}{Q+2}[\boldsymbol{\nabla}_s \cdot (q\boldsymbol{v})]_{01}, \tag{4.35}$$

$$\begin{aligned}\dot{P}_{11} + P_{11} = {} & \frac{\mathrm{d}}{\mathrm{d}t}\left[\frac{6}{5}f_{12}\left(P_{01}\frac{1+2Q}{2+Q} + \frac{1-Q}{2+Q}\right)\right] + \frac{6}{5}f_{12}\left(P_{01}\frac{R+2}{2R+1} - \frac{1-R}{2R+1}\right) \\ & - \frac{1}{Q+2}[\boldsymbol{\nabla}_s \cdot (q\boldsymbol{v})]_{11},\end{aligned} \tag{4.36}$$

$$\begin{aligned}\dot{P}_{13} + \frac{Q+2}{3Q+4}\frac{4R+3}{2R+1}P_{13} = {} & \frac{\mathrm{d}}{\mathrm{d}t}\left[\frac{6}{5}f_{12}\left(P_{01}\frac{8+7Q}{8+6Q} - \frac{1-Q}{4+3Q}\right)\right] \\ & + \frac{6}{5}f_{12}\frac{Q+2}{3Q+4}\left(P_{01}\frac{8R+7}{4R+2} + \frac{1-R}{2R+1}\right) - \frac{1}{3Q+4}[\boldsymbol{\nabla}_s \cdot (q\boldsymbol{v})]_{13}.\end{aligned} \tag{4.37}$$

These coupled ordinary differential equations constitute the main result of this section. The external forcing in these equations is encapsulated in the first term on the right-hand side of (4.35), which describes the effect of the applied electric field on the leading-order dipole moment. It is also clear from equation (4.35) that charge convection cannot be neglected even at zeroth order as was previously done in the theories of Shutov [154] and Shkadov & Shutov [153]. Solving (4.35)–(4.37) requires the Legendre coefficients of the charge convection term as well as the first-order shape coefficient f_{12}. These unknowns will be determined below after we solve for the fluid flow, which affects both interfacial charge convection and droplet deformation.

4.3.3 Flow problem: streamfunction formulation

We now turn to the calculation of the fluid flow outside and inside the drop. Upon application of the field, electric stresses develop at the interface leading to deformations and flow. Since the flow is axisymmetric, we use a Stokes streamfunction

$\Psi(r,\theta)$ to determine the fluid velocity, which has components

$$v^r = \frac{1}{r^2\sin\theta}\partial_\theta\Psi, \qquad v^\theta = -\frac{1}{r\sin\theta}\partial_r\Psi, \tag{4.38}$$

in spherical coordinates. The streamfunction satisfies the biharmonic equation $\nabla^4\Psi = 0$, the general solutions to which outside and inside the drop are [82]:

$$\Psi = \sum_{n=2}^{\infty}(A_n r^{-n+1} + B_n r^{-n+3})\mathcal{G}_n(\eta), \qquad \bar{\Psi} = \sum_{n=2}^{\infty}(\bar{A}_n r^n + \bar{B}_n r^{n+2})\mathcal{G}_n(\eta), \tag{4.39}$$

where $\mathcal{G}_n(\eta)$ are Gegenbauer functions of degree $-1/2$ of the first kind [1]. They are related to Legendre polynomials and are regular everywhere in $-1 \le \eta \le 1$:

$$\mathcal{G}_n(\eta) = \frac{\mathcal{L}_{n-2}(\eta) - \mathcal{L}_n(\eta)}{2n-1}, \quad n \ge 2. \tag{4.40}$$

The first two functions are defined as $\mathcal{G}_0(\eta) = 1$ and $\mathcal{G}_1(\eta) = -\eta$, and we also note the property: $\mathcal{G}_n'(\eta) = -\mathcal{L}_{n-1}(\eta)$.

Following the same methodology as for the electric problem, we seek solutions as expansions in powers of δ. As will become evident in §4.3.5 when performing the stress balance on the interface, the zeroth- and first-order electric stresses acting on the interface at most induce fluid motions of the form

$$\Psi = \Psi_{03}\mathcal{G}_3(\eta) + \delta[\Psi_{13}\mathcal{G}_3(\eta) + \Psi_{15}\mathcal{G}_5(\eta)] + O(\delta^2), \tag{4.41a}$$

$$\bar{\Psi} = \bar{\Psi}_{03}\mathcal{G}_3(\eta) + \delta[\bar{\Psi}_{13}\mathcal{G}_3(\eta) + \bar{\Psi}_{15}\mathcal{G}_5(\eta)] + O(\delta^2), \tag{4.41b}$$

where

$$\Psi_{03} = A_{03} r^{-2} + B_{03}, \qquad \bar{\Psi}_{03} = \bar{A}_{03} r^{3} + \bar{B}_{03} r^{5}, \tag{4.42a}$$

$$\Psi_{13} = A_{13} r^{-2} + B_{13}, \qquad \bar{\Psi}_{13} = \bar{A}_{13} r^{3} + \bar{B}_{13} r^{5}, \tag{4.42b}$$

$$\Psi_{15} = A_{15} r^{-4} + B_{15} r^{-2}, \qquad \bar{\Psi}_{15} = \bar{A}_{15} r^{5} + \bar{B}_{15} r^{7}. \tag{4.42c}$$

In particular, the flow is entirely determined by twelve coefficients that are functions of time and that we proceed to solve for by application of the boundary conditions.

4.3.4 Kinematic boundary condition

The kinematic boundary condition relates the shape deformation to the fluid velocity so as to satisfy the no-slip and no-penetration boundary conditions at the interface. The streamfunction Ψ can be used to determine the normal and tangential components of the fluid velocity on the drop surface, which are obtained by combining equations (4.20a)–(4.20b) and (4.38) as

$$v^n = v^n_{02}\mathcal{L}_2(\eta) + \delta[v^n_{10} + v^n_{12}\mathcal{L}_2(\eta) + v^n_{14}\mathcal{L}_4(\eta)] + O(\delta^2), \tag{4.43a}$$

$$\bar{v}^n = \bar{v}^n_{02}\mathcal{L}_2(\eta) + \delta[\bar{v}^n_{10} + \bar{v}^n_{12}\mathcal{L}_2(\eta) + \bar{v}^n_{14}\mathcal{L}_4(\eta)] + O(\delta^2), \tag{4.43b}$$

$$v^t = v^t_{01}\mathcal{L}_1(\eta)\sin\theta + \delta[v^t_{11}\mathcal{L}_1(\eta) + v^t_{13}\mathcal{L}_3(\eta)]\sin\theta + O(\delta^2), \tag{4.43c}$$

$$\bar{v}^t = \bar{v}^t_{01}\mathcal{L}_1(\eta)\sin\theta + \delta[\bar{v}^t_{11}\mathcal{L}_1(\eta) + \bar{v}^t_{13}\mathcal{L}_3(\eta)]\sin\theta + O(\delta^2). \tag{4.43d}$$

The detailed expressions of the velocity coefficients are provided in appendix B.2. The no-penetration boundary condition is expressed as $v^n = \bar{v}^n = -\dot{\xi}$, which yields the

eight relations

$$v_{02}^n = \bar{v}_{02}^n = \delta \dot{f}_{12}, \qquad v_{10}^n = \bar{v}_{10}^n = \delta \dot{f}_{20}, \tag{4.44a, b}$$

$$v_{12}^n = \bar{v}_{12}^n = \delta \dot{f}_{22}, \qquad v_{14}^n = \bar{v}_{14}^n = \delta \dot{f}_{24}. \tag{4.44c, d}$$

Similarly, the no-slip boundary condition $v^t = \bar{v}^t$ dictates that

$$v_{01}^t = \bar{v}_{01}^t, \qquad v_{11}^t = \bar{v}_{11}^t, \qquad v_{13}^t = \bar{v}_{13}^t \tag{4.45a, b, c}.$$

The matching of orders in equation (4.44) might seem surprising at first due to the presence of terms involving δ on the right-hand side. However, it is the only possible solution as the leading-order term in $\dot{\xi}$ involves δ. This implies that temporal derivatives of the shape functions in fact scale as δ^{-1}, suggesting that the characteristic time scale for the shape transient is not the Maxwell-Wagner relaxation time used here for non-dimensionalization. This point will be made clearer in §4.4.2.

4.3.5 Dynamic boundary condition

We now proceed to enforce the dynamic boundary condition of equation (4.7), which in dimensionless form reads

$$\boldsymbol{n} \cdot (\llbracket \boldsymbol{T}^E \rrbracket + Ma \llbracket \boldsymbol{T}^H \rrbracket) = \frac{1}{Ca_E} (\boldsymbol{\nabla}_s \cdot \boldsymbol{n}) \boldsymbol{n}, \tag{4.46}$$

and requires us to evaluate electric and hydrodynamic stresses on the interface.

Electric and hydrodynamic stresses

As previously shown in equation (4.9), the jump in electric tractions can be decomposed into tangential and normal components, both of which involve quadratic products of expansions derived above. The tangential component $q\boldsymbol{E}^t = qE^t\boldsymbol{t}$ is continuous and is expanded as

$$qE^t = [qE^t]_{01}\mathcal{L}_1(\eta)\sin\theta + \delta\{[qE^t]_{11}\mathcal{L}_1(\eta) + [qE^t]_{13}\mathcal{L}_3(\eta)\}\sin\theta + O(\delta^2). \tag{4.47}$$

Similarly, the expansion for the jump in electric pressure in equation (4.9) is found to be

$$[\![p^E]\!] = [\![p^E]\!]_{00} + [\![p^E]\!]_{02}\mathcal{L}_2(\eta) + \delta\{[\![p^E]\!]_{10} + [\![p^E]\!]_{12}\mathcal{L}_2(\eta) + [\![p^E]\!]_{14}\mathcal{L}_4(\eta)\} + O(\delta^2). \tag{4.48}$$

The expressions for the coefficients are provided in appendix B.1.

The jump in hydrodynamic tractions is evaluated using equations (4.20c)–(4.20d), in which the requisite components of the stress tensor in spherical coordinates are obtained from the velocity components as

$$T^{H,rr} = -p^H + 2\partial_r v^r, \qquad \bar{T}^{H,rr} = -\bar{p}^H + 2\lambda\partial_r \bar{v}^r, \tag{4.49a}$$

$$T^{H,r\theta} = r^{-1}\partial_\theta v^r + r\partial_r(v^\theta r^{-1}), \qquad \bar{T}^{H,r\theta} = \lambda[r^{-1}\partial_\theta \bar{v}^r + r\partial_r(\bar{v}^\theta r^{-1})], \tag{4.49b}$$

$$T^{H,\theta\theta} = -p^H + 2r^{-1}(\partial_\theta v_\theta + v_r), \qquad \bar{T}^{H,\theta\theta} = -\bar{p}^H + 2r^{-1}\lambda(\partial_\theta \bar{v}_\theta + \bar{v}_r). \tag{4.49c}$$

The diagonal stress components $T^{H,rr}$ and $T^{H,\theta\theta}$ involve the fluid pressure p^H, which can be obtained from the velocity by integration of the momentum equation. After some algebra, the jumps in hydrodynamic stresses induced by the zeroth- and first-order

streamfunctions Ψ_0, Ψ_1, scaled with μ/τ_{MW}, are found as

$$\begin{aligned}
[\![T^H]\!]^{nn} &= [\![T^H]\!]_0^{nn} + \delta[\![T^H]\!]_1^{nn} + O(\delta^2) \\
&= [\![T^H]\!]_{00}^{nn} + [\![T^H]\!]_{02}^{nn}\mathcal{L}_2(\eta) \\
&\quad + \delta\{[\![T^H]\!]_{10}^{nn} + [\![T^H]\!]_{12}^{nn}\mathcal{L}_2(\eta) + [\![T^H]\!]_{14}^{nn}\mathcal{L}_4(\eta)\} + O(\delta^2), \qquad (4.50a) \\
[\![T^H]\!]^{nt} &= [\![T^H]\!]_0^{nt} + \delta[\![T^H]\!]_1^{nt} + O(\delta^2) \\
&= [\![T^H]\!]_{01}^{nt}\mathcal{L}_1(\eta)\sin\theta + \delta\{[\![T^H]\!]_{11}^{nt}\mathcal{L}_1(\eta) + [\![T^H]\!]_{13}^{nt}\mathcal{L}_3(\eta)\}\sin\theta + O(\delta^2), \qquad (4.50b)
\end{aligned}$$

where the various coefficients can all be expressed in terms of B_{03}, B_{13}, B_{15} as detailted in appendix B.2.

Stress balance

The electric and hydrodynamic traction jumps can now be substituted into the stress balance (5.8) to satisfy the dynamic boundary condition. In the normal direction, the stress balance requires:

$$[\![p^E]\!]_{00} + Ma\,[\![T^H]\!]_{00}^{nn} = \frac{2}{Ca_E}, \qquad (4.51a)$$

$$[\![p^E]\!]_{02} + Ma\,[\![T^H]\!]_{02}^{nn} = \frac{4}{Ca_E}\delta f_{12}, \qquad (4.51b)$$

$$[\![p^E]\!]_{10} + Ma\,[\![T^H]\!]_{10}^{nn} = -\frac{2}{Ca_E}\delta f_{12}^2, \qquad (4.51c)$$

$$[\![p^E]\!]_{12} + Ma\,[\![T^H]\!]_{12}^{nn} = \frac{4}{Ca_E}\delta(f_{22} - \tfrac{5}{7}f_{12}^2), \qquad (4.51d)$$

$$[\![p^E]\!]_{14} + Ma\,[\![T^H]\!]_{14}^{nn} = \frac{18}{Ca_E}\delta(f_{24} - \tfrac{2}{7}f_{12}^2). \qquad (4.51e)$$

In the tangential direction, it yields

$$[qE^t]_{01} + Ma\,[\![T^H]\!]^{nt}_{01} = 0, \tag{4.52a}$$

$$[qE^t]_{11} + Ma\,[\![T^H]\!]^{nt}_{11} = 0, \tag{4.52b}$$

$$[qE^t]_{13} + Ma\,[\![T^H]\!]^{nt}_{13} = 0. \tag{4.52c}$$

The above balances now allow us to define more explicitly the value of the small deformation parameter δ. The driving force for the flow is the tangential electric stress $q\boldsymbol{E}^t$, which according to equations (4.52) induces hydrodynamic tractions scaling with $O(Ma^{-1})$. The magnitude of the resulting flow therefore is such that all normal tractions, both electric and hydrodynamic, in equation (4.51) are of order $O(1)$. Balancing these tractions with surface tension forces thus requires us to choose $\delta \propto Ca_E$. For consistency with previous small deformation theories, we define δ explicitly as

$$\delta = \frac{3\,Ca_E}{4(1+2R)^2}. \tag{4.53}$$

In particular, the assumption of small deformation yields no restriction on the magnitude of the Mason number, which is only constrained by the approximation discussed in §4.3.2.

4.3.6 Nonlinear charge convection

As a final calculation, we determine the Legendre coefficients of the nonlinear convection term in the charge convection equation (5.4). The convection term is

straightforward to calculate after applying the identity

$$\boldsymbol{\nabla}_s \cdot (q\boldsymbol{v}) = qv^n(\boldsymbol{\nabla}_s \cdot \boldsymbol{n}) + \boldsymbol{\nabla}_s \cdot (q\boldsymbol{v}^t), \tag{4.54}$$

in which the expansions for q, v^n, $\boldsymbol{v}^t = v^t\boldsymbol{t}$, and $\boldsymbol{\nabla}_s \cdot \boldsymbol{n}$ can be substituted together with

$$\boldsymbol{\nabla}_s = [\boldsymbol{I} - \hat{\boldsymbol{e}}_r\hat{\boldsymbol{e}}_r + \delta(\hat{\boldsymbol{e}}_r\hat{\boldsymbol{e}}_\theta + \hat{\boldsymbol{e}}_\theta\hat{\boldsymbol{e}}_r)] \cdot \boldsymbol{\nabla} + O(\delta^2). \tag{4.55}$$

All calculations done, the relevant Legendre coefficients appearing in equations (4.35)–(4.37) for the dipole and octupole moments are found to be

$$[\boldsymbol{\nabla}_s \cdot (q\boldsymbol{v})]_{01} = -\tfrac{2}{5}q_{01}B_{03} + \tfrac{6}{5}q_{01}\delta\dot{f}_{12}, \tag{4.56a}$$

$$\begin{aligned}[\boldsymbol{\nabla}_s \cdot (q\boldsymbol{v})]_{11} = {}& \tfrac{2}{5}q_{01}A_{13} + \tfrac{2}{5}q_{11}A_{03} - \tfrac{6}{35}q_{13}A_{03} - \tfrac{54}{35}q_{01}A_{03}f_{12} \\ & + \tfrac{4}{5}q_{01}\delta\dot{f}_{22} + \tfrac{4}{5}q_{11}\delta\dot{f}_{12} + \tfrac{18}{35}q_{13}\delta\dot{f}_{12} + \tfrac{38}{35}q_{01}\delta f_{12}\dot{f}_{12},\end{aligned} \tag{4.56b}$$

$$\begin{aligned}[\boldsymbol{\nabla}_s \cdot (q\boldsymbol{v})]_{13} = {}& \tfrac{8}{5}q_{01}A_{13} + \tfrac{4}{3}q_{01}A_{15} + \tfrac{2}{3}q_{01}B_{15} + \tfrac{8}{5}q_{11}A_{03} \\ & + \tfrac{4}{15}q_{13}A_{03} - \tfrac{104}{15}q_{01}A_{03}f_{12} + \tfrac{6}{5}q_{01}\delta\dot{f}_{22} + \tfrac{8}{9}q_{01}\delta\dot{f}_{24} \\ & + \tfrac{6}{5}q_{11}\delta\dot{f}_{12} + \tfrac{8}{15}q_{13}\delta\dot{f}_{12} - \tfrac{4}{5}q_{01}\delta f_{12}\dot{f}_{12}.\end{aligned} \tag{4.56c}$$

4.4 Summary of the small-deformation theory

The set of asymptotic expansions obtained in §4.3 provides a closed system of equations for all unknown coefficients. We summarize here the results of the theory and outline the solution procedure at first and second order. We also compare and contrast our predictions with the existing theories of Taylor [159], Ajayi [2], Esmaeeli & Sharifi [48] and Lanauze *et al.* [89].

4.4.1 Taylor deformation parameter

For easy comparison with previous theories and experiments, we introduce Taylor's deformation parameter $\mathcal{D}$, defined as

$$\mathcal{D} = \frac{r^{\parallel} - r^{\perp}}{r^{\parallel} + r^{\perp}}, \tag{4.57}$$

where $r^{\parallel}$ and $r^{\perp}$ denote the length of the drop in directions parallel and perpendicular to the electric field, respectively. The sign of $\mathcal{D}$ distinguishes between oblate ($\mathcal{D} < 0$) and prolate ($\mathcal{D} > 0$) shapes. For an axisymmetric drop, $r^{\parallel}$ and $r^{\perp}$ are reached at $\theta = 0$ and $\pi/2$, respectively:

$$r^{\parallel} = r(0) = 1 + \delta f_{12} + \delta^2 \left(f_{20} + f_{22} + f_{24}\right) + O(\delta^3), \tag{4.58a}$$

$$r^{\perp} = r(\pi/2) = 1 - \tfrac{1}{2}\delta f_{12} + \delta^2 \left(f_{20} - \tfrac{1}{2} f_{22} + \tfrac{3}{8} f_{24}\right) + O(\delta^3), \tag{4.58b}$$

from which we find

$$\mathcal{D} = \tfrac{3}{4}\left[\delta f_{12} + \delta^2 \left(f_{22} + \tfrac{5}{12} f_{24} - \tfrac{1}{4} f_{12}^2\right)\right] + O(\delta^3). \tag{4.59}$$

4.4.2 First-order theory

We first summarize the first-order theory, which allows us to compare our results with those of Taylor [159], Esmaeeli & Sharifi [48] and Lanauze *et al.* [89]. The zeroth-order stress balance equations (4.51*b*) and (4.52*a*), together with the dipole relaxation equation (4.35), provide three coupled equations for the three unknowns B_{03}, f_{12} and P_{01}. We first eliminate B_{03} by combining (4.51*b*) and (4.52*a*), and

after manipulations we arrive at a coupled system of first-order ordinary differential equations of the form

$$\frac{\mathrm{d}}{\mathrm{d}t}\begin{bmatrix} P_{01} \\ f_{12} \end{bmatrix} = \mathcal{F}_1(P_{01}, f_{12}; Ca_E, Ma, R, Q, \lambda), \tag{4.60}$$

where $\mathcal{F}_1$ is a nonlinear function whose explicit form is cumbersome and is omitted here for brevity. These equations can be integrated numerically in time subject to initial conditions. In all of the results shown below, we assume that the drop surface is initially spherical and does not carry any charge at $t = 0$, which provides the initial conditions:

$$P_{01}(0) = \frac{Q-1}{Q+2}, \qquad f_{12}(0) = 0. \tag{4.61}$$

Equations (4.60) can easily be compared to previous first-order theories. First, neglecting charge convection decouples the dipole evolution equation from the fluid problem, yielding the simple relaxation equation

$$\dot{P}_{01} + P_{01} = \frac{1-R}{1+2R}, \tag{4.62}$$

the solution to which is:

$$P_{01} = \frac{1-R}{1+2R} + \left(\frac{Q-1}{Q+2} - \frac{1-R}{1+2R}\right)\mathrm{e}^{-t}. \tag{4.63}$$

Substituting (4.63) into equation (4.60) then yields a simplified model which is similar to that of Lanauze *et al.* [89] when the effect of fluid inertia is negligible. If we further neglect charge relaxation, we can easily solve for the transient deformation parameter

as

$$\mathcal{D}(t) = \mathcal{D}_T(1 - \mathrm{e}^{-t/\tau_d}) \qquad \text{where} \qquad \tau_d = \frac{a\mu}{\gamma}\frac{(19\lambda + 16)(2\lambda + 3)}{40(\lambda + 1)}, \tag{4.64}$$

which matches the result of Esmaeeli & Sharifi [48]. In particular, the viscous-capillary time scale τ_d emerges as the characteristic time scale for shape deformations, which also rationalizes the seeming contradiction in the matching of terms in the kinematic boundary of equation (4.44). Here, $\mathcal{D}_T$ is the steady first-order deformation parameter first obtained by Taylor [159] as

$$\mathcal{D}_T = \frac{9}{16}\frac{\Phi_T}{(1 + 2R)^2}Ca_E \tag{4.65}$$

in terms of Taylor's discriminating function Φ_T:

$$\Phi_T = (1 - R)^2 + R(1 - RQ)\left[2 + \frac{3}{5}\frac{2 + 3\lambda}{1 + \lambda}\right]. \tag{4.66}$$

Note that equation (4.64) predicts an exponential relaxation towards the steady drop shape and therefore fails to capture the non-monotonic transient deformation observed in experiments and simulations [90] and also predicted by the full solution of equations (4.60) as we discuss in §5.4.

4.4.3 Second-order theory

The first-order theory can then be improved by solution of the second-order equations, which involve the additional unknowns B_{13}, B_{15}, f_{22}, f_{24}, P_{11}, and P_{13}. These are provided by the first-order normal and tangential stress balances of equations

(4.51c), (4.51e), (4.52b) and (4.52c), together with the moment evolution equations (4.36)–(4.37). The flow unknowns B_{13} and B_{15} can be eliminated by manipulating equations (4.51c) and (4.52b) for B_{13}, and equations (4.51e) and (4.52c) for B_{15}. When combined with the moment evolution equations, this yields a system a differential equations of the form

$$\frac{\mathrm{d}}{\mathrm{d}t}\begin{bmatrix} P_{11} \\ P_{13} \\ f_{22} \\ f_{24} \end{bmatrix} = \mathcal{F}_2(P_{11}, P_{13}, f_{22}, f_{24}; P_{01}, f_{12}; Ca_E, Ma, R, Q, \lambda), \tag{4.67}$$

where $\mathcal{F}_2$ is another nonlinear function. Once again, these equations can be integrated in time numerically to obtain the multipole moments as well as shape functions entering Taylor's deformation parameter of equation (4.59). The initial conditions for these variables in the case of an initially spherical and uncharged drop are

$$P_{11}(0) = P_{13}(0) = f_{22}(0) = f_{24}(0) = 0. \tag{4.68}$$

If charge convection is neglected, equations (4.36)–(4.37) for the moments become uncoupled from the flow problem and only involve electric parameters. At steady state, the first-order multipole moments are then obtained as

$$P_{11} = \frac{6}{5} f_{12} \left(\frac{1-R}{1+2R}\right)^2, \qquad P_{13} = \frac{9}{5} f_{12} \frac{1-R}{1+2R}, \tag{4.69}$$

which matches equations (25) and (26) in the work of Ajayi [2]. The numerical codes solving systems (4.60) and (4.67) are available upon request.

Table 4.1: Material properties: systems 1, 2 and 3 correspond to the experiments of Lanauze *et al.* [90], Salipante & Vlahovska [141] and Tsukada *et al.* [165], respectively. $\epsilon_0 = 8.8542 \times 10^{-12}\,\mathrm{F.m^{-1}}$ denotes the permittivity of vacuum.

System	ϵ/ϵ_0	$\bar{\epsilon}/\epsilon_0$	σ ($\mathrm{S.m^{-1}}$)	$\bar{\sigma}$ ($\mathrm{S.m^{-1}}$)	μ (Pa.s)	$\bar{\mu}$ (Pa.s)	γ ($\mathrm{mN.m^{-1}}$)
1a	4.9	2.8	5.8×10^{-11}	0.2×10^{-11}	0.68	0.05	4.5
1b	4.9	2.8	5.8×10^{-11}	0.2×10^{-11}	0.68	0.05	4.5
1c	4.9	2.8	5.8×10^{-11}	0.2×10^{-11}	0.68	0.05	4.5
2a	5.3	3.0	4.5×10^{-11}	0.12×10^{-11}	0.69	0.97	4.5
2b	5.3	3.0	4.5×10^{-11}	0.12×10^{-11}	0.69	0.97	4.5
3	2.5	4.3	2.7×10^{-12}	1.7×10^{-10}	0.017	0.254	3.0

Table 4.2: Material properties: systems 1, 2 and 3 with drop radius and electric field strength.

System	a (mm)	E_0 ($\mathrm{kV.cm^{-1}}$)
1a	2.0	1.6
1b	2.0	2.1
1c	2.0	6.1
2a	0.7	0.45–2.0
2b	2.1	0.26–1.2
3	2.5	2.0–9.2

4.5 Results and discussion

We now compare our theoretical results with existing experimental data, previous small-deformation theories, as well as fully nonlinear numerical simulations using an axisymmetric boundary element method described in appendix B.3. The material properties, drop sizes and electric field strengths are chosen as in table 4.1 to match the experimental values of Lanauze *et al.* [90] (system 1), who measured transient drop dynamics, and of Salipante & Vlahovska [141] (system 2) for steady deformations, and corresponding dimensionless parameter values are provided in table 4.3. Both

Table 4.3: Dimensionless parameters corresponding to the material properties of table 4.1: systems 1, 2, 3 and 4 correspond to the experiments of Lanauze *et al.* [90], Salipante & Vlahovska [141], Tsukada *et al.* [165] and Ha & Yang [58], respectively.

System	R	Q	λ	Ca_E	Ma
1a	29.0	0.57	0.074	0.49	0.65
1b	29.0	0.57	0.074	0.85	0.375
1c	29.0	0.57	0.074	7.18	0.045
2a	36.6	0.57	1.41	0.03–0.6	0.27–5.4
2b	36.6	0.57	1.41	0.03–0.6	0.8–16
3	0.016	1.72	14.7	0.0075–0.155	0.2–4.1
4	0.1	1.37	1	0.3	0.5

of these studies considered oblate drops. We also present a few results on prolate drops using the experimental values of Tsukada *et al.* [165] (system 3) and Ha & Yang [58] (system 4). The latter study, however, did not report all the material properties required to construct all five dimensionless parameters in our model; we choose to set the values of the electric capillary number and Mason number to $Ca_E = 0.3$ and $Ma = 0.5$ in this case.

4.5.1 Effect of transient charge relaxation and shape deformation

In this section, we first neglect nonlinear charge convection and focus on the effects of transient charge relaxation and transient shape deformation alone. Here we adopt the experimental values of system 1b. The drop deformation is plotted as a function of time in figure 4.2 for three distinct cases. In figure 4.2(a), both nonlinear charge convection and transient charge relaxation are neglected. In this case, the only time dependence enters through the temporal derivatives of the shape functions. We find that the drop shape becomes oblate ($\mathcal{D} < 0$), and our theoretical

results asymptote at long times towards the steady-state predictions of Taylor [159] and Ajayi [2] at first- and second-order, respectively. Both steady states, however, overpredict the drop deformation, and it is found, rather curiously, that the theory performs more poorly at second order than at first order; this was already noted by Ajayi [2] and is a consequence of neglecting charge convection as further discussed below. The transient is also poorly captured: the model predicts a monotonic increase of the drop deformation towards the oblate steady state and fails to capture the initial dynamics seen in experiments, where the drop first adopts a prolate shape before becoming oblate. Figure 4.2(b) shows the opposite situation in which transient shape deformation is neglected but transient charge relaxation is included. In this case, the shape instantaneously adjusts to the charge distribution, which explains the immediate deformation to a prolate shape at $t = 0$ as a result of the instantaneous polarization of the drop according to equation (4.61). The deformation subsequently relaxes monotonically towards its steady oblate value. However, accounting for both transient phenomena in figure 4.2(c) captures the transient dynamics correctly while still evolving towards the steady deformation values of Taylor [159] and Ajayi [2] in the absence of charge convection. These results underscore the importance of including all transient effects if one wants to capture the correct shape dynamics.

4.5.2 Effect of nonlinear charge convection

We now turn to the full theoretical model, which includes transient charge and shape relaxation as well as nonlinear charge convection. As we show here, the main effect of charge convection is to reduce the strength of the interfacial velocity, thereby causing oblate drops to deform less but prolate drops to deform more in

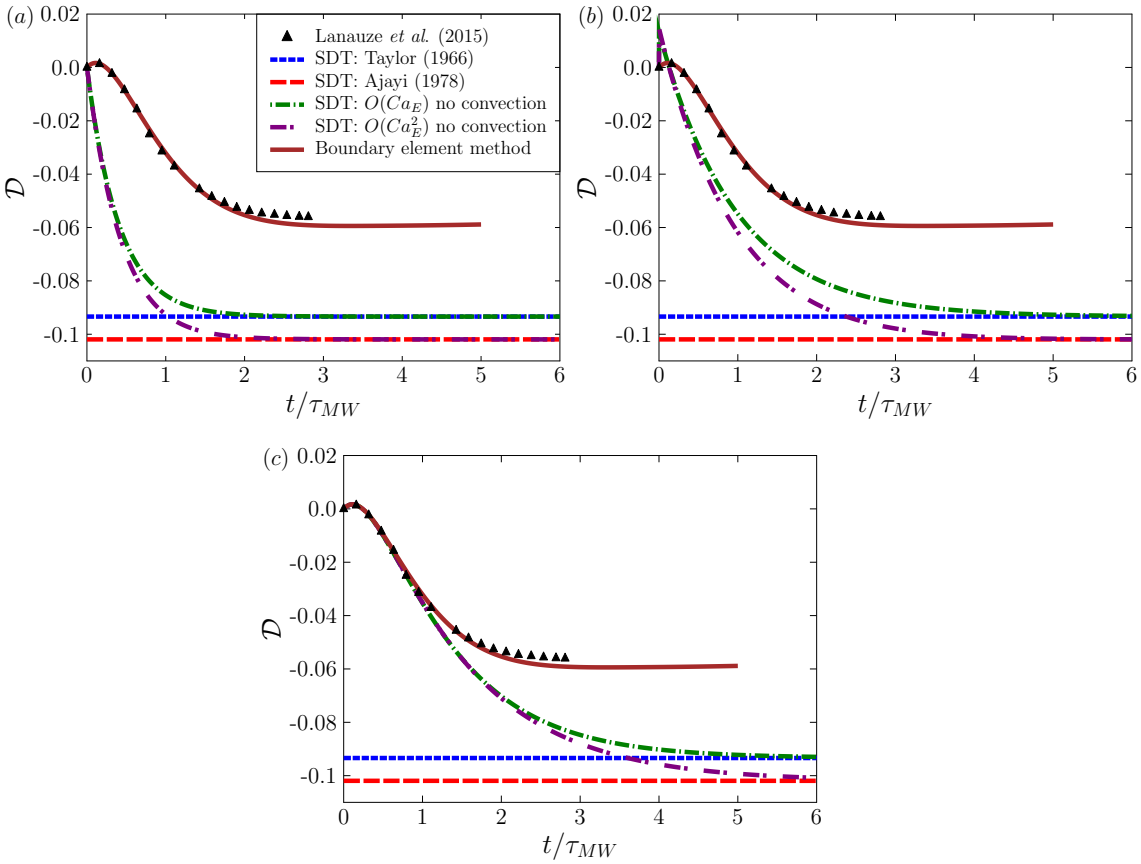

Figure 4.2: Deformation parameter $\mathcal{D}$ as a function of time for the parameters of system 1b in the absence of charge convection: (a) effect of transient shape relaxation only (no transient charge relaxation), (b) effect of transient charge relaxation only (no transient shape relaxation), and (c) effect of both transient shape and charge relaxation. Symbols show experimental data of Lanauze *et al.* [90]. Boundary element simulation results using the full nonlinear model and the algorithm of appendix B.3 are also shown.

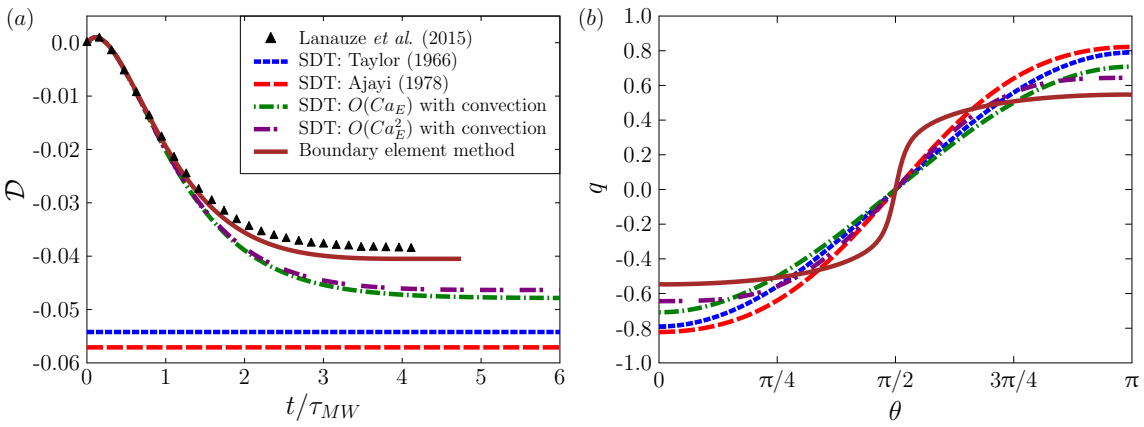

Figure 4.3: (a) Deformation parameter $\mathcal{D}$ as a function of time for the parameters of system 1a. (b) Steady interfacial charge profile. The plots show experimental results of Lanauze *et al.* [90], fully nonlinear boundary element simulations, first- and second-order small-deformation theory (with nonlinear charge convection), and the steady results of Taylor [159] and Ajayi [2] that neglected charge convection.

agreement with computational studies [49, 90]. We first consider the dynamics in a relatively weak electric field using the parameters of system 1a in figure 4.3 (the plots show experimental results of Lanauze *et al.* [90], fully nonlinear boundary element simulations, first- and second-order small-deformation theory (with nonlinear charge convection), and the steady results of Taylor [159] and Ajayi [2] that neglected charge convection). First, we note in figure 4.3(a) that the boundary element simulations perform best and capture both the transient and the steady state with very good accuracy. Our small deformation theory with charge convection also captures the transient very well but still slightly overpredicts the steady deformation parameter, albeit not as much as the models of Taylor [159] and Ajayi [2]. Interestingly, we find that while the second-order theory of Ajayi is worse than the first-order theory of Taylor in the absence of charge convection, such is not the case in our model where including second-order terms is seen to improve the solution. The poor performance of Ajayi's model is a direct consequence of the neglect of charge convection, which

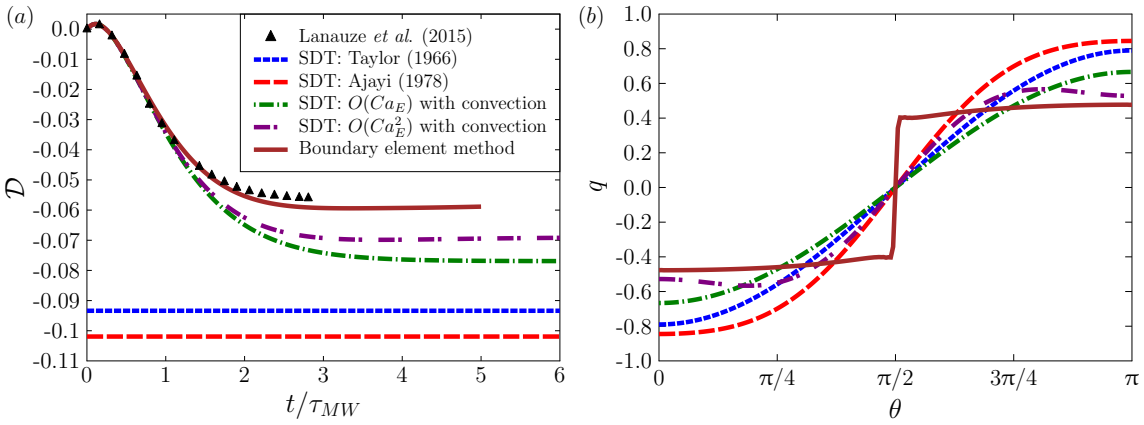

Figure 4.4: (a) Deformation parameter $\mathcal{D}$ as a function of time for the parameters of system 1b. (b) Steady interfacial charge profile. For these parameter values, the charge distribution predicted by the boundary element simulation develops a discontinuity at the equator.

results in a stronger dipole moment and in turn leads to larger deformations. Charge convection by the flow, on the other hand, causes the transport of positive and negative charges from the poles towards the equator, thus effectively reducing the induced dipole. This point is evident in figure 4.3(b) showing the steady charge distribution on the drop surface, where we see that the second-order theory with charge convection best approximates the charge profile from boundary element simulations. This numerical charge profile, however, exhibits a sharper transition from negative to positive values at the equator.

The effect of increasing field strength is shown in figure 4.4 corresponding to system 1b. Unsurprisingly, stronger fields cause larger drop deformations, which are not as easily captured by the theory. While the boundary element simulation matches the experimental data quite well, our nonlinear small-deformation theory captures the transient well but shows a significant departure at steady state. Nevertheless, the second-order theory still outperforms all previous theoretical models. The difficulty in capturing the steady state accurately can be understood by considering the charge

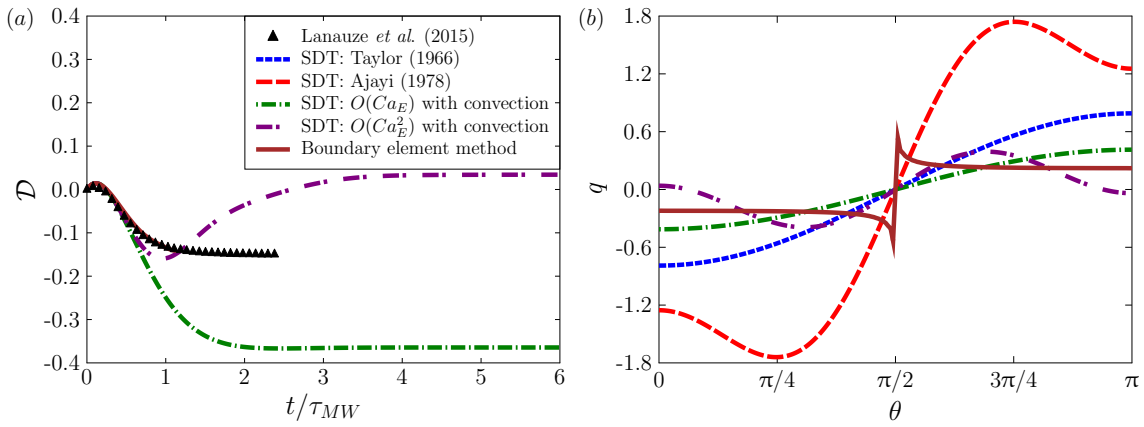

Figure 4.5: (a) Deformation parameter $\mathcal{D}$ as a function of time for the parameters of system 1c. (b) Steady interfacial charge profile. The steady deformation values predicted by the models of [159] and Ajayi [2] in this case are -0.75 and -1.40, respectively, and out of the frame of figure (a). For these parameter values, the charge discontinuity at the equator is so severe that the boundary element simulations blow up before reaching steady state; in this case, the charge profile shown in (b) corresponds to a time before the instability develops.

profile in figure 4.4(b), where a sharp gradient is observed across the equator in the numerical data from boundary element simulations. This sharp gradient cannot be captured using only two Legendre functions as in the expansion of equation (4.30), which explains the discrepancy. The problem becomes yet more severe in stronger fields, as shown in figure 4.5 in the case of system 1c. There, an actual discontinuity appears in the charge profile, leading to the very poor performance of small-deformation theories and to numerical instabilities in the boundary element simulation, which blows up before reaching steady state. The formation of a charge shock in strong fields was first observed in the simulations of Lanauze *et al.* [90], who also were not able to resolve it numerically using their boundary element algorithm based on spline interpolation. The boundary element method used here and described in appendix B.3 solves the charge conservation equation using finite volumes and yet is still unable

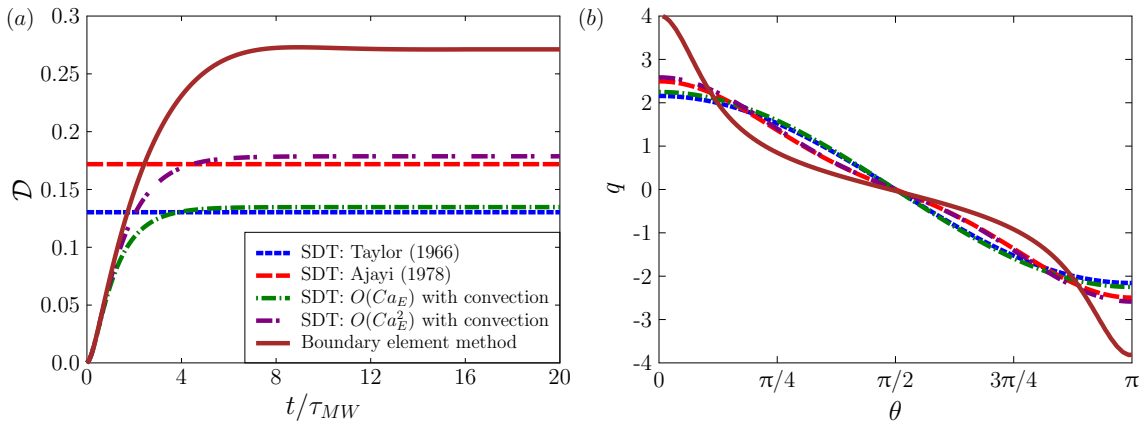

Figure 4.6: (a) Deformation parameter $\mathcal{D}$ as a function of time for the parameters of system 4, which correspond to a steady prolate shape. (b) Steady interfacial charge profile.

to capture the discontinuity, suggesting that higher-order non-oscillating numerical schemes should be employed towards this purpose [97].

The case of prolate deformations is illustrated in figure 4.6 using the parameters of system 4. In this case, the drop deformation increases monotonically with time. The steady deformation parameter obtained by simulations with $Ma = 0.5$ is $\mathcal{D} = 0.27$, which slightly exceeds the value of $\mathcal{D} = 0.22$ found by Lac & Homsy [88], who neglected charge convection ($Ma \to \infty$); the experiments of Ha & Yang [58], for which the value of Ma is unknown, reported a deformation of $\mathcal{D} = 0.25$. Our small deformation theory only provides a modest improvement at steady state over the predictions of Taylor [159] and Ajayi [2], again confirming that nonlinear charge convection has a weaker effect for prolate drops. This again can be rationalized by considering the interfacial charge profile in figure 4.6(b): convection by the flow is seen to cause charge accumulation at the drop poles, and thus does not cause any discontinuity as in the oblate case. Instead, the charge profile remains relatively smooth and therefore can be reasonably well approximated using Legendre polynomials.

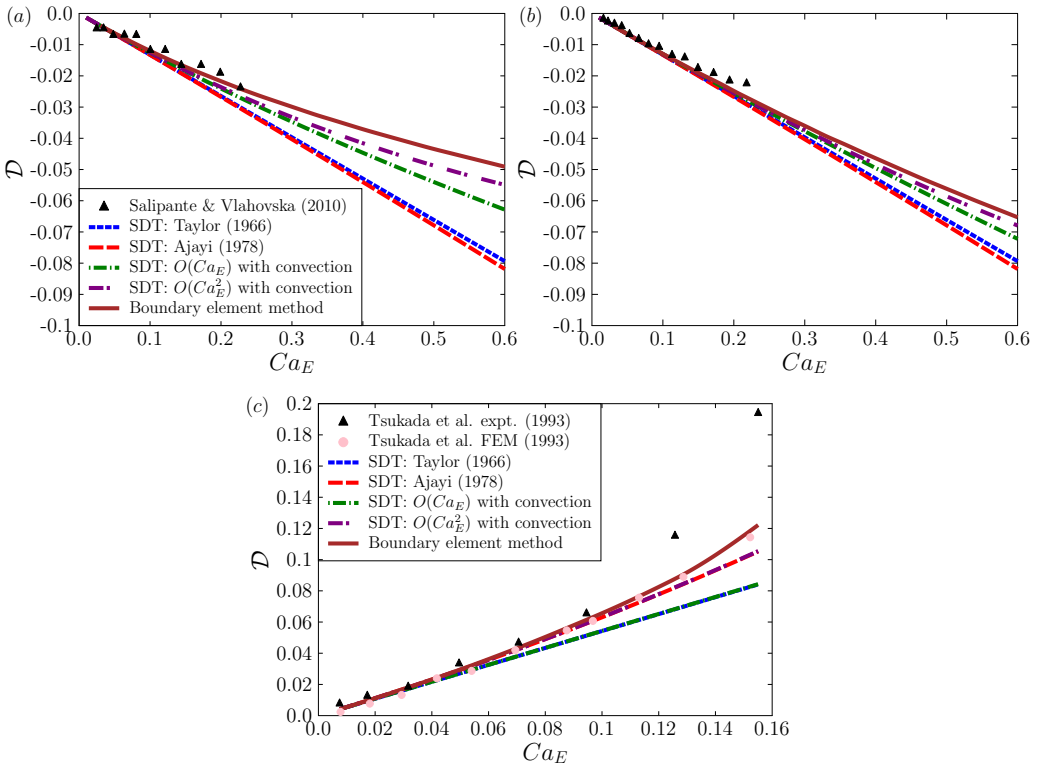

Figure 4.7: Steady drop deformation $\mathcal{D}$ as a function of electric capillary number Ca_E for the parameters of: (a) system 2a, (b) system 2b, and (c) system 3. The various models are compared to the experimental measurements of Salipante & Vlahovska [141] and Tsukada *et al.* [165].

As a final test, we compare our theoretical and numerical predictions for the steady drop shapes with the experimental results of Salipante & Vlahovska [141] for systems 2a and 2b with oblate drops and Tsukada *et al.* [165] for system 3 with prolate drops in figure 4.7. The experimental system 2 used two different drop sizes but identical material properties. At a given value of the electric capillary number Ca_E, increasing drop size is equivalent to decreasing the electric field or increasing the Mason number Ma, which reduces the effect of charge convection. Charge convection is therefore more significant in figure 4.7(a) for the smaller drop size, and indeed departures of our numerical and theoretical results from the small-deformation theories of Taylor [159] and Ajayi [2] are more significant in this case. In both cases, our theoretical model performs quite well at predicting the steady drop shape, but still slightly overpredicts the experimental values especially as Ca_E increases; nonetheless the agreement is noticeably better than in previous models. The effect of charge convection is extremely weak in the case of prolate drops in system 3 as shown in figure 4.7(c). As a consequence, our first and second order theories are indistinguishable from Taylor's and Ajayi's results, and the deformations predicted by our axisymmetric boundary element method only slightly exceed the finite element simulation values of Tsukada *et al.* [165] who neglected charge convection.

4.6 Conclusion

In summary, we have developed a small-deformation theory for the complete Melcher-Taylor leaky dielectric model including the non-linear charge convection term. The theory is most relevant for small-sized drops or drops with high surface tension but non-negligible charge convection. A domain perturbation method based on spherical

harmonics valid for small deviations from sphericity was employed to represent the drop shape up to second order in electric capillary number $O(Ca_E^2)$. The zeroth- and first-order electric and flow fields were solved for using multipole expansions. On making the appropriate assumptions, we were able to recover the previous theoretical models [159, 2, 48, 89]. The discrepancy of Ajayi's second-order theory predicting drop deformation more inaccurately than Taylor's first-order theory in the case of oblate drops was resolved by including charge convection in the theoretical model. Retention of transient charge relaxation and shape deformation was also shown to be critical in order to accurately capture the transient non-monotonic drop deformation, as we validated by comparison with both numerical simulations and existing experimental data.

While our second-order theory showed good agreement with simulations and experiments, departures become significant with increasing electric field strength as deformations become larger. While possible in principle, extending the theory to include higher-order corrections in Ca_E is exceedingly difficult due to the non-linearities in the governing equations. The problem of capturing large deformations in a theoretical model would likely be better addressed using spheroidal coordinates as in the previous work of Zhang *et al.* [179], though this method has yet to be adapted to include charge convection. One should also note that the present study is limited to axisymmetric drop deformations. In strong electric fields, experiments have demonstrated the existence of a symmetry-breaking bifurcation leading to Quincke electrorotation [141, 142, 64], which is characterized by non-axisymmetric shapes and a primarily rotational flow. Such effects cannot be captured by the theory and simulations presented herein. From a theoretical standpoint, a fully three-dimensional

model would preclude the simple use of a Stokes streamfunction as done in §5.3.2 for the solution of the flow problem, which could instead by obtained using Lamb's general solution of the Stokes equations [82]. Such a model would also be useful for the description of pair interactions between widely separated drops using the method of reflections, in a similar manner as in the previous work of Anderson [5] for thermocapillary motion of drops, or as in our previous theory for electrohydrodynamic interactions between rigid spheres [35]; the understanding of such interactions could then pave the way for dilute suspension theories for electrohydrodynamics of multiple drops. Lastly, three-dimensional boundary element simulations would be of great use to describe large deformations and electrorotation in strong fields and are the subject of our current work.

Acknowledgements

Chapter 4 is based on material that is under review in Journal of Fluid Mechanics (2016), authored by Debasish Das and David Saintillan [37]. The dissertation author was the primary researcher and author of this paper. The authors thank Petia Vlahovska and Paul Salipante for comments and suggestions, Aditya Khair and Javier Lanauze for useful discussions and for sharing their experimental data, and Lorenzo Rossini for help with generating movies of drop dynamics. Acknowledgement is made to the Donors of the American Chemical Society Petroleum Research Fund for partial support of this research through grant 53240-ND9.

Chapter 5

Electrohydrodynamics of drops under Quincke rotation: Numerical simulations

5.1 Introduction

The subject of electrohydrodynamics of drops was introduced in chapter 4. Chapter 5 extends the numerical technique employed in the previous chapter for axisymmetric drops to drops in three dimensions for the full Melcher-Taylor leaky dielectric model. Most of the early experiments on electrohydrodynamics of drops were confined to weak electric fields [4, 167, 58]; henceforth referred to as Taylor's regime characterized by prolate or oblate shapes with circulatory toroidal flow fields. Lanauze *et al.* [90] measured the transient drop deformations in the Taylor regime accurately providing a benchmark for comparisons with simulations and theory. Recent experiments in strong fields have reported existence of a symmetry breaking bifurcation

Table 5.1: Summary of existing studies on an uncharged neutrally buoyant drop subject to uniform DC electric field. EHS/EHD - ElectrohydroStatics/Dynamics

Experimental work:
Allan & Mason [4], Torza *et al.* [162], Vizika & Saville [167];
Krause & Chandratreya [84], Ha & Yang [58, 59], Sato *et al.* [144];
Salipante & Vlahovska [141, 142], Karyappa *et al.* [79], Lanauze *et al.* [90].

Theoretical modelling (EHS):
O'Konski & Thacher [108], Harris & O'Konski [62];
Allan & Mason [4], Taylor [158].

Numerical simulation (EHS):
Brazier-Smith [19], Brazier-Smith *et al.* [20], Miksis [104];
Haywood *et al.* [63], Dubash & Mestel [44, 45].

Theoretical modelling (EHD):
Taylor [159], Torza *et al.* [162], Ajayi [2], Esmaeeli & Sharifi [48];
Zhang *et al.* [179], Lanauze *et al.* [89], He *et al.* [64], Yariv & Frankel [176];
Das & Saintillan [37].

Numerical simulation (EHD):
Sherwood [151], Feng & Scott [50], Baygents *et al.* [10], Feng [49];
Hirata *et al.* [65], Lac & Homsy [88], Supeene *et al.* [156], Bjorklund [16];
López-Herrera *et al.* [100], Karyappa *et al.* [79], Hu *et al.* [68], Lanauze *et al.* [90].

Reviews:
Melcher & Taylor [103], Saville [145].

leading to spontaneous electrorotation of drops less conductive than the suspending fluid [84, 59, 144, 141]; henceforth referred to as Quincke regime [130], characterized by titled drop configurations with rotational flow fields.

While there have been numerous numerical studies investigating drop dynamics in Taylor regime, no simulations exist for drops in the Quincke regime to the best of the authors' knowledge. Brazier-Smith [19], Brazier-Smith *et al.* [20] and Miksis [104] used boundary element method to solve electrohydrostatics of drop wherein the shape of the drop is evolved as necessary to balance the normal stresses on the interface. In a more

comprehensive work, Sherwood [151] solved the coupled electrohydrodynamic problem assuming creeping flow conditions that allowed him to use boundary element method for both the electric and flow problem. His pioneering work was extended by Baygents *et al.* [10] to study axisymmetric drop pair interactions and Lac & Homsy [88] to investigate a much wider range of electric and fluid parameters. Very recently, Lanauze *et al.* [90] extended these previous work by formulating a boundary element method for the complete Melcher-Taylor leaky dielectric model. Other methods based on finite elements [50, 49, 65, 156], level-sets [16], immersed boundary [68] and finite volumes [100] have also been employed to investigate drop dynamics in the Taylor regime. All these previous work have neglected charge convection or restricted the simulations to axisymmetric drops. The latter assumption is justifiable in Taylor regime since the drop assumes an axisymmetric shape at all times. A notable exception is the work of López-Herrera *et al.* [100], however, they did not investigate drop dynamics in the Quincke regime. A closely related problem of EHD tip streaming was analysed using finite element method to solve the full Melcher-Taylor leaky dielectric model [28]. Table 5.1 summarizes the existing experimental, theoretical and numerical work on subject of electrohydrodynamics of drops.

The novelty of our work lies in the formulation of a boundary element method in three-dimensions for electrohydrodynamics of drop using the complete Melcher-Taylor leaky dielectric model that enables us to investigate Quincke regime as well. Our numerical method shows excellent agreement with existing experimental data and small deformation theories. We define the problem and present the governing equations in section §5.2. Details of the boundary integral formulation for the electric and flow problem and their numerical implementation are described in §5.3. Results

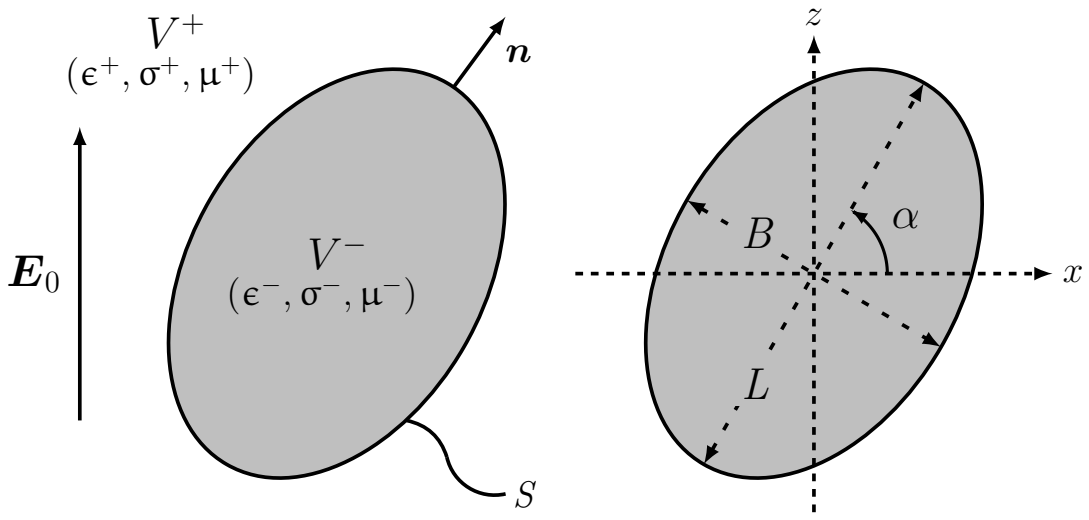

Figure 5.1: Problem definition: A liquid droplet with surface S and outward pointing unit normal $\boldsymbol{n}$ in an unbounded domain is placed in a uniform electric field $\boldsymbol{E}_0$ pointing in the vertical direction. (a) $V^{\pm}$ denote the exterior and interior domains, and $(\epsilon^{\pm}, \sigma^{\pm}, \mu^{\pm})$ are the corresponding permittivity, conductivity and dynamic viscosity, (b) the drop's major and minor axis length are denoted by L and B and the major axis is tilted at an angle α with the horizontal direction.

of the boundary element method and comparisons with experiments and theory are discussed in §5.4. We conclude and discuss possible extensions of our work in §5.5. Details of the boundary element method like surface parametrisation, regularisation of singular integrals and Wielandt's deflation technique for the flow problem are provided in the appendix.

5.2 Problem definition

5.2.1 Governing equations

We consider an uncharged neutrally buoyant liquid droplet with undeformed radius a occupying volume V^- in an infinite fluid medium V^+ and subject to a uniform

electric field $\boldsymbol{E}_0$ as depicted in figure 5.1. The drop surface is denoted as S and has an outward unit normal $\boldsymbol{n}$. Let $(\epsilon^{\pm}, \sigma^{\pm}, \mu^{\pm})$ be the permittivity, conductivity, and dynamic viscosity of the fluid and drop phase, respectively. In the Melcher-Taylor leaky dielectric model [103], all charges in the system are concentrated on the drop surface, so that the electric potential in both fluid domains is harmonic:

$$\nabla^2 \varphi^{\pm}(\boldsymbol{x}) = 0 \quad \text{for } \boldsymbol{x} \in V^{\pm}. \tag{5.1}$$

On the drop surface, the electric potential is continuous, as is the tangential component of the electric field:

$$\varphi^{+}(\boldsymbol{x}) = \varphi^{-}(\boldsymbol{x}) \quad \text{and} \quad \boldsymbol{E}_t^{+}(\boldsymbol{x}) = \boldsymbol{E}_t^{-}(\boldsymbol{x}), \quad \text{for } \boldsymbol{x} \in S, \tag{5.2}$$

where $\boldsymbol{E}_t^{\pm} = (\boldsymbol{I} - \boldsymbol{nn}) \cdot \boldsymbol{E}^{\pm}$ and $\boldsymbol{E}^{\pm} = -\boldsymbol{\nabla}\varphi^{\pm}$. The normal component of the electric field, however, undergoes a jump across the interface due to mismatch in electrical properties between the two media [91], which results in a surface charge distribution $q(\boldsymbol{x})$ related to the normal electric field by Gauss's law:

$$q(\boldsymbol{x}) = \boldsymbol{n} \cdot [\![\epsilon \boldsymbol{E}(\boldsymbol{x})]\!] = \epsilon^{+} E_n^{+}(\boldsymbol{x}) - \epsilon^{-} E_n^{-}(\boldsymbol{x}), \quad \text{for } \boldsymbol{x} \in S, \tag{5.3}$$

where $E_n^{\pm} = \boldsymbol{n} \cdot \boldsymbol{E}^{\pm}$ is the normal electric field on the interface. The charge density q evolves due to two distinct mechanisms: Ohmic currents from the bulk and advection by the fluid flow with velocity $\boldsymbol{u}(\boldsymbol{x})$ on the drop surface. Accordingly, it satisfies the

conservation equation:

$$\partial_t q + \boldsymbol{n} \cdot [\![\sigma \boldsymbol{E}]\!] + \boldsymbol{\nabla}_s \cdot (q\boldsymbol{u}) = 0, \quad \text{for } \boldsymbol{x} \in S, \tag{5.4}$$

where $\boldsymbol{\nabla}_s \equiv (\boldsymbol{I} - \boldsymbol{nn}) \cdot \boldsymbol{\nabla}$ is the surface gradient operator. On neglecting unsteady terms and surface charge convection, equation (5.4) simplifies to the boundary condition used in previous studies [151, 10, 88]:

$$\sigma^+ E_n^+ - \sigma^- E_n^- = 0, \quad \text{for } \boldsymbol{x} \in S. \tag{5.5}$$

The fluid velocity field $\boldsymbol{u}^{\pm}(\boldsymbol{x})$ and corresponding pressure field $p^{\pm}(\boldsymbol{x})$ satisfy Stokes equations in both fluid domains:

$$-\mu^{\pm} \nabla^2 \boldsymbol{u}^{\pm} + \boldsymbol{\nabla} p^{\pm} = \boldsymbol{0} \quad \text{and} \quad \boldsymbol{\nabla} \cdot \boldsymbol{u}^{\pm} = 0, \quad \text{for } \boldsymbol{x} \in V^{\pm}. \tag{5.6}$$

The velocity is continuous on the drop surface providing the kinematic boundary condition:

$$\partial_t \boldsymbol{x} = \boldsymbol{u}^+ = \boldsymbol{u}^-, \quad \text{for } \boldsymbol{x} \in S, \tag{5.7}$$

and in the absence of Marangoni effects the dynamic boundary condition expresses the balance of the jump in electric and hydrodynamic tractions with interfacial tension forces:

$$\Delta \boldsymbol{f}^E + \Delta \boldsymbol{f}^H = \gamma (\boldsymbol{\nabla}_s \cdot \boldsymbol{n}) \boldsymbol{n}, \quad \text{for } \boldsymbol{x} \in S. \tag{5.8}$$

Here, γ is the constant surface tension and $\boldsymbol{\nabla}_s \cdot \boldsymbol{n} = 2\kappa_m$ is twice the mean surface curvature. The jumps in tractions are expressed in terms of the Maxwell stress tensor

$\boldsymbol{T}^E$ and hydrodynamic stress tensor $\boldsymbol{T}^H$ as

$$\Delta \boldsymbol{f}^E = \boldsymbol{n} \cdot [\![\boldsymbol{T}^E]\!] = \boldsymbol{n} \cdot [\![\epsilon(\boldsymbol{E}\boldsymbol{E} - \tfrac{1}{2}E^2 \boldsymbol{I})]\!], \tag{5.9}$$

$$\Delta \boldsymbol{f}^H = \boldsymbol{n} \cdot [\![\boldsymbol{T}^H]\!] = \boldsymbol{n} \cdot [\![-p^H \boldsymbol{I} + \mu \left(\boldsymbol{\nabla u} + \boldsymbol{\nabla u}^T \right)]\!]. \tag{5.10}$$

The jump in electric tractions can be further simplified as

$$\begin{aligned} \Delta \boldsymbol{f}^E &= [\epsilon^+ E_n^+ - \epsilon^- E_n^-] \boldsymbol{E}_t + \tfrac{1}{2}[\epsilon^+ (E_n^{2+} - E_t^2) - \epsilon^- (E_n^{2-} - E_t^2)] \boldsymbol{n} \\ &= q \boldsymbol{E}_t + [\![p^E]\!] \boldsymbol{n}. \end{aligned} \tag{5.11}$$

The first term on the right hand side captures the tangential electric force on the interface arising from the action of the tangential field on the interfacial charge distribution. The second term captures normal electric stresses and can be interpreted as an electric pressure jump [88].

5.2.2 Non-dimensionalization

Non-dimensionalization of the governing equations yields five dimensionless groups, three of which are ratios of material properties typically defined as:

$$R = \frac{\sigma^+}{\sigma^-}, \qquad Q = \frac{\epsilon^-}{\epsilon^+}, \qquad \lambda = \frac{\mu^-}{\mu^+}. \tag{5.12}$$

The low-drop-viscosity limit $\lambda \to 0$ describes a bubble, whereas $\lambda \to \infty$ describes a rigid particle. The product RQ can also be interpreted as the ratio of inner to outer

charge relaxation time.

$$RQ = \frac{\tau^-}{\tau^+} \qquad \text{where} \qquad \tau^+ = \frac{\epsilon^+}{\sigma^+}, \quad \tau^- = \frac{\epsilon^-}{\sigma^-}. \tag{5.13}$$

The Quincke regime of interest to us is such that $RQ > 1$ or $\tau^+ > \tau^-$. A possible choice for the two remaining dimensionless number consists of the electric capillary number Ca_E and electric Mason number Ma defined as

$$Ca_E = \frac{a\epsilon^+ E_0^2}{\gamma} \qquad \text{and} \qquad Ma = \frac{\mu^+}{\epsilon^+ \tau_{MW} E_0^2}. \tag{5.14}$$

The electric capillary number Ca_E compares the characteristic time τ_γ for a deformed drop to relax to its equilibrium shape as a result of surface tension to the electro-viscous timescale τ_{EHD} [141], where

$$\tau_\gamma = \frac{\mu^+(1+\lambda)a}{\gamma}, \qquad \tau_{EHD} = \frac{\mu^+(1+\lambda)}{\epsilon^+ E_0^2}. \tag{5.15}$$

On the other hand, the Mason number is the ratio of τ_{EHD} multiplied by a factor of $\frac{2}{1+\lambda}$ to the Maxwell-Wagner relaxation time:

$$\tau_{MW} = \frac{\epsilon^- + 2\epsilon^+}{\sigma^- + 2\sigma^+}, \tag{5.16}$$

which is the characteristic timescale for charging and polarization of the drop surface upon application of the field [35]. It is also directly related to the ratio of the electric field magnitude to the critical electric field E_c for onset of Quincke rotation of a rigid

sphere as

$$Ma = \frac{\overline{\epsilon} - \overline{\sigma}}{2}\left(\frac{E_c}{E_0}\right)^2, \tag{5.17}$$

where

$$\overline{\epsilon} = \frac{\epsilon^- - \epsilon^+}{\epsilon^- + 2\epsilon^+}, \quad \overline{\sigma} = \frac{\sigma^- - \sigma^+}{\sigma^- + 2\sigma^+}, \quad E_c = \sqrt{\frac{2\mu^+}{\epsilon^+\tau_{MW}(\overline{\epsilon} - \overline{\sigma})}}. \tag{5.18}$$

Quincke rotation therefore occurs when $Ma < \overline{\epsilon} - \overline{\sigma}$ necessitating application of strong electric fields. Additionally, the condition $\overline{\epsilon} > \overline{\sigma}$ or equivalently, $RQ > 1$ needs to be satisfied for existence of real values of the critical electric field for a given drop-fluid system, indicating that the drop should be less conducting than the suspending fluid. There is also a direct correspondence between Ma and the electric Reynolds number Re_E defined by other authors [90, 147] as

$$Ma = \frac{\tau^+/\tau_{MW}}{Re_E} \qquad \text{where} \qquad Re_E = \frac{\epsilon^{2+}E_0^2}{\sigma^+\mu^+}. \tag{5.19}$$

Finally, an additional dimensionless group can be constructed by taking the ratio of the capillary time and Maxwell-Wagner relaxation time, and is independent of field strength [141]:

$$Ca_{MW} = \frac{\tau_\gamma}{\tau_{MW}} = \frac{\mu^+(1+\lambda)a}{\gamma\tau_{MW}} = (1+\lambda)Ca_E Ma. \tag{5.20}$$

For a fixed set of material properties, varying Ca_{MW} is equivalent to varying drop size a. In the remainder of the paper, we exclusively use dimensionless variables by scaling lengths with a, electric fields with E_0, and times with τ_{MW}. In addition to R, Q and λ, we primarily use Ca_E and Ma as dimensionless groups, though some of results in §5.4 will also be shown in terms of E_0/E_c and Ca_{MW}.

5.3 Boundary integral formulation

5.3.1 Electric problem

The solution of Laplace's equation (5.1) is best formulated using boundary integral equations [74, 157]. In general it is possible to express the electric potential in both fluid phases either as a single layer potential representing the surface as a distribution of sources or as a double-layer potential involving a distribution of dipoles [128]. We follow previous studies in the field [151, 10, 88, 90] and elect to use the single layer potential, yielding the integral equation

$$\varphi(\boldsymbol{x}_0) = -\boldsymbol{x}_0 \cdot \boldsymbol{E}_0 + \int_S [\![E_n(\boldsymbol{x})]\!]\, \mathcal{G}(\boldsymbol{x}_0; \boldsymbol{x})\, \mathrm{d}S(\boldsymbol{x}), \quad \text{for } \boldsymbol{x}_0 \in V^{\pm}, S. \tag{5.21}$$

Here, $\boldsymbol{x}_0$ is the evaluation point for the potential and can be anywhere in space, whereas $\boldsymbol{x}$ denotes the integration point which is located on the drop surface. The Green's function or fundamental solution of Laplace's equation in an infinite domain is given by

$$\mathcal{G}(\boldsymbol{x}_0; \boldsymbol{x}) = \frac{1}{4\pi r} \quad \text{where} \quad r = |\boldsymbol{x}_0 - \boldsymbol{x}|. \tag{5.22}$$

Note that equation (5.21) is valid in both fluid phases as well as on the interface since the Green's function is continuous across S. The equation is weakly singular, however, when $\boldsymbol{x} = \boldsymbol{x}_0$, though the singularity can be removed analytically by introducing plane polar coordinates in the parametric plane defining the local surface [128]. Knowledge of the single-layer potential density $[\![E_n(\boldsymbol{x})]\!]$ on the interface therefore allows one to determine the electric potential anywhere in space by simple integration, which prompts us to seek an equation for $[\![E_n(\boldsymbol{x})]\!]$ in terms of the surface charge density q.

We first take the gradient of equation (5.21) to obtain an integral equation for the electric field in the fluid:

$$\boldsymbol{E}^{\pm}(\boldsymbol{x}_0) = \boldsymbol{E}_0 - \int_S [\![E_n(\boldsymbol{x})]\!] \boldsymbol{\nabla}_0 \mathcal{G}(\boldsymbol{x}_0; \boldsymbol{x}) \, \mathrm{d}S(\boldsymbol{x}), \quad \text{for } \boldsymbol{x}_0 \in V^{\pm}. \tag{5.23}$$

The derivative of the Green's function undergoes a discontinuity at the interface, which needs to be accounted for when the evaluation point is on the boundary [129]:

$$\boldsymbol{E}^{\pm}(\boldsymbol{x}_0) = \boldsymbol{E}_0 - \int_S [\![E_n(\boldsymbol{x})]\!] \boldsymbol{\nabla}_0 \mathcal{G}(\boldsymbol{x}_0; \boldsymbol{x}) \, \mathrm{d}S(\boldsymbol{x}) \pm \tfrac{1}{2} [\![E_n(\boldsymbol{x}_0)]\!] \boldsymbol{n}(\boldsymbol{x}_0), \quad \text{for } \boldsymbol{x}_0 \in S. \tag{5.24}$$

The integral equation for the electric field is strongly singular. However, taking dot product of equation (5.24) with the unit normal vector $\boldsymbol{n}(\boldsymbol{x}_0)$ reduces the singularity by an order. We then add the normal components of electric field outside and inside to obtain their average:

$$\frac{E_n^+(\boldsymbol{x}_0) + E_n^-(\boldsymbol{x}_0)}{2} = E_{n0} - \int_S [\![E_n(\boldsymbol{x})]\!] [\boldsymbol{n}(\boldsymbol{x}_0) \cdot \boldsymbol{\nabla}_0 \mathcal{G}(\boldsymbol{x}_0; \boldsymbol{x})] \, \mathrm{d}S(\boldsymbol{x}), \quad \text{for } \boldsymbol{x}_0 \in S. \tag{5.25}$$

The weak singularity in integral equation (5.25) can be removed by subtracting $[\![E_n(\boldsymbol{x}_0)]\!]$ from its kernel to obtain the regular integral [149]:

$$\begin{aligned} &\frac{E_n^+(\boldsymbol{x}_0) + E_n^-(\boldsymbol{x}_0)}{2} + [\![E_n(\boldsymbol{x}_0)]\!] L_n(\boldsymbol{x}_0) \\ &= E_{n0} - \int_S \{[\![E_n(\boldsymbol{x})]\!] - [\![E_n(\boldsymbol{x}_0)]\!]\} \{\boldsymbol{n}(\boldsymbol{x}_0) \cdot \boldsymbol{\nabla}_0 \mathcal{G}(\boldsymbol{x}_0; \boldsymbol{x})\} \, \mathrm{d}S(\boldsymbol{x}), \quad \text{for } \boldsymbol{x}_0 \in S, \end{aligned} \tag{5.26}$$

where $L_n = \boldsymbol{n} \cdot \boldsymbol{L}$ is an integral equation containing geometrical quantities whose exact form is given in the appendix. Using Gauss's law, we can eliminate E_n^+ and E_n^-

to obtain the desired regular integral equation for $[\![E_n]\!]$:

$$[\![E_n(\boldsymbol{x}_0)]\!]\left(L_n(\boldsymbol{x}_0)-\frac{1+Q}{2(1-Q)}\right)+\int_S\{[\![E_n(\boldsymbol{x})]\!]-[\![E_n(\boldsymbol{x}_0)]\!]\}\{\boldsymbol{n}(\boldsymbol{x}_0)\cdot\boldsymbol{\nabla}_0\mathcal{G}(\boldsymbol{x}_0;\boldsymbol{x})\}\,\mathrm{d}S(\boldsymbol{x})$$
$$=E_{n0}-\frac{q(\boldsymbol{x}_0)}{1-Q},\quad \text{for } \boldsymbol{x}_0\in S. \tag{5.27}$$

The jump in normal component of the electric field can be computed from (5.27) for a given surface charge distribution numerically by solving a linear system using a standard iterative solver GMRES [136]. The first term in the right hand side is the forcing term arising from the applied electric field. Knowledge of $[\![E_n]\!]$ and application of Gauss's law, provides the values of E_n^+ and E_n^-:

$$E_n^+=\frac{q-Q[\![E_n]\!]}{1-Q},\qquad E_n^-=\frac{q-[\![E_n]\!]}{1-Q}. \tag{5.28a,b}$$

The tangential component of the electric field can be evaluated using (5.24) directly, however, care must be taken to remove the strong singularity in the kernel [149]. Here, we adopt an indirect method that requires computation of the electric potential φ using equation (5.21) and differentiating it numerically along the surface to obtain $\boldsymbol{E}_t$, see appendix for details. Once the normal and tangential components of the electric field are known, we can determine the jump in normal component of Ohmic current $[\![\sigma E_n]\!]$ and electric traction $\Delta\boldsymbol{f}^E$ using equation (5.11).

5.3.2 Flow problem

The applied electric field induces fluid motion inside and outside the drop. The need to solve the flow problem are twofold; determination of the interfacial fluid

velocity for solving the charge conservation equation (5.4) and advection of the drop's shape to satisfy the kinematic boundary condition (5.7). The flow problem is solved after application of the dynamic boundary condition (5.8) to obtain the hydrodynamic traction $\Delta \boldsymbol{f}^H$ on the drop-fluid interface. Assuming creeping flow, we use Stokes' boundary integral equation to determine fluid velocity in the domain [132, 128].

$$\begin{aligned} \boldsymbol{u}(\boldsymbol{x}_0) = &- \frac{1}{4\pi\mu(1+\lambda)} \int_S \Delta \boldsymbol{f}^H(\boldsymbol{x}) \cdot \boldsymbol{G}(\boldsymbol{x}_0;\boldsymbol{x}) \, \mathrm{d}S(\boldsymbol{x}) \\ &+ \frac{\kappa}{4\pi} \int_S \boldsymbol{u}(\boldsymbol{x}) \cdot \boldsymbol{T}(\boldsymbol{x}_0;\boldsymbol{x}) \cdot \boldsymbol{n}(\boldsymbol{x}) \, \mathrm{d}S(\boldsymbol{x}), \quad \text{for } \boldsymbol{x}_0 \in V^{\pm}, S, \end{aligned} \tag{5.29}$$

$$\text{where,} \qquad \boldsymbol{G} = \frac{\boldsymbol{I}}{r} + \frac{\boldsymbol{rr}}{r^3}, \qquad \boldsymbol{T} = 6\frac{\boldsymbol{rrr}}{r^5}, \tag{5.30a, b}$$

are the Stokeslet and stresslet respectively and $\kappa = (1-\lambda)/(1+\lambda)$. The usual negative sign in the stresslet term appears if $\boldsymbol{r}$ is defined as $|\boldsymbol{x} - \boldsymbol{x}_0|$. Note that $\kappa = \pm 1$ corresponds to the case of a bubble ($\lambda \to 0$) and solid ($\lambda \to \infty$) respectively. The interfacial velocity appearing in the double layer potential is yet unknown and an integral equation for the same can be obtained by moving the evaluation point $\boldsymbol{x}_0$ to the boundary S. In dimensionless form it reads:

$$\begin{aligned} \boldsymbol{u}(\boldsymbol{x}_0) + &\frac{\lambda - 1}{8\pi} \int_S \{\boldsymbol{u}(\boldsymbol{x}) - \boldsymbol{u}(\boldsymbol{x}_0)\} \cdot \boldsymbol{T}(\boldsymbol{x}_0;\boldsymbol{x}) \cdot \boldsymbol{n}(\boldsymbol{x}) \, \mathrm{d}S(\boldsymbol{x}) \\ &= - \frac{1}{8\pi Ma} \int_S \Delta \boldsymbol{f}^H(\boldsymbol{x}) \cdot \boldsymbol{G}(\boldsymbol{x}_0;\boldsymbol{x}) \, \mathrm{d}S(\boldsymbol{x}), \quad \text{for } \boldsymbol{x}_0 \in S. \end{aligned} \tag{5.31}$$

The forcing term in this equation is contained in the hydrodynamic traction $\Delta \boldsymbol{f}^H$. The above equation forms a linear system $\boldsymbol{A} \cdot \boldsymbol{u} = \boldsymbol{b}$ that is solved numerically using GMRES. The weak singularity appearing in the double layer potential in the original equation (5.29) has been removed by using appropriate integral identities (5.31). The

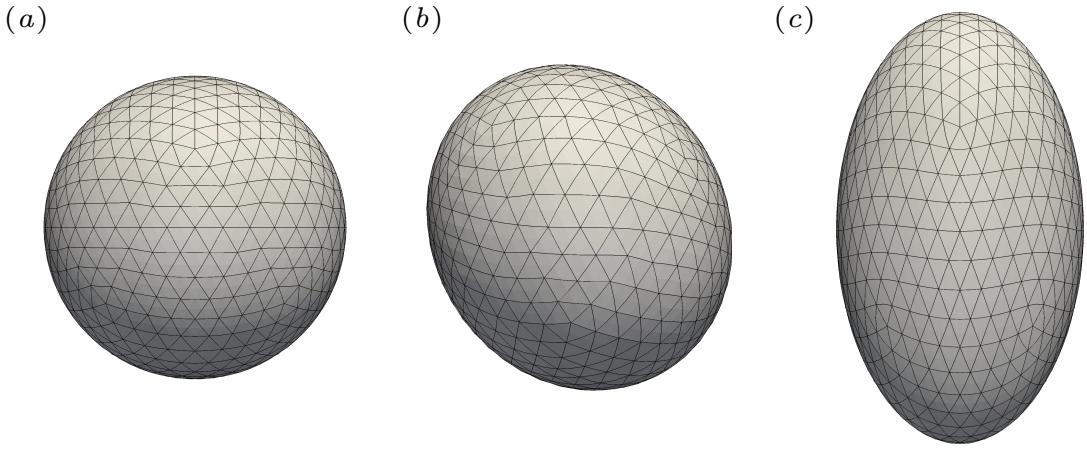

Figure 5.2: Discretized mesh: $N_{\triangle} = 1280$ curved elements with 6 nodes (a) An initially spherical mesh at time $t = 0$, (b) a deformed mesh of a tilted drop in Quincke regime corresponding to the case of figures 5.7c and 5.7f, (c) a deformed mesh of a prolate drop in Taylor regime, with mesh relaxation algorithm of Loewenberg & Hinch [99], corresponding to the steady state of system 3.

weak singularity appearing in the single layer potential disappears after introducing plane polar coordinates [127]. It is well known that the integral equation (5.31) admits arbitrary rigid body motion and uniform expansion eigensolutions that results in the matrix $\boldsymbol{A}$ becoming ill-conditioned for $\lambda \gg 1$ or $\lambda \ll 1$ leading to poor convergence of the solution [181]. We employ Wielandt's deflation technique to eliminate $\kappa = \pm 1$ from the spectrum of the integral equation to cure the ill-conditioning [82], see appendix for details. Once the interfacial velocity is known, the nodes are advected in the normal direction of the fluid flow and tangential direction with a heuristic mesh relaxation velocity $\boldsymbol{u}_m$ for a uniform spacial node distribution [99].

5.3.3 Numerical implementation

We solve the integral equations (5.21), (5.27) and (5.31) numerically using boundary element method on the discretized drop's surface [128]. The main advantages

of using boundary element method are accuracy and decreased computational time as the solution space is one degree lower than the physical space. In all the simulations, we consider an initially spherical uncharged drop. The initial drop's surface is generated from an icosahedron by successive subdivision of the 20 original triangular elements into four new elements by projecting the new nodes onto the sphere. The discretized surface comprises of 6 nodes curved elements that allows for computation of curvature. While most of our results in the present work are on a surface with $N_\triangle = 320$ elements and 642 nodes obtained after two successive subdivisions $N_d = 2$, we present a few results with $N_\triangle = 1280$ elements and 2562 nodes after $N_d = 3$ subdivisions. The computation of geometrical properties of the discretized surface like normal vector and curvature are outlined in the appendix. The charge conservation equation (5.4) and surface nodes are advanced in time using finite differences and an explicit second order Runge-Kutte scheme with the initial condition $q(t = 0) = 0$.

$$\partial_t q = \frac{Q+2}{1+2R}(E_n^- - RE_n^+) - \boldsymbol{\nabla}_s \cdot (q\boldsymbol{u}) + \boldsymbol{u}_m \cdot \boldsymbol{\nabla}_s q, \tag{5.32}$$

$$\partial_t \boldsymbol{x} = \boldsymbol{n} \cdot \boldsymbol{u} + \boldsymbol{u}_m \tag{5.33}$$

We implemented a finite volume [177] and a semi-implicit scheme for the charge conservation equation wherein the linear $[\![\sigma E_n]\!]$ and nonlinear $\boldsymbol{\nabla}_s \cdot (q\boldsymbol{u})$ terms are treated implicitly and explicitly respectively. These alternative methods did not produce significant differences in the results when compared to the second order Runge-Kutte method. As a validation of the numerical implementation of the electric problem, we solved electrohydrodynamics of a solid spherical particle under Quincke rotation for easy comparison with analytical solutions based on spherical harmonic

Table 5.2: Material properties: systems 1 and 2 correspond to the experiments of Lanauze *et al.* [90] and Salipante & Vlahovska [141], respectively. $\epsilon_0 = 8.8542 \times 10^{-12}\,\mathrm{F.m^{-1}}$ denotes the permittivity of vacuum.

System	ϵ/ϵ_0	$\bar{\epsilon}/\epsilon_0$	σ (S.m^{-1})	$\bar{\sigma}$ (S.m^{-1})	μ (Pa.s)	$\bar{\mu}$ (Pa.s)	γ (mN.m^{-1})
1a	4.9	2.8	5.8×10^{-11}	0.2×10^{-11}	0.68	0.05	4.5
1b	4.9	2.8	5.8×10^{-11}	0.2×10^{-11}	0.68	0.05	4.5
1c	4.9	2.8	5.8×10^{-11}	0.2×10^{-11}	0.68	0.05	4.5
2a	5.3	3.0	4.5×10^{-11}	0.12×10^{-11}	0.69	0.97	4.5
2b	5.3	3.0	4.5×10^{-11}	0.12×10^{-11}	0.69	0.97	4.5

expansions [35]. We also tested our numerical method for hydrodynamics of drops in simple shear flow [81] and electrohydrodynamics of drops without convection [88].

5.4 Results and discussion

For measuring the drop's deviation from sphericity, we use Taylor's deformation parameter $\mathcal{D}$, defined as

$$\mathcal{D} = \frac{L - B}{L + B}, \tag{5.34}$$

where L and B denote the length of the axis of the drop parallel and perpendicular to the electric field respectively in the Taylor regime. The sign of $\mathcal{D}$ distinguishes between oblate ($\mathcal{D} < 0$) and prolate ($\mathcal{D} > 0$) shapes. In the Quincke regime, L and B denote the length of the major and minor axis of the drop respectively, resulting in $\mathcal{D} > 0$ at all times. The tilt angle of drops is measured with angle α, see figure 5.1. In order to find these geometric quantities, the drop's surface is fitted to an ellipsoid using least squares method.

Table 5.3: Material properties: systems 1 and 2 with drop radius and electric field strength.

System	a (mm)	E_0 (kV.cm^{-1})
1a	2.0	1.6
1b	2.0	2.1
1c	2.0	6.1
2a	0.7	0.45–2.0
2b	2.1	0.26–1.2

5.4.1 Taylor regime

We first investigate drop dynamics in the Taylor regime, where the drops attain either a steady oblate or prolate shape. We compare our three dimensional boundary element method with existing experiments, small deformation theories and an axisymmetric boundary element method developed in our previous work [37]. The material properties are chosen from experiments of Lanauze *et al.* [90] for transient (system 1) and Salipante & Vlahovska [141] for steady drop deformations (system 2), see table 5.2. The corresponding dimensionless parameters are presented in table 5.4. Since both these experiments focused on oblate drops, we choose one set of parameters from the prolate drop experiments of Ha & Yang [58] (system 3). As they did not report all the material properties necessary to construct all the 5 dimensional groups; we set $Ca_E = 0.3$ and $Ma = 0.5$.

Figure 5.3a shows the transient deformation of oblate drops for system 1a for an electric field strength of $E/E_c = 0.49$. The axisymmetric boundary element method performs the best in predicting drop deformation when compared with experiments. We calculate drop deformations obtained using the three dimensional boundary element method for two different mesh sizes as a convergence test; $N_d = 2$ and $N_d = 3$. The

Table 5.4: Dimensionless parameters corresponding to the material properties of table 5.1: systems 1, 2 and 3 correspond to the experiments of Lanauze *et al.* [90], Salipante & Vlahovska [141] and Ha & Yang [58], respectively.

System	R	Q	λ	Ca_E	Ma
1a	29.0	0.57	0.074	0.49	0.65
1b	29.0	0.57	0.074	0.85	0.375
1c	29.0	0.57	0.074	7.18	0.045
2a	36.6	0.57	1.41	0.03–0.6	0.27–5.4
2b	36.6	0.57	1.41	0.03–0.6	0.8–16
3	0.1	1.37	1	0.3	0.5

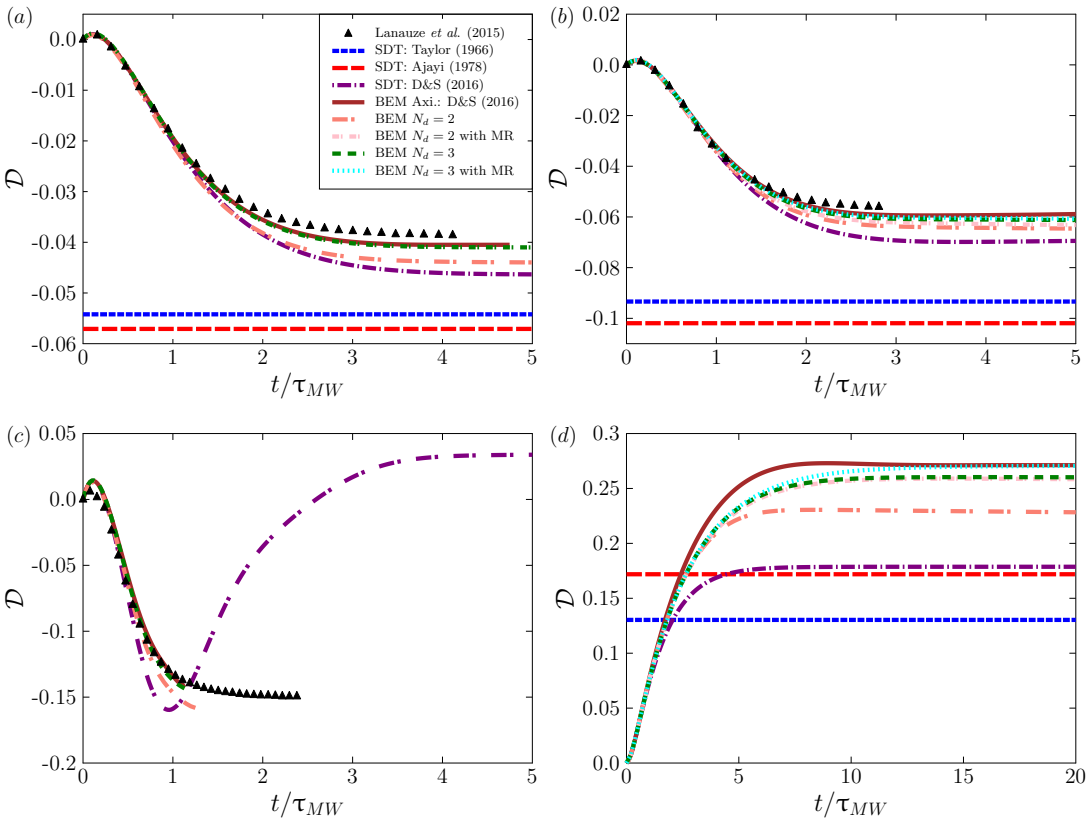

Figure 5.3: Deformation parameter $\mathcal{D}$ as a function of time for the parameters of: a) system 1a, b) system 1b, c) system 1c, the steady deformation values predicted by the models of Taylor (1966) and Ajayi (1978) are -0.75 and -1.40, respectively, and out of the frame of figure and d) system 3. The effect of mesh relaxation algorithm on drop deformation measurement is seen to be more profound for larger deformation as in system 3 when compared to system 1b.

results from the finer mesh converges to that of the axisymmetric boundary element method. The small deformation theories [159, 2] do not perform as well as the full numerical simulations, however, inclusion of charge convection in the theoretical model improves the results considerably [37].

Next, we consider system 1b, to investigate the effect of increasing the electric field to $E/E_c = 0.64$ that correspondingly results in an increase in drop deformations. The axisymmetric and three dimensional boundary element method with $N_d = 3$ again find excellent agreement with the experimental data. The interfacial charge and velocity profile for the three dimensional simulation is shown in figure 5.4. These time series profiles reveal that as the interfacial velocity strength increases, negative and positive charges are advected towards the equatorial circumference of the drop, thereby creating a sharp charge gradient across it. We also consider the effect of the mesh relaxation algorithm of Loewenberg & Hinch [99] and find that it improves the predictions by a small fraction. The deviations of the coarser mesh $N_d = 2$ from the experimental results are small and improve slightly on including mesh relaxation. We again find that the small deformation theory with convection matches the simulations and experiments better than that without convection.

Considering system 1c, with an even higher electric field $E/E_c = 1.86$, we find the charge gradient across the drop's equator becomes sharper and an actual discontinuity appears that triggers instabilities, reminiscent of Gibb's phenomena, leading to the termination of the simulations. Lanauze *et al.* [90] had discovered this charge shock in their simulations and attributed it to three dimensional flows (referring to Quincke electrorotation) that an axisymmetric boundary integral formulation cannot capture. However, our three dimensional simulations do not show any rotational flow

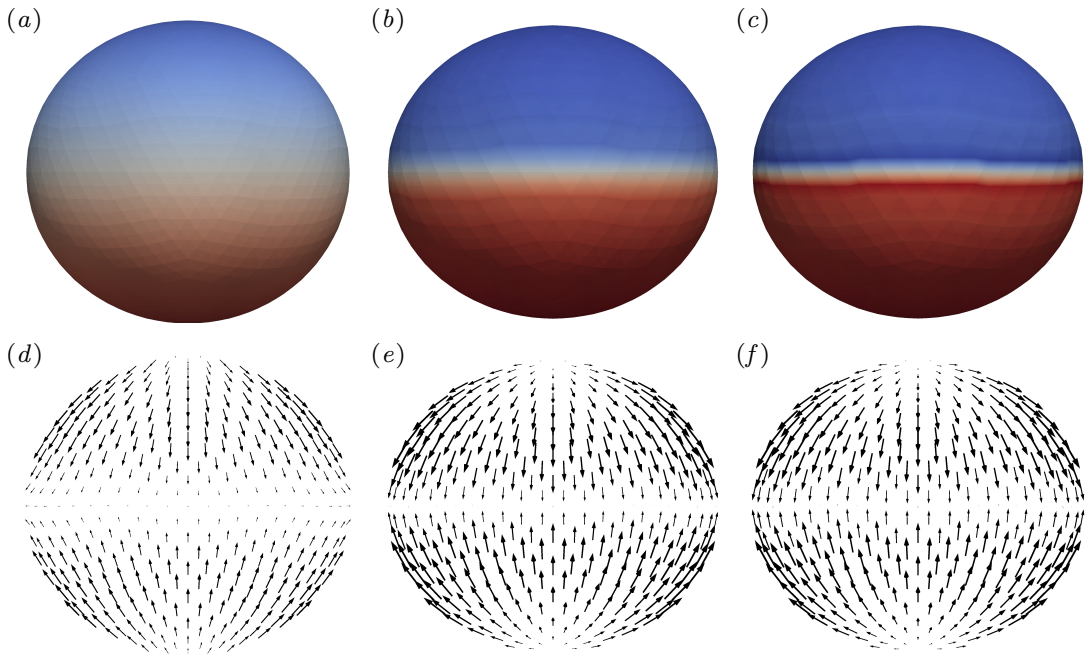

Figure 5.4: Time evolution profiles of interfacial charge and velocity for system 1b in the Taylor regime at $t/\tau_{MW} = 1.0, 2.5, 4.0$.

at this electric field strength that could prevent the formation of this charge shock. This shows that charge shock can exist in the Taylor regime as well. The charge shock is solely due to the straining flow that causes accumulation of positive and negative charges at the equator. The strength of this straining flow increases with electric field and is more pronounced for low viscosity drops. Taylor's and Ajayi's drop deformation predictions are out of the frame for this case. Inclusion of charge convection in the small deformation theory appears to help the situation, however, the sharp charge discontinuity is still unable to be captured.

We also consider a prolate drop case, system 3, that undergoes larger deformations than the oblate cases. The steady state deformation value reported in experiments of Ha & Yang [58] with unknown Ma is $\mathcal{D} = 0.25$, simulation of Lac & Homsy [88] with $Ma \to \infty$ is $\mathcal{D} = 0.22$, and our simulations with $Ma = 0.5$ is

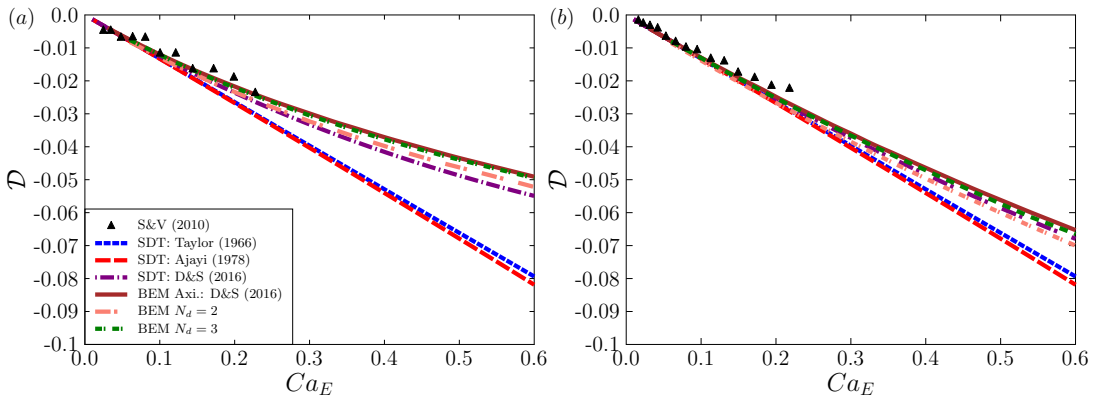

Figure 5.5: Steady drop deformation $\mathcal{D}$ as a function of electric capillary number Ca_E for the parameters of: (a) system 2a, and (b) system 2b. The various theoretical models and simulations are compared to the experimental measurements of Salipante & Vlahovska [141].

$\mathcal{D} = 0.27$, see figure 5.3d. Since there are no experimental data for transient drop deformations we will consider the axisymmetric simulations as the benchmark for convergence test. We find that the three dimensional simulations with $N_d = 3$ and mesh relaxation converges to the results of the axisymmetric simulation, however, with a small discrepancy in the transient state. Simulations with $N_d = 2$ and mesh relaxation perform as good as $N_d = 3$ without mesh relaxation. These results signifies the importance of including mesh relaxation in simulations with larger drop deformations. Unsurprisingly, the large drop deformation is poorly captured and underpredicted by the small deformation theories.

We now consider steady state drops deformations, system 2, and compare our simulations with theoretical and experimental data. We consider drop deformations for two drop sizes; system 2a with $a = 0.7$mm and $a = 2.1$mm for increasing values of electric capillary number Ca_E. For a given value of electric capillary number, the smaller drop experiences a stronger electric field corresponding to a lower Mason number Ma, when compared to the larger drop. As a consequence, for a fixed Ca_E value

the smaller drop experiences stronger charge convection on its surface, resulting in less oblate shape, see figure 5.5a. The larger drop, on the other hand, experiences weaker charge convection and consequently deforms more, see figure 5.5b. In consistence with previous results, the axisymmetric and three dimensional simulations perform the best in predicting drop deformations. The small deformation theory with convection performs the best out of all the theories. Since the effect of charge convection is weaker in the case of the larger drop, the small deformation theories without convection do not deviate significantly from the simulation, experiments and theory with convection.

5.4.2 Quincke regime

We now turn our attention to electrorotation of drops in the Quincke regime. We use the drop-fluid system from the experiments of Salipante & Vlahovska [141] but only consider smaller drop sizes. We consider three systems with different viscosity ratios; system 2c with $\lambda = 14.1$, 2d with $\lambda = 7.05$, 2e and 2f with $\lambda = 1.4$. Note that system 2e and 2f are the same as 2b, however, with different drop sizes and stronger electric fields. The heuristic mesh relaxation algorithm of Loewenberg & Hinch [99] is not included in the simulations in the Quincke regime as we found it to cause numerical instabilities preventing the simulations to reach a steady state. This is not a problem since we do not expect mesh relaxation to considerably alter the results since the drop deformations considered here are moderate $\mathcal{D} \leqslant 0.1$. For comparisons with the drop tilt angle α, we define β as the angle between the induced dipole moment and the direction antiparallel to the electric field following the notation

Table 5.5: Material properties: system 2 corresponding to the experiments of Salipante & Vlahovska [141] has a critical electric field of $E_c = 2.68$ kV.cm^{-1}. Permittivity and conductivity of this system are given in table 5.2.

System	μ (Pa.s)	$\bar{\mu}$ (Pa.s)	γ (mN.m^{-1})	a (mm)	E_0 (kV.cm^{-1})
2c	0.69	9.74	4.5	0.25, 0.75, 1.25, 1.75	0.67–5.36
2d	0.69	4.87	4.5	0.25, 0.75, 1.25, 1.75	0.67–5.36
2e	0.69	0.97	4.5	0.25	4.69–5.49
2f	0.69	0.97	4.5	0.75	4.69–6.03

Table 5.6: Dimensionless parameters corresponding to the material properties of table 5.5: system 2 corresponds to the experiments of Salipante & Vlahovska [141].

System	R	Q	λ	Ca_{MW}	E_0/E_c
2c	36.6	0.57	14.1	0.44, 1.32, 2.20, 3.08	0.25–2.0
2d	36.6	0.57	7.05	0.23, 0.69, 1.15, 1.61	0.25–2.0
2e	36.6	0.57	1.41	0.07	1.75–2.05
2f	36.6	0.57	1.41	0.21	1.75–2.25

of Salipante & Vlahovska [141],

$$\beta = \frac{\pi}{2} - \arctan\left[\left(\frac{E_0^2}{E_c^2} - 1\right)^{-1/2}\right]. \tag{5.35}$$

In order to characterise the onset of Quincke electrorotation of drops, we present a phase digram that distinguishes Taylor from the Quincke regime for systems 2c and 2d, figure 5.6. Figure 5.6a shows the transition from Taylor to Quincke regime for increasing drop sizes with correspondingly increasing Ca_{MW} for viscosity ratio $\lambda = 14.1$. We find that the applied electric field required for the onset of rotation decreases with an increase in Ca_{MW} in agreement with experimental data for the range of Ca_{MW} considered here. The physical interpretation of this observation is as follows; for a given electric field strength, a smaller drop experiences smaller deformation, due

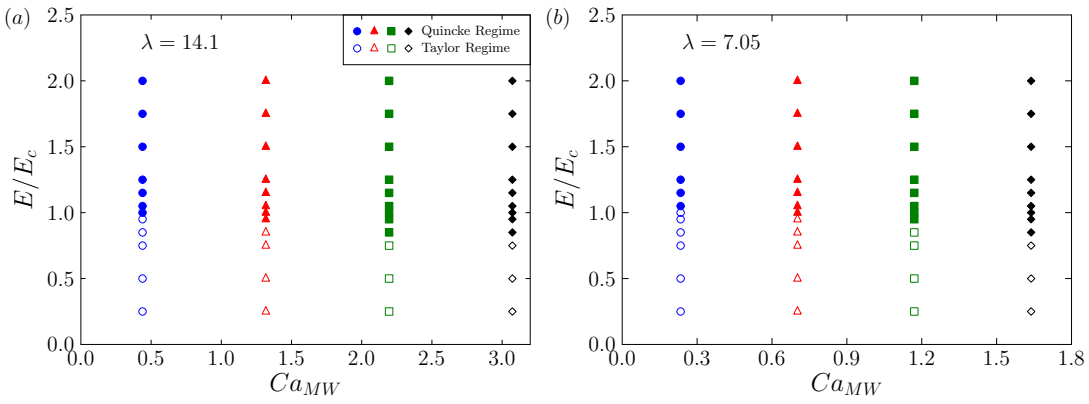

Figure 5.6: Phase diagram distinguishing Taylor (empty symbols) from Quincke regime (filled symbols) for two different viscosity ratios (a) $\lambda = 14.1$, (b) $\lambda = 7.05$.

to smaller Ca_E value, resulting in a weaker induced dipole moment $\boldsymbol{P}$ when compared to a larger drop that deforms more. As a result, the electric torque $\boldsymbol{P} \times \boldsymbol{E}_0$ required to overcome viscous torque for sustained rotation is higher for a smaller drop as compared to a larger drop. The same effect is seen in figure 5.6b with $\lambda = 7.05$. For a given electric field strength and drop radius, a drop with lower viscosity experiences stronger charge convection, resulting in a weaker induced dipole moment. Consequently, the critical electric field for the onset of Quincke electrorotation increases. Our simulations were unable to explore higher E/E_c and Ca_{MW} due to two probable reasons. Strong electric fields gives rise to strong flow velocities which leads to significant mass loss of the drop arising from discretization errors and requirement of exceedingly small time steps for advection of nodes for numerical stability. We discuss potential remedies of these problems in the conclusion section.

Figure 5.7, shows the charge and velocity evolution plots of a drop under Quincke rotation, corresponding to system 2c with an initial radius of $a = 1.25$mm and electric field $E/E_c = 1.5$. In figure 5.10, we measure the tilt angle for system 2c as a function of the applied field for three different drop sizes. We also show the

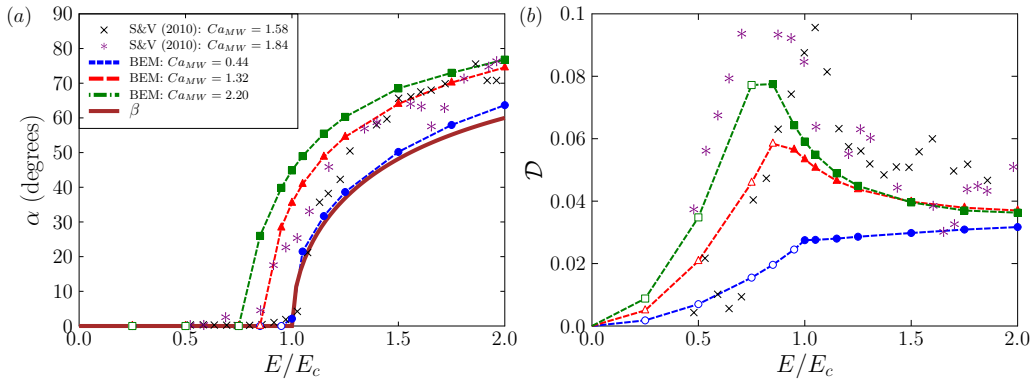

Figure 5.7: Time evolution profiles of interfacial charge and velocity for system 2c with drop radius a=1.25mm in the Quincke regime at $t/\tau_{MW} = 3.75, 5.25, 10.5$.

experimental results of Salipante & Vlahovska [141], however, with larger drop sizes for qualitative comparison. In figure 5.10a, we find that an increase in drop size shifts the supercritical pitchfork bifurcation point to the left. This effect, which is a consequence of stronger induced dipole in more deformed drops, was also found in the experiments, however to a lesser degree. We also plots the drop deformation as a function of the applied field. We find that the drop deformation increases non-monotonically in the Taylor regime till the point of transition to Quincke regime. In the Taylor regime, there is only straining flow that serves to deform the drop. Once the drop enters the Quincke regime, the rotational flow dominates over the straining flow and the drop deformation decreases. We see these same effects in a drop with lower viscosity ratio $\lambda = 7.05$ as well, however, the entire bifurcation plot is shifted to the right, see figure 5.9. This is a consequence of stronger charge convection that serves to decrease the strength of the induced dipole moment as compared to the higher viscosity drop. These results are consistent with the electrorotation theory of He *et al.* [64].

In order to quantify the straining and rotational flow in the drop, we first obtain the velocity gradient tensor by taking the gradient of the velocity field (5.29)

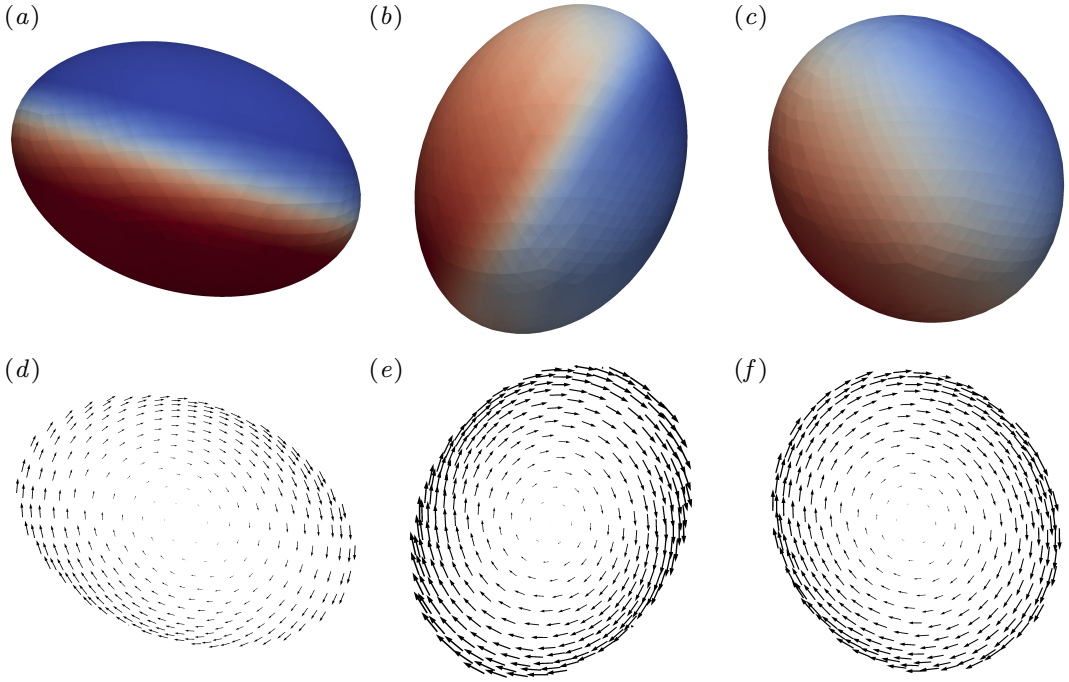

Figure 5.8: Time evolution profiles of interfacial charge and velocity for system 2c with drop radius $a = 1.25$mm in the Quincke regime at $t/\tau_{MW} = 3.75, 5.25, 10.5$

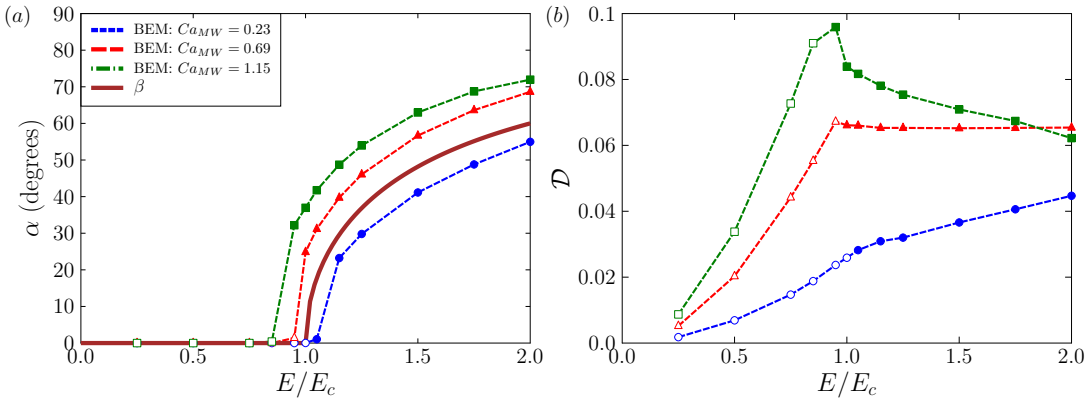

Figure 5.9: *a*) Tilt angle α and *b*) drop deformation $\mathcal{D}$ as a function of applied electric field E/E_c for system 2d for various drop sizes.

with respect to $\boldsymbol{x}_0$.

$$\begin{aligned}\boldsymbol{\nabla}_0\boldsymbol{u}(\boldsymbol{x}_0) = &-\frac{1}{4\pi\mu(1+\lambda)}\int_S \Delta\boldsymbol{f}^H(\boldsymbol{x})\cdot\boldsymbol{\nabla}_0\boldsymbol{G}(\boldsymbol{x}_0;\boldsymbol{x})\,\mathrm{d}S(\boldsymbol{x})\\ &+\frac{\kappa}{4\pi}\int_S \boldsymbol{u}(\boldsymbol{x})\cdot\boldsymbol{\nabla}_0\boldsymbol{T}(\boldsymbol{x}_0;\boldsymbol{x})\cdot\boldsymbol{n}(\boldsymbol{x})\,\mathrm{d}S(\boldsymbol{x}),\quad \text{for } \boldsymbol{x}_0\in V^{\pm},S,\end{aligned} \tag{5.36}$$

We define a parameter ζ to characterise the straining and rotation flow as,

$$\zeta = \frac{\mathrm{tr}(\boldsymbol{S}^2)-\mathrm{tr}(\boldsymbol{W}^2)}{\mathrm{tr}(\boldsymbol{S}^2)+\mathrm{tr}(\boldsymbol{W}^2)}, \tag{5.37}$$

where, $\boldsymbol{S} = \frac{1}{2}(\boldsymbol{\nabla u}+\boldsymbol{\nabla u}^T)$, $\boldsymbol{W} = \frac{1}{2}(\boldsymbol{\nabla u}-\boldsymbol{\nabla u}^T)$, (5.38$a$, b)

are the usual strain-rate and vorticity tensors. Values of ζ closer to 1 or -1 represent dominant straining or rotational flows respectively. In the Taylor regime, rotational flow is completely absent and the value of ζ is identically 1. During the transition from Taylor to Quincke regime $\zeta\in(-1,1)$ but once the drop is in the Quincke regime, the straining flow does not increase while rotational flow continues to increase with the electric field and $\zeta\to-1$. This also explains the asymptotic behaviour of drop deformation as electric field increases, see figure 5.10b and 5.9b.

We investigated a few cases for system 2e and 2f with $\lambda = 1.4$, figure 5.11. We were not able to start these simulations from a spherical uncharged drop due to the formation of charge shock. The initial condition for these cases were obtained from the steady state data of $\lambda = 7.05$. We also show the experimental data for larger drops sizes for qualitative comparison.

Finally, we show the tilt angle and deformation of the drop as a function of time, see figure 5.12. In particular, we find that stronger electric fields induce more oscillations in the drop tilt angle and deformation before they reach a steady state.

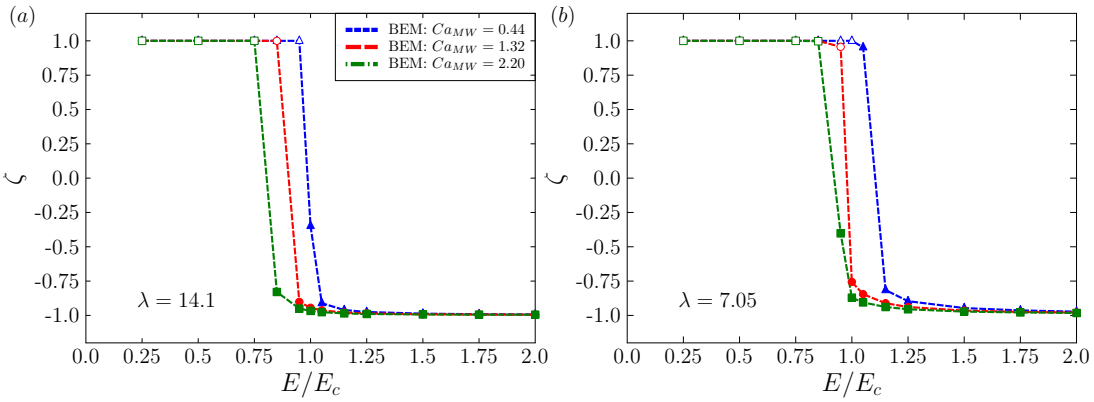

Figure 5.10: ζ calculated at the drop's center $\boldsymbol{x}_0 = \mathbf{0}$ as a function of electric field for *a*) $\lambda = 14.1$ and *b*) $\lambda = 7.05$. Values of ζ close to 1 or -1 represent dominant straining or rotational flows respectively.

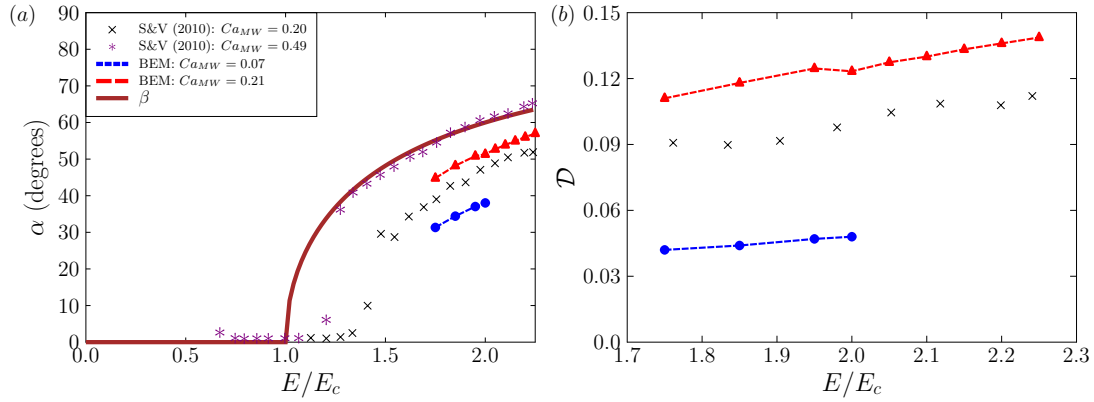

Figure 5.11: *a*) Tilt angle α and *b*) drop deformation $\mathcal{D}$ as a function of applied electric field E/E_c for system 2e and 2f. The experimental data for drop deformation corresponding to $Ca_{MW} = 0.98$ is not available.

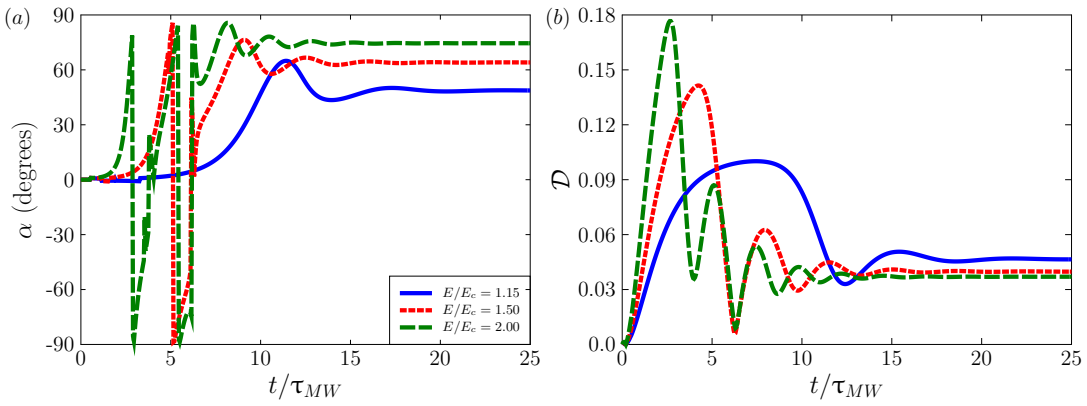

Figure 5.12: (color online) *a*) Tilt angle α and *b*) drop deformation $\mathcal{D}$ as a function of time t/τ_{MW} for system 2d with drop size a=0.75mm and $Ca_{MW} = 0.69$. Stronger electric fields cause more oscillations in the tilt angle and drop deformation.

These observations are also consistent with the theoretical results of He *et al.* [64].

5.5 Conclusion

In this work, we have developed a three dimensional boundary element method for the complete Melcher-Taylor leaky dielectric model, thereby extending the previous work in this field [151, 10, 88, 90]. Our simulations are able to predict the steady oblate and prolate drop shapes in the Taylor and tilted drops in the Quincke regime. We presented a phase diagram to show the transition from Taylor to Quincke regime. We measured the tilt angle and drop deformation in the Quincke regime as a function of electric field that agrees well with the experiments. We also characterized the nature of the flow in the drop as a function of electric field helpful in explaining the drop deformation in the two regimes.

Our simulations were restricted to relatively small to moderate drop sizes while the experiments of Salipante & Vlahovska [141] reported larger drop sizes as

well. The mass loss at stronger electric fields and larger deformations can be cured by increasing mesh discretization. However, an increase in the size of the linear system to be solved will require full parallelisation (as compared to OPENMP used in this work) for achieving convergence in reasonable computational time. A spectral boundary element method for electrohydrodynamics of drops will also be helpful for faster convergence. Being able to investigate drops in stronger electric fields will help in reproducing and understanding the chaotic drop dynamics at stronger electric fields reported in experiments [142]. The sharp charge discontinuity observed at the equatorial circumference of the drop requires a shock capturing scheme. Standard upwind schemes are non-trivial to implement on an unstructured mesh. High-order weighted essentially non-oscillatory (WENO) schemes using finite volume formulation can be employed towards this purpose [67]. Potential extensions of our work include studying sedimenting drops under electric field, the effect of surfactants on drop deformation and rotation and drop-drop interactions leading to electrohydrodynamics of emulsions that may necessitate the use of fast multipole methods [180]. Numerical simulations of electrohydrodynamics of emulsions will be helpful in understanding recent experiments that have reported collective flow pattern in these systems. Finally, a three dimensional small deformation theory for the complete Melcher-Taylor leaky dielectric model will be helpful in understanding these phenomena due to analytical tractability and is the subject of our current research.

Acknowledgements

Chapter 5 is based on material that is going to be submitted to Journal of Fluid Mechanics (2016), authored by Debasish Das and David Saintillan [36]. The

dissertation author was the primary researcher and author of this paper. The authors thank Petia Vlahovska and Paul Salipante for helpful discussions and suggestions, Aditya Khair and Javier Lanauze for useful comments and sharing their experimental data, Andrew Spann and Maxime Theillard for discussions on the implementation of the numerical scheme. Acknowledgement is made to the Donors of the American Chemical Society Petroleum Research Fund for support of this research through grant 53240-ND9.

Chapter 6

Conclusions and directions for future work

6.1 Conclusions

In this work, we addressed a number of fundamental questions concerning the electrohydrodynamics of particles and drops, many of them motivated by experiments. While most of the previous work in this field focused on the dynamics of particles and drops in weak electric fields, there are only a handful of work investigating the dynamics in strong electric fields. Of particular interest to us was the phenomena of Quincke electrorotation, where particles and drops exhibit a symmetry breaking bifurcation leading to spontaneous steady rotation in strong electric fields. This phenomena, although, discovered almost a century ago had been mostly overlooked until recently and constitutes the main theme of this work. The methods and techniques used and developed in this work are applicable to other similar multiphysics and multiphase problems like acoustico-fluidics, magnetohydrodynamics, thermophoresis

and electrokinetics of particles and drops to name a few.

In chapter 2, we developed a comprehensive model to study electrohydrodynamic interactions between a pair of spherical particles using method of reflections, particularly in strong electric fields where these particles are under Quincke rotation. The motivation of this work was the discrepancy between experiments and theoretical predictions observed by Lemaire and coworkers [98, 95, 112]. We demonstrated the importance of electrohydrodynamic interactions and their effect on the critical electric field required for the onset of Quincke rotation. Using numerical simulations, we solve the nonlinear governing equations and discovered complex dynamics exhibited by a pair of particles under Quincke rotation.

In chapter 3, we used the mathematical tools developed earlier and explored the effects of wall on the Quincke rotation of a particle. The spontaneous angular velocity of the Quincke particle or roller enabled it to self-propel in a random direction with Brownian diffusion. The electrohydrodynamic interaction between many such rollers gave rise to large scale correlated motion. We studied these effects using a combination of experiment, theory and simulations. This proved to be an ideal system in the emerging field of active matter primarily due to its high controllability, accurate measurement techniques and ease of manoeuvrability. The effect of confinement in ring, square and circular geometry were also discussed. In circular confinement, we discovered that the motile colloids self organise into a steadily rotating vortex that live on the verge of a phase separation.

In chapter 4 and 5, we addressed the problem of electrohydrodynamics of drops in strong electric fields using a theoretical and numerical approach, respectively. It is a classic multiphase problem best described by the Melcher-Taylor leaky dielectric

model. The most novel aspect of our work was the inclusion of the nonlinear charge convection term in the theoretical model that had been neglected by researchers in the past mostly due to convenience. We also tackled this problem using a numerical approach based on boundary element method. Our simulations were able to capture Quincke rotation of drops inaccessible by previous researchers as they either confined themselves to axisymmetric drops or neglected the charge convection term that drives this phenomena.

6.2 Directions for future work

- Particles under Quincke rotation have been shown to reduce the effective viscosity [98] and increase the apparent conductivity of these suspensions[113]. The work described in chapter 2 is a first step towards simulating many particles under Quincke rotation interacting with each other electrohydrodynamically. One can also approach the same problem in a different way by developing a continuum model of leaky dielectric particles through a Smoluchowski equation. Both discrete particle simulations and continuum approach have been used previously to model bacterial suspensions. A theoretical model will give us a physical insight into the mechanisms and allow us to obtain macroscopic properties like effective viscosity and bulk electrical conductivity of these suspensions.

- The transient small deformation theory developed in chapter 4 includes charge convection, however, only relatively weak in strength. As charge convection increases in strength one needs to include higher order multipoles both in the first and second order theory. This makes the problem more complicated owing

to the nonlinear nature of the convection term. Moreover, the theory presented in this work is only valid for axisymmetric drops. Extension to three dimensions precludes the use of Stokes streamfunction and one has to use Lamb's general solution. A theoretical model for electrohydrohydrodynamics of drops in three dimensions will be useful in analysing pair interactions between them, thereby paving the path for a dilute suspension theory.

- A natural extension of the numerical work based on boundary element method presented in chapter 5 is to study drop-drop interactions and include the effect of surfactants. There have been recent experiments with particle laden drops in electric fields that exhibit complex dynamics [109, 110, 43, 134, 41, 42]. These experiments are yet to be explained and reproduced in simulations.

Appendix A

Pair interactions

A.1 Asymptotic estimate of the steady-state angular velocity

In this Appendix, we derive an asymptotic expression for the steady-state angular velocity of two interacting spheres that are fixed in space, in the case where the spheres are co-rotating: $\mathbf{\Omega}_1 = \mathbf{\Omega}_2 = \mathbf{\Omega}$. In this case, it is also obvious by symmetry that $\mathbf{P}_1 = \mathbf{P}_2 = \mathbf{P}$. We seek an expression for the correction to the steady-state angular velocity $\Omega_0 = |\mathbf{\Omega}_0|$ and dipole moment $\mathbf{P}_0$ of an isolated sphere to account for leading-order interactions in the limit of large separation distance $R \gg 1$. The single-sphere case was solved in Sec. 2.2.1, where we obtained in dimensionless variables

$$\mathbf{P}_0 = -A_1^0 \mathbf{\Omega}_0 \times \widehat{\mathbf{z}} + A_2^0 \widehat{\mathbf{z}}, \quad \Omega_0^2 = \left(\frac{E_0}{E_c^0}\right)^2 - 1, \tag{A.1}$$

with

$$A_1^0 = \frac{\varepsilon_{21} - \sigma_{21}}{1 + \Omega_0^2}, \quad A_2^0 = \varepsilon_{21} - A_1^0. \tag{A.2}$$

When interactions are taken into account, the dipole relaxation equation (2.52) at steady state simplifies to

$$\boldsymbol{\Omega} \times (\mathbf{P} + \varepsilon_{21}\mathbf{E}_e) - (\mathbf{P} + \sigma_{21}\mathbf{E}_e) = 0, \tag{A.3}$$

where $\mathbf{E}_e = -\widehat{\mathbf{z}} + \boldsymbol{\Pi} \cdot \mathbf{P}/R^3$ is the electric field experienced by each sphere. To leading order, this can be approximated as $\mathbf{E}_e \approx -\widehat{\mathbf{z}} + \boldsymbol{\Pi} \cdot \mathbf{P}_0/R^3$, where $\mathbf{P}_0$ is given in Eq. (A.1). The dipole moment equation (A.3) can then be inverted for $\mathbf{P}$ as

$$\mathbf{P} = A_1 \left[\boldsymbol{\Omega} \times \mathbf{E}_e + (\boldsymbol{\Omega} \cdot \mathbf{E}_e)\boldsymbol{\Omega}\right] - A_2\mathbf{E}_e, \tag{A.4}$$

where A_1 and A_2 are defined as in Eq. (A.2) but with Ω_0 replaced by Ω. This expression can then be substituted into the torque balance equation (2.54), which becomes

$$\boldsymbol{\Omega} = \frac{A_1}{\mathrm{Ma}} \left[E_e^2\boldsymbol{\Omega} - (\boldsymbol{\Omega} \cdot \mathbf{E}_e)\mathbf{E}_e - (\boldsymbol{\Omega} \cdot \mathbf{E}_e)(\boldsymbol{\Omega} \times \mathbf{E}_e) + \frac{1}{R^3}(\mathbf{I} - \widehat{\mathbf{z}}\widehat{\mathbf{z}}) \cdot \boldsymbol{\Omega}_0\right], \tag{A.5}$$

where we have only kept leading-order corrections in $1/R^3$. Eq. (A.5) is a nonlinear equation for the angular velocity $\boldsymbol{\Omega}$; as in the single-sphere case, it does not admit a unique solution as the direction of rotation is indeterminate. However, it can be used to obtain an expression for the magnitude of the angular velocity. To this end, we assume an asymptotic expansion for $\boldsymbol{\Omega}$ of the form

$$\boldsymbol{\Omega} = \boldsymbol{\Omega}_0 + \frac{\boldsymbol{\alpha}}{R} + \frac{\boldsymbol{\beta}}{R^2} + \frac{\boldsymbol{\gamma}}{R^3} + O(R^{-4}), \tag{A.6}$$

where $\boldsymbol{\alpha}$, $\boldsymbol{\beta}$, and $\boldsymbol{\gamma}$ are unknown vectors. The corresponding expansion for the

magnitude of the angular velocity is also given by

$$\Omega^2 = \Omega_0^2 + \frac{1}{R}(2\boldsymbol{\Omega}_0 \cdot \boldsymbol{\alpha}) + \frac{1}{R^2}(2\boldsymbol{\Omega}_0 \cdot \boldsymbol{\beta} + \alpha^2) + \frac{2}{R^3}(\boldsymbol{\Omega}_0 \cdot \boldsymbol{\gamma} + \boldsymbol{\alpha} \cdot \boldsymbol{\beta}) + O(R^{-4}). \quad \text{(A.7)}$$

By substituting these expansions into Eq. (A.5), where care must be taken to also expand A_1 which is also a function of Ω, one can derive a hierarchical set of conditions on the unknown vectors $\boldsymbol{\alpha}$, $\boldsymbol{\beta}$, and $\boldsymbol{\gamma}$ by successively identifying terms corresponding to various powers of $1/R$. At zeroth order, we recover the solution for an isolated particle, as expected. At first, second, and third orders, the conditions obtained are:

$$O(R^{-1}): \qquad \boldsymbol{\alpha} \cdot \hat{\mathbf{z}} = 0, \quad \boldsymbol{\Omega}_0 \cdot \boldsymbol{\alpha} = 0, \quad \text{(A.8)}$$

$$O(R^{-2}): \qquad \boldsymbol{\beta} \cdot \hat{\mathbf{z}} = 0, \quad 2\boldsymbol{\Omega}_0 \cdot \boldsymbol{\beta} + \alpha^2 = 0, \quad \text{(A.9)}$$

$$O(R^{-3}): \qquad \boldsymbol{\Omega}_0 \cdot \boldsymbol{\gamma} + \boldsymbol{\alpha} \cdot \boldsymbol{\beta}$$

$$= (1 + \Omega_0^2)\left[(\boldsymbol{\Pi} : \boldsymbol{\Omega}_0\boldsymbol{\Omega}_0)/4\Omega_0^2 - \hat{\mathbf{z}} \cdot \boldsymbol{\Pi} \cdot \mathbf{P}_0\right]. \quad \text{(A.10)}$$

While these conditions are not sufficient to solve for the vectors $\boldsymbol{\alpha}$, $\boldsymbol{\beta}$, and $\boldsymbol{\gamma}$, they are sufficient to fully obtain the unknown coefficients in the expansion of Ω^2 in Eq. (A.7), which becomes:

$$\Omega^2 = \Omega_0^2 + \frac{2}{R^3}(1 + \Omega_0^2)\left(\frac{\boldsymbol{\Pi} : \boldsymbol{\Omega}_0\boldsymbol{\Omega}_0}{4\Omega_0^2} - \hat{\mathbf{z}} \cdot \boldsymbol{\Pi} \cdot \mathbf{P}_0\right) + O(R^{-4}). \quad \text{(A.11)}$$

This expression shows that electric and hydrodynamic interactions modify the angular velocity of the spheres to order $O(R^{-3})$, though the perturbation depends on the direction of rotation through $\boldsymbol{\Omega}_0$ and on the orientation of the spheres through the tensor $\boldsymbol{\Pi}$. To obtain a more general estimate for the angular velocity that does

not depend on the direction of rotation, we take an average of Eq. (A.11) over all orientations of $\mathbf{\Omega}_0$, which after algebra yields the simple expression

$$\langle \Omega^2 \rangle = \Omega_0^2 + \frac{1 + 3\cos 2\Theta}{R^3} \left[\varepsilon_{21} \left(\frac{E_0}{E_c^0} \right)^2 + (\sigma_{21} - \varepsilon_{21}) \right] + O(R^{-4}), \tag{A.12}$$

in terms of the angle $\Theta = \cos^{-1}(\widehat{\mathbf{R}} \cdot \hat{\mathbf{z}})$ between the field direction and the direction of the line of centers. While this expression was obtained for two co-rotating spheres, we show in Sec. 2.4 that it provides a very good approximation to the steady-state angular velocity in the limit of $R \gg 1$ even when the two spheres are rotating in different directions.

We also note that Eq. (A.12) can be used to provide an estimate for the critical field E_c in the presence of interactions by solving for the field value for which $\langle \Omega^2 \rangle = 0$:

$$E_c \approx E_c^0 \sqrt{\frac{(1 + 3\cos 2\Theta)(\varepsilon_{21} - \sigma_{21}) + R^3}{(1 + 3\cos 2\Theta)\varepsilon_{21} + R^3}}, \tag{A.13}$$

which can be compared to the numerical results of the linear stability analysis of Sec. 2.3 and shows excellent agreement for $R \gg 1$.

A.2 Contact algorithm

In the simulations of freely suspended spheres, particle overlap is prevented by introducing additional equal and opposite contact forces $\mathbf{F}^c = \mathbf{F}_1^c = -\mathbf{F}_2^c$ at the point of contact between the two touching particles. These forces modify both the torque and force balances on the spheres. The torque balance of Eq. (2.42) becomes,

in dimensionless form:

$$\boldsymbol{\Omega}_1 + \frac{1}{2R^3}\boldsymbol{\Pi}\cdot\boldsymbol{\Omega}_2 = \frac{1}{\mathrm{Ma}}\left[\mathbf{P}_1 \times \left(\widehat{\mathbf{z}} - \frac{1}{R^3}\boldsymbol{\Pi}\cdot\mathbf{P}_2\right) + \frac{1}{4\pi}\widehat{\mathbf{R}}\times\mathbf{F}^c\right], \quad \text{(A.14)}$$

$$\boldsymbol{\Omega}_2 + \frac{1}{2R^3}\boldsymbol{\Pi}\cdot\boldsymbol{\Omega}_1 = \frac{1}{\mathrm{Ma}}\left[\mathbf{P}_2 \times \left(\widehat{\mathbf{z}} - \frac{1}{R^3}\boldsymbol{\Pi}\cdot\mathbf{P}_1\right) + \frac{1}{4\pi}\widehat{\mathbf{R}}\times\mathbf{F}^c\right], \quad \text{(A.15)}$$

The force balances of Eqs. (2.48)–(2.49) are also modified as

$$\mathbf{U}_1 = -\frac{1}{R^2}\boldsymbol{\Omega}_2\times\widehat{\mathbf{R}} + \frac{1}{3\pi\mathrm{Ma}}(\mathbf{F}_1 + \mathbf{F}^c), \quad \text{(A.16)}$$

$$\mathbf{U}_2 = \frac{1}{R^2}\boldsymbol{\Omega}_1\times\widehat{\mathbf{R}} + \frac{1}{3\pi\mathrm{Ma}}(\mathbf{F}_2 - \mathbf{F}^c). \quad \text{(A.17)}$$

To determine the contact force, we prescribe that there be rolling without slipping between the two touching surfaces, which is expressed as

$$\mathbf{U}_1 + \boldsymbol{\Omega}_1\times\widehat{\mathbf{R}} = \mathbf{U}_2 - \boldsymbol{\Omega}_2\times\widehat{\mathbf{R}}. \quad \text{(A.18)}$$

If $\mathbf{P}_1$ and $\mathbf{P}_2$ are known, Eqs. (A.14)–(A.18) form a system of five vector equations for the five unknowns $\boldsymbol{\Omega}_1$, $\boldsymbol{\Omega}_2$, $\mathbf{U}_1$, $\mathbf{U}_2$, and $\mathbf{F}^c$. This system can be inverted analytically, yielding new expressions for $\boldsymbol{\Omega}_1$, $\boldsymbol{\Omega}_2$, $\mathbf{U}_1$ and $\mathbf{U}_2$ to be used instead of Eqs. (2.54)–(2.57) when the two particles are in contact.

Appendix B

Small deformation theory

B.1 Electric field, charge and jump in Ohmic current

The normal component and tangential components of the electric field are expressed in terms of the dipole and octupole moment as:

$$E^n_{01} = 1 + 2P_{01}, \qquad \bar{E}^n_{01} = 1 - P_{01}, \tag{B.1a}$$

$$E^n_{11} = 2P_{11} - \tfrac{6}{5} f_{12}(1 + P_{01}), \qquad \bar{E}^n_{11} = -P_{11} - \tfrac{6}{5} f_{12}(1 - 2P_{01}), \tag{B.1b}$$

$$E^n_{13} = 4P_{13} + \tfrac{6}{5} f_{12}(1 - 4P_{01}), \qquad \bar{E}^n_{13} = -3P_{13} + \tfrac{6}{5} f_{12}\left(1 + \tfrac{7}{2} P_{01}\right). \tag{B.1c}$$

$$E^t_{00} = -(1 - P_{01}), \tag{B.2a}$$

$$E^t_{10} = P_{13} + P_{11} - f_{12}(1 + 2P_{01}), \tag{B.2b}$$

$$E^t_{12} = 5P_{13} - f_{12}(2 + 7P_{01}). \tag{B.2c}$$

Substituting the expressions obtained in (B.1) into Gauss's and Ohm's law respectively, the surface charge and jump in Ohmic current are written as:

$$q_{01} = E^n_{01} - Q\bar{E}^n_{01} = 1 + 2P_{01} - Q(1 - P_{01}), \tag{B.3a}$$

$$q_{11} = E^n_{11} - Q\bar{E}^n_{11} = 2P_{11} - \tfrac{6}{5}f_{12}(1 + P_{01}) - Q[-P_{11} - \tfrac{6}{5}f_{12}(1 - 2P_{01})], \tag{B.3b}$$

$$q_{13} = E^n_{13} - Q\bar{E}^n_{13} = 4P_{13} + \tfrac{6}{5}f_{12}(1 - 4P_{01}) - Q[-3P_{13} + \tfrac{6}{5}f_{12}\left(1 + \tfrac{7}{2}P_{01}\right)]. \tag{B.3c}$$

$$[\![j]\!]^n_{01} = RE^n_{01} - \bar{E}^n_{01} = R(1 + 2P_{01}) - 1 + P_{01}, \tag{B.4a}$$

$$[\![j]\!]^n_{11} = RE^n_{11} - \bar{E}^n_{11} = R[2P_{11} - \tfrac{6}{5}f_{12}(1 + P_{01})] + P_{11} + \tfrac{6}{5}f_{12}(1 - 2P_{01}), \tag{B.4b}$$

$$[\![j]\!]^n_{13} = RE^n_{13} - \bar{E}^n_{13} = R[4P_{13} + \tfrac{6}{5}f_{12}(1 - 4P_{01})] + 3P_{13} - \tfrac{6}{5}f_{12}\left(1 + \tfrac{7}{2}P_{01}\right). \tag{B.4c}$$

The tangential electric stress coefficients in equation (4.47) are written as

$$[qE^t]_{01} = q_{01}E^t_{01}, \tag{B.5a}$$

$$[qE^t]_{11} = q_{01}E^t_{11} + \tfrac{2}{5}q_{01}E^t_{13} + q_{11}E^t_{01}, \tag{B.5b}$$

$$[qE^t]_{13} = \tfrac{3}{5}q_{01}E^t_{13} + q_{13}E^t_{01}, \tag{B.5c}$$

where the various products on the right-hand side are easily evaluated using equations (B.2) and (B.3). The electric pressure coefficients in equation (4.48) are

$$[\![p^E]\!]_{00} = \tfrac{1}{6}(E_{01}^{n2} - Q\bar{E}_{01}^{n2}) + \tfrac{1}{3}(Q-1)E_{00}^{t2}, \tag{B.6a}$$

$$[\![p^E]\!]_{02} = \tfrac{1}{3}(E_{01}^{n2} - Q\bar{E}_{01}^{n2}) - \tfrac{1}{3}(Q-1)E_{00}^{t2}, \tag{B.6b}$$

$$[\![p^E]\!]_{10} = \tfrac{1}{3}(E_{01}^{n}E_{11}^{n} - Q\bar{E}_{01}^{n}\bar{E}_{11}^{n}) + \tfrac{2}{3}E_{00}^{t}(E_{10}^{t} - \tfrac{1}{5}E_{12}^{t}), \tag{B.6c}$$

$$\begin{aligned}[\![p^E]\!]_{12} = {} & \tfrac{2}{3}(E_{01}^{n}E_{11}^{n} - Q\bar{E}_{01}^{n}\bar{E}_{11}^{n}) + \tfrac{3}{7}(E_{01}^{n}E_{13}^{n} - Q\bar{E}_{01}^{n}\bar{E}_{13}^{n}) \\ & + \tfrac{2}{3}E_{00}^{t}(\tfrac{5}{7}E_{12}^{t} - E_{10}^{t}),\end{aligned} \tag{B.6d}$$

$$[\![p^E]\!]_{14} = \tfrac{4}{7}(E_{01}^{n}E_{13}^{n} - Q\bar{E}_{01}^{n}\bar{E}_{13}^{n}) - \tfrac{12}{35}E_{00}^{t}E_{12}^{t}, \tag{B.6e}$$

and can be calculated using equations (B.1) and (B.2).

B.2 Interfacial velocity and hydrodynamic stress

The zeroth-order coefficients of the normal and tangential component of the interfacial velocity used in equation (4.43) are found to be

$$v_{02}^{n} = A_{03} + B_{03}, \qquad \bar{v}_{02}^{n} = \bar{A}_{03} + \bar{B}_{03}, \tag{B.7a}$$

$$v_{01}^{t} = A_{03}, \qquad \bar{v}_{01}^{t} = -\tfrac{3}{2}\bar{A}_{03} - \tfrac{5}{2}\bar{B}_{03}. \tag{B.7b}$$

At first order, the normal velocities read

$$v_{10}^n = -\tfrac{2}{5} f_{12}(A_{03} + B_{03}), \tag{B.8a}$$

$$v_{12}^n = A_{13} + B_{13} - \tfrac{2}{7} f_{12}(3A_{03} + 2B_{03}), \tag{B.8b}$$

$$v_{14}^n = A_{15} + B_{15} - \tfrac{12}{35} f_{12}(8A_{03} + 3B_{03}), \tag{B.8c}$$

$$\bar{v}_{10}^n = -\tfrac{2}{5} f_{12}(\bar{A}_{03} + \bar{B}_{03}), \tag{B.8d}$$

$$\bar{v}_{12}^n = \bar{A}_{13} + \bar{B}_{13} - \tfrac{1}{7} f_{12}(\bar{A}_{03} - \bar{B}_{03}), \tag{B.8e}$$

$$\bar{v}_{14}^n = \bar{A}_{15} + \bar{B}_{15} + \tfrac{6}{35} f_{12}(9\bar{A}_{03} + 19\bar{B}_{03}), \tag{B.8f}$$

whereas those of the tangential velocity are given by

$$v_{11}^t = A_{13} + \tfrac{3}{5} A_{15} + \tfrac{3}{10} B_{15} - \tfrac{2}{5} f_{12}(7A_{03} + 3B_{03}), \tag{B.9a}$$

$$v_{13}^t = \tfrac{7}{5} A_{15} + \tfrac{7}{10} B_{15} - \tfrac{3}{5} f_{12}(7A_{03} + 3B_{03}), \tag{B.9b}$$

$$\bar{v}_{11}^t = -\tfrac{3}{2} \bar{A}_{13} - \tfrac{5}{2} \bar{B}_{13} - \tfrac{3}{4} \bar{A}_{15} - \tfrac{21}{20} \bar{B}_{15} - \tfrac{3}{5} f_{12}(3\bar{A}_{03} + 7\bar{B}_{03}), \tag{B.9c}$$

$$\bar{v}_{13}^t = -\tfrac{7}{4} \bar{A}_{15} - \tfrac{49}{20} \bar{B}_{15} - \tfrac{9}{10} f_{12}(3\bar{A}_{03} + 7\bar{B}_{03}). \tag{B.9d}$$

The zeroth-order boundary conditions (4.44*a*) and (A.18*a*) provide us with the relations

$$A_{03} = -B_{03} + \delta \dot{f}_{12}, \quad \bar{A}_{03} = -B_{03} + \tfrac{7}{2} \delta \dot{f}_{12}, \quad \bar{B}_{03} = B_{03} - \tfrac{5}{2} \delta \dot{f}_{12}. \tag{B.10}$$

Using these relations together with the condition that $f_{20} = -f_{12}^2/5$ obtained in §4.3.1 from volume conservation, it is easy to show that (4.44*b*) is trivially satisfied. The remaining first-order boundary conditions then yield six additional equations that can

be combined to show that

$$A_{13} = -B_{13} - \tfrac{2}{7} f_{12} B_{03} + \delta \dot{f}_{22} + \tfrac{6}{7} \delta f_{12} \dot{f}_{12}, \tag{B.11a}$$

$$\bar{A}_{13} = -B_{13} + \tfrac{3}{7} f_{12} B_{03} + \tfrac{7}{2} \delta \dot{f}_{22} + \tfrac{1}{2} \delta f_{12} \dot{f}_{12}, \tag{B.11b}$$

$$\bar{B}_{13} = B_{13} - \tfrac{5}{7} f_{12} B_{03} - \tfrac{5}{2} \delta \dot{f}_{22} + \tfrac{5}{14} \delta f_{12} \dot{f}_{12}, \tag{B.11c}$$

$$A_{15} = -B_{15} - \tfrac{12}{7} f_{12} B_{03} + \delta \dot{f}_{24} + \tfrac{96}{35} \delta f_{12} \dot{f}_{12}, \tag{B.11d}$$

$$\bar{A}_{15} = -B_{15} - \tfrac{6}{7} f_{12} B_{03} + \tfrac{11}{2} \delta \dot{f}_{24} + \tfrac{3}{35} \delta f_{12} \dot{f}_{12}, \tag{B.11e}$$

$$\bar{B}_{15} = B_{15} - \tfrac{6}{7} f_{12} B_{03} - \tfrac{9}{2} \delta \dot{f}_{24} + \tfrac{93}{35} \delta f_{12} \dot{f}_{12}. \tag{B.11f}$$

Equations (B.10)–(B.11) therefore allow us to reduce the number of flow unknowns to three, namely B_{03}, B_{13} and B_{15}. The hydrodynamic stress is obtained by using equations (4.49). At zeroth order, we find:

$$[\![T^H]\!]^{nn}_{00} = [\![p^H]\!]_{00}, \tag{B.12a}$$

$$[\![T^H]\!]^{nn}_{02} = (2 + 3\lambda) B_{03} - \tfrac{1}{2}(16 + 19\lambda) \delta \dot{f}_{12}, \tag{B.12b}$$

$$[\![T^H]\!]^{nt}_{01} = 5(1 + \lambda) B_{03} - \tfrac{1}{2}(16 + 19\lambda) \delta \dot{f}_{12}. \tag{B.12c}$$

Similarly, at first order,

$$[\![T^H]\!]^{nn}_{10} = [\![p^H]\!]_{10} + \tfrac{2}{5}(-1+11\lambda)B_{03}f_{12} + \tfrac{1}{5}(8-43\lambda)\delta\dot{f}_{12}f_{12}, \tag{B.13a}$$

$$\begin{aligned}[\![T^H]\!]^{nn}_{12} &= (2+3\lambda)B_{13} + \tfrac{1}{7}(-8+13\lambda)B_{03}f_{12} - \tfrac{1}{2}(16+19\lambda)\delta\dot{f}_{22} \\ &\quad - \tfrac{105}{14}\lambda\,\delta f_{12}\dot{f}_{12},\end{aligned} \tag{B.13b}$$

$$\begin{aligned}[\![T^H]\!]^{nn}_{14} &= \tfrac{3}{10}(4+5\lambda)B_{15} + \tfrac{3}{35}(28+37\lambda)B_{03}f_{12} - \tfrac{3}{4}(16+17\lambda)\delta\dot{f}_{24} \\ &\quad - \tfrac{3}{70}(32+47\lambda)\delta f_{12}\dot{f}_{12},\end{aligned} \tag{B.13c}$$

$$\begin{aligned}[\![T^H]\!]^{nt}_{11} &= 5(1+\lambda)B_{13} + \tfrac{27}{10}(1+\lambda)B_{15} - \tfrac{4}{35}(33+18\lambda)B_{03}f_{12} \\ &\quad - \tfrac{1}{2}(16+19\lambda)\delta\dot{f}_{22} - \tfrac{9}{20}(16+17\lambda)\delta\dot{f}_{24} + \tfrac{2}{175}(227-466\lambda)\delta f_{12}\dot{f}_{12},\end{aligned} \tag{B.13d}$$

$$\begin{aligned}[\![T^H]\!]^{nt}_{13} &= \tfrac{63}{10}(1+\lambda)B_{15} - \tfrac{9}{5}(1+\lambda)B_{03}f_{12} - \tfrac{21}{20}(16+17\lambda)\delta\dot{f}_{24} \\ &\quad + \tfrac{9}{50}(4-7\lambda)\delta f_{12}\dot{f}_{12}.\end{aligned} \tag{B.13e}$$

In equations (B.12) and (B.13), $[\![p^H]\!]_{00}$ and $[\![p^H]\!]_{10}$ denote uniform hydrostatic pressure jumps that do no affect drop shape.

B.3 Axisymmetric boundary element method

We outline the numerical method used in §5.4 for the solution of the full nonlinear problem in axisymmetric geometry based on boundary integral equations [74, 157]. The method shares similarities with that of [90] but makes use of a finite-volume algorithm for the solution of the charge convection equation. We first solve Laplace's equation for the electric potential using a single-layer potential

[151, 10, 88, 90], yielding the integral equation

$$\varphi(\boldsymbol{x}_0) = -\boldsymbol{x}_0 \cdot \boldsymbol{E}_0 + \int_C [\![E^n(\boldsymbol{x})]\!]\, \mathcal{G}^a(\boldsymbol{x}_0; \boldsymbol{x})\, \mathrm{d}s(\boldsymbol{x}), \tag{B.14}$$

where C is the one-dimensional curve describing the drop shape, which is parametrized by arclength s. Equation (B.14) is valid for any location of the evaluation point $\boldsymbol{x}_0$ on the drop surface C or in either of the fluid domains V and $\bar{V}$. It involves the axisymmetric Green's function for Laplace's equation, which is obtained by integration of the three-dimensional free-space Green's function over the azimuthal direction:

$$\mathcal{G}^a(\boldsymbol{x}_0; \boldsymbol{x}) = \int_0^{2\pi} \frac{\mathrm{d}\phi}{4\pi r}, \qquad \text{where} \quad r = |\boldsymbol{r}| = |\boldsymbol{x}_0 - \boldsymbol{x}|. \tag{B.15}$$

Knowledge of the single-layer potential density $[\![E^n]\!]$ therefore allows determination of the electric potential anywhere in space by simple integration, which prompts us to seek an equation for $[\![E^n]\!]$ in terms of the charge density q. To this end, we first take the gradient of equation (B.14) with respect to $\boldsymbol{x}_0$ to obtain integral equations for the electric field in both fluid phases:

$$\boldsymbol{E}(\boldsymbol{x}_0) = \boldsymbol{E}_0 - \int_C [\![E^n(\boldsymbol{x})]\!] \boldsymbol{\nabla}_0 \mathcal{G}^a\, \mathrm{d}s(\boldsymbol{x}) \quad \text{for } \boldsymbol{x}_0 \in V, \tag{B.16a}$$

$$\bar{\boldsymbol{E}}(\boldsymbol{x}_0) = \boldsymbol{E}_0 - \int_C [\![E^n(\boldsymbol{x})]\!] \boldsymbol{\nabla}_0 \mathcal{G}^a\, \mathrm{d}s(\boldsymbol{x}) \quad \text{for } \boldsymbol{x}_0 \in \bar{V}. \tag{B.16b}$$

The derivative of the Green's function undergoes a discontinuity across the interface, which needs to be accounted for when the evaluation point is on the boundary [129],

leading to the following expressions on the drop surface:

$$\boldsymbol{E}(\boldsymbol{x}_0) = \boldsymbol{E}_0 - \int_C [\![E^n(\boldsymbol{x})]\!] \boldsymbol{\nabla}_0 \mathcal{G}^a \, \mathrm{d}s(\boldsymbol{x}) + \tfrac{1}{2}[\![E^n(\boldsymbol{x}_0)]\!]\boldsymbol{n}(\boldsymbol{x}_0) \quad \text{for } \boldsymbol{x}_0 \in C, \tag{B.17a}$$

$$\bar{\boldsymbol{E}}(\boldsymbol{x}_0) = \boldsymbol{E}_0 - \int_C [\![E^n(\boldsymbol{x})]\!] \boldsymbol{\nabla}_0 \mathcal{G}^a \, \mathrm{d}s(\boldsymbol{x}) - \tfrac{1}{2}[\![E^n(\boldsymbol{x}_0)]\!]\boldsymbol{n}(\boldsymbol{x}_0) \quad \text{for } \boldsymbol{x}_0 \in C. \tag{B.17b}$$

These equations are singular at $\boldsymbol{x} = \boldsymbol{x}_0$, though the singularity disappears after taking the dot product with the normal $\boldsymbol{n}(\boldsymbol{x}_0)$. An integral equation for the jump can then be obtained by summing both equations and combining them with Gauss's law (4.4), which is written $q = E^n - Q\bar{E}^n$ in dimensionless form. After manipulations, it reads

$$\int_C [\![E^n(\boldsymbol{x})]\!][\boldsymbol{n}(\boldsymbol{x}_0) \cdot \boldsymbol{\nabla}_0 \mathcal{G}^a] \mathrm{d}s(\boldsymbol{x}) - \frac{1+Q}{2(1-Q)}[\![E^n(\boldsymbol{x}_0)]\!] = E_0^n(\boldsymbol{x}_0) - \frac{q(\boldsymbol{x}_0)}{1-Q}. \tag{B.18}$$

This can be solved for $[\![E^n]\!]$, from which E^n and $\bar{E}^n$ are deduced using Gauss's law as

$$E^n = \frac{q - Q[\![E^n]\!]}{1-Q}, \qquad \bar{E}^n = \frac{q - [\![E^n]\!]}{1-Q}. \tag{B.19}$$

The tangential component of the electric field can then be obtained by evaluating equation (B.17), though care must be taken to treat the integral singularity [149]. Another approach, which we adopt here, consists in evaluating the potential φ using equation (B.14), which is only weakly singular, and then differentiating it numerically along the curve C to obtain E^t.

Once both normal and tangential components of the electric field are known, they can be used to determine the jump in electric tractions $[\![\boldsymbol{f}^E]\!]$ using equation (4.9), from which we infer the jump in hydrodynamic tractions $[\![\boldsymbol{f}^H]\!]$ using the stress balance (4.7). Hydrodynamic tractions then enter the Stokes boundary integral equation for

the fluid velocity $\boldsymbol{v}$ [127], which for an axisymmetric domain reads

$$\begin{aligned}\boldsymbol{v}(\boldsymbol{x}_0) = &-\frac{1}{4\pi Ma(1+\lambda)}\int_C [\![\boldsymbol{f}^H(\boldsymbol{x})]\!]\cdot\boldsymbol{G}^a(\boldsymbol{x};\boldsymbol{x}_0)\,\mathrm{d}s(\boldsymbol{x})\\ &+\frac{1-\lambda}{4\pi(1+\lambda)}\int_C \boldsymbol{v}(\boldsymbol{x})\cdot\boldsymbol{T}^a(\boldsymbol{x};\boldsymbol{x}_0)\cdot\boldsymbol{n}(\boldsymbol{x})\,\mathrm{d}s(\boldsymbol{x}),\end{aligned} \tag{B.20}$$

where $\boldsymbol{G}^a$ and $\boldsymbol{T}^a$ are the axisymmetric Green's functions for the Stokeslet and stresslet, respectively:

$$\boldsymbol{G}^a(\boldsymbol{x};\boldsymbol{x}_0) = \int_0^{2\pi}\left(\frac{\boldsymbol{I}}{r}+\frac{\boldsymbol{rr}}{r^3}\right)\mathrm{d}\phi, \quad \boldsymbol{T}^a(\boldsymbol{x};\boldsymbol{x}_0) = \int_0^{2\pi} -6\frac{\boldsymbol{rrr}}{r^5}\,\mathrm{d}\phi, \tag{B.21}$$

The exact expressions for these functions are very cumbersome but can be found in [127, 128]. The integral equation (B.20), which is valid in both fluid domains and on the interface, can be inverted to determine the interfacial velocity, which is then used to update the drop shape and charge distribution.

The complete algorithm can be summarized as follows:

1. Given a surface charge distribution $q(\boldsymbol{x})$, compute $[\![E^n]\!]$, E^n, and $\bar{E}^n$ by solution of the integral equation (B.18) together with equation (B.19).

2. Determine the surface potential φ by evaluation of equation (B.14).

3. Differentiate the surface potential φ numerically along the interface to obtain the tangential electric field $\boldsymbol{E}^t = -\boldsymbol{\nabla}_s\varphi$.

4. Knowing both components of the electric field, calculate the jump in electric tractions $[\![\boldsymbol{f}^E]\!]$ using equation (4.9), and use it to determine the jump in hydrodynamic tractions $[\![\boldsymbol{f}^H]\!]$ using the stress balance (4.7).

5. Solve the Stokes boundary integral equation (B.20) to obtain the interfacial velocity.

6. Update the charge distribution $q(\boldsymbol{x})$ by time marching of the charge conservation equation (5.4) using an explicit scheme.

7. Update the position of the interface by advecting the mesh with the normal component of the interfacial velocity using the same time-marching scheme as in (vi).

In all simulations, the drop shape is taken to be initially spherical, and the initial surface charge is uniformly zero. We use spline interpolation to represent the shape of the interface, which allows for an easy and accurate determination of geometric properties such as the normal and tangential vectors and surface curvature, and for accurate evaluation of surface integrals. The charge conservation equation, however, is discretized using a finite-volume scheme [97], which has better conservation properties and is also more adequate for capturing sharp gradients as arise in strong fields (figures 4.4 and 4.5); this distinguishes our method from that of [90], which uses splines for both the drop shape and surface charge distribution.

Appendix C

Boundary element method

C.1 Discrete surface parametrisation

The drop's surface is divided into $N_{\triangle}$ 6-nodes curved triangular elements that allows accurate computation of its curvature. The physical three dimensional element is mapped to a right angles isosceles triangle residing in a plane described by s_1 and s_2 coordinates. Any point on the surface $\boldsymbol{x}$ in the physical space is represent using 6 basis functions ϕ that are defined on each triangle, exact expressions of which can be found in [127, 128],

$$\boldsymbol{x} = \sum_{i=1}^{6} \boldsymbol{x}_i \phi_i(s_1, s_2), \tag{C.1}$$

where The unit tangential vectors in the directions of s_1 and s_2 in the physical space are,

$$\boldsymbol{e}_{s_1} = \sum_{i=1}^{6} \boldsymbol{x}_i \frac{\partial \phi_i}{\partial s_1}, \quad \boldsymbol{e}_{s_2} = \sum_{i=1}^{6} \boldsymbol{x}_i \frac{\partial \phi_i}{\partial s_2}. \tag{C.2}$$

The unit normal vector is given by,

$$\boldsymbol{n} = \frac{1}{h_S}\boldsymbol{e}_{s_1} \times \boldsymbol{e}_{s_2} \tag{C.3}$$

where $h_S(\xi, \eta) = |\boldsymbol{e}_{s_1} \times \boldsymbol{e}_{s_2}|$ is the surface metric. We define the metric tensor $\boldsymbol{A}$,

$$A_{ij} = \frac{\partial x_k}{\partial s_i}\frac{\partial x_k}{\partial s_j}, \tag{C.4}$$

using which the surface divergence of any surface vector $\boldsymbol{v}$ can be found as,

$$\boldsymbol{\nabla}_s \cdot \boldsymbol{v} = A_{ij}^{-1}\frac{\partial v_k}{\partial s_i}\frac{\partial x_k}{\partial s_j}. \tag{C.5}$$

We use equation (C.5) to compute the mean curvature $2\kappa_m = \boldsymbol{\nabla}_s \cdot \boldsymbol{n}$ and charge convection term $\boldsymbol{\nabla}_s \cdot (q\boldsymbol{u})$. Since these terms are computed locally at each element, the value at a global node is found by simply averaging the values at the local nodes. An alternative method of computing the surface divergence of a vector is by using Stokes theorem that enables us to find the effective curvature of each element,

$$\kappa_m = \frac{1}{2S_E}\int_{S_E} \boldsymbol{\nabla}_s \cdot \boldsymbol{v}\,\mathrm{d}S = \frac{1}{2S_E}\int_{C_E} (\boldsymbol{b} \times \boldsymbol{v})\,\mathrm{d}l \tag{C.6}$$

where, $\boldsymbol{b} = \boldsymbol{t} \times \boldsymbol{n}$ is the outward unit normal to the edges of the triangular element and S_E and C_E are the element area and contour respectively [129]. The Stokes theorem also forms the basis of the finite volume method for the charge conservation equation. We did not find any significant difference between these methods and the curvature is computed using (C.5) in this work.

C.2 Regularisation of hypersingular integral

In this section we briefly summarize the regularization of hypersingular integral that arises in the boundary integral equation for the electric field. The interior and exterior potential problems are,

$$\int_S [\varphi^-(\boldsymbol{x}) - \varphi^-(\boldsymbol{x}_0)][\boldsymbol{n}(\boldsymbol{x}) \cdot \boldsymbol{\nabla}\mathcal{G}(\boldsymbol{x};\boldsymbol{x}_0)]\,\mathrm{d}S(\boldsymbol{x}) = \int_S [\nabla\varphi \cdot \boldsymbol{n}]^-(\boldsymbol{x})\mathcal{G}(\boldsymbol{x};\boldsymbol{x}_0)\,\mathrm{d}S(\boldsymbol{x}), \tag{C.7}$$

$$\int_S [\varphi^+(\boldsymbol{x}) - \varphi^+(\boldsymbol{x}_0)][\boldsymbol{n}(\boldsymbol{x}) \cdot \boldsymbol{\nabla}\mathcal{G}(\boldsymbol{x};\boldsymbol{x}_0)]\,\mathrm{d}S(\boldsymbol{x}) - \varphi^+(\boldsymbol{x}_0) = \int_S [\nabla\varphi \cdot \boldsymbol{n}]^+(\boldsymbol{x})\mathcal{G}(\boldsymbol{x};\boldsymbol{x}_0)\,\mathrm{d}S(\boldsymbol{x}), \tag{C.8}$$

respectively, where, $\mathcal{G}(\boldsymbol{x};\boldsymbol{x}_0) = 1/(4\pi r)$ is the fundamental solution of Laplace's equation, also known as Green's function. It is evident from these integral equations that the knowledge of potential on the boundary gives us the knowledge of its normal flux and vice versa. Using continuity of potential, $\varphi^+ = \varphi^-$ and subtracting equation (C.8) from (C.7) and adding the external potential $\varphi^e = -\boldsymbol{x} \cdot \boldsymbol{E}^e$ to the resulting equation, we obtain the electric potential in terms of the normal jump in the electric field.

$$\varphi^{\pm}(\boldsymbol{x}_0) = \varphi^e(\boldsymbol{x}_0) + \int_S [\![E_n]\!](\boldsymbol{x})\mathcal{G}(\boldsymbol{x};\boldsymbol{x}_0)\,\mathrm{d}S(\boldsymbol{x}) \tag{C.9}$$

The singular integral are regularised by converting them to tangential derivatives of the potential using integral identities, details of which can be found in [149] and are omitted here for brevity. The regularized integral equations for the exterior and

interior electric field are,

$$\begin{aligned}
&\tfrac{1}{2}\boldsymbol{E}^{+}(\boldsymbol{x}_0) - [\boldsymbol{n}\boldsymbol{E}_t - \boldsymbol{E}_t\boldsymbol{n}](\boldsymbol{x}_0)\cdot\boldsymbol{L}(\boldsymbol{x}_0)\\
&+\int_S \Big\{[\boldsymbol{n}\boldsymbol{E}_t - \boldsymbol{E}_t\boldsymbol{n}](\boldsymbol{x}) - [\boldsymbol{n}\boldsymbol{E}_t - \boldsymbol{E}_t\boldsymbol{n}](\boldsymbol{x}_0)\Big\}\cdot\boldsymbol{\nabla}_0\mathcal{G}(\boldsymbol{x};\boldsymbol{x}_0)\,\mathrm{d}S(\boldsymbol{x}) \qquad \text{(C.10)}\\
&=\tfrac{1}{2}\boldsymbol{E}^{e}(\boldsymbol{x}_0) - E_n^{+}(\boldsymbol{x}_0)\boldsymbol{L}(\boldsymbol{x}_0) + \int_S \Big\{E_n^{+}(\boldsymbol{x}) - E_n^{+}(\boldsymbol{x}_0)\Big\}\,\boldsymbol{\nabla}_0\mathcal{G}(\boldsymbol{x};\boldsymbol{x}_0)\,\mathrm{d}S(\boldsymbol{x}),\\
&\tfrac{1}{2}\boldsymbol{E}^{-}(\boldsymbol{x}_0) + [\boldsymbol{n}\boldsymbol{E}_t - \boldsymbol{E}_t\boldsymbol{n}]\cdot\boldsymbol{L}(\boldsymbol{x}_0)\\
&-\int_S \Big\{[\boldsymbol{n}\boldsymbol{E}_t - \boldsymbol{E}_t\boldsymbol{n}](\boldsymbol{x}) - [\boldsymbol{n}\boldsymbol{E}_t - \boldsymbol{E}_t\boldsymbol{n}](\boldsymbol{x}_0)\Big\}\cdot\boldsymbol{\nabla}_0\mathcal{G}(\boldsymbol{x};\boldsymbol{x}_0)\,\mathrm{d}S(\boldsymbol{x}) \qquad \text{(C.11)}\\
&=\tfrac{1}{2}\boldsymbol{E}^{e}(\boldsymbol{x}_0) + E_n^{-}(\boldsymbol{x}_0)\boldsymbol{L}(\boldsymbol{x}_0) + \int_S \Big\{E_n^{-}(\boldsymbol{x}) - E_n^{-}(\boldsymbol{x}_0)\Big\}\,\boldsymbol{\nabla}_0\mathcal{G}(\boldsymbol{x};\boldsymbol{x}_0)\,\mathrm{d}S(\boldsymbol{x}).
\end{aligned}$$

where $\boldsymbol{L}$ is an integral equation containing geometrical properties of the surface,

$$\begin{aligned}
\boldsymbol{L}(\boldsymbol{x}_0) = \tfrac{1}{2}\boldsymbol{n}(\boldsymbol{x}_0) - \int_S \Big\{&[\boldsymbol{\nabla}\mathcal{G}(\boldsymbol{x};\boldsymbol{x}_0)\cdot\boldsymbol{n}(\boldsymbol{x})][\boldsymbol{n}(\boldsymbol{x}) - \boldsymbol{n}(\boldsymbol{x}_0)]\\
&+\mathcal{G}(\boldsymbol{x};\boldsymbol{x}_0)[\boldsymbol{\nabla}\cdot\boldsymbol{n}](\boldsymbol{x})\boldsymbol{n}(\boldsymbol{x})\Big\}\,\mathrm{d}S(\boldsymbol{x}).
\end{aligned} \qquad \text{(C.12)}$$

Since the tangential electric field is continuous on the surface, we can eliminate the terms involving the tangential electric field by adding the integral equations for the exterior (C.10) and interior (C.11) field.

$$\begin{aligned}
\tfrac{1}{2}[\boldsymbol{E}^{+} + \boldsymbol{E}^{-}](\boldsymbol{x}_0) =&\boldsymbol{E}^{e}(\boldsymbol{x}_0) - [\![E_n]\!](\boldsymbol{x}_0)\boldsymbol{L}(\boldsymbol{x}_0)\\
&+\int_S \{[\![E_n]\!](\boldsymbol{x}) - [\![E_n]\!](\boldsymbol{x}_0)\}\,\boldsymbol{\nabla}_0\mathcal{G}(\boldsymbol{x};\boldsymbol{x}_0)\,\mathrm{d}S(\boldsymbol{x})
\end{aligned} \qquad \text{(C.13)}$$

C.3 Weilandt's deflation technique

In this section we present Weilandt's deflation technique used for faster convergence of the iterative GMRES solver used for solving the Stokes's boundary

integral equation. The boundary integral equation for the interfacial velocity non-dimensionalized with the appropriate scales is,

$$\boldsymbol{u}(\boldsymbol{x}_0) + \frac{\lambda - 1}{8\pi} \int_S [\boldsymbol{u}(\boldsymbol{x}) - \boldsymbol{u}(\boldsymbol{x}_0)] \cdot \boldsymbol{T}(\boldsymbol{x}; \boldsymbol{x}_0) \cdot \boldsymbol{n}(\boldsymbol{x}) \, \mathrm{d}S(\boldsymbol{x}) = -\frac{1}{8\pi Ma} \int_S \Delta \boldsymbol{f}^h \cdot \boldsymbol{G}(\boldsymbol{x}; \boldsymbol{x}_0) \, \mathrm{d}S(\boldsymbol{x}). \tag{C.14}$$

Weilandt's deflation technique involves formulating a boundary integral equation in terms of the interfacial velocity, $\boldsymbol{w}$, obtained after removal of rigid body motion and uniform expansion solutions.

$$\begin{aligned} \boldsymbol{w}(\boldsymbol{x}_0) + \frac{(\lambda - 1)}{8\pi} \Big[\int_S [\boldsymbol{w}(\boldsymbol{x}) - \boldsymbol{w}(\boldsymbol{x}_0)] \cdot \boldsymbol{T}(\boldsymbol{x}; \boldsymbol{x}_0) \cdot \boldsymbol{n}(\boldsymbol{x}) \, \mathrm{d}S(\boldsymbol{x}) \\ + 4\pi \boldsymbol{w}'(\boldsymbol{x}_0) - \frac{4\pi}{S} \boldsymbol{n}(\boldsymbol{x}_0) \int_S \boldsymbol{w}(\boldsymbol{x}) \cdot \boldsymbol{n}(\boldsymbol{x}) \, \mathrm{d}S(\boldsymbol{x}) \Big] \\ = -\frac{1}{8\pi Ma} \int_S \Delta \boldsymbol{f}^h(\boldsymbol{x}) \cdot \boldsymbol{G}(\boldsymbol{x}; \boldsymbol{x}_0) \, \mathrm{d}S(\boldsymbol{x}) \end{aligned} \tag{C.15}$$

The rigid body motion $\boldsymbol{w}'$ is given by the summation of translational $\boldsymbol{U}$ and rotational $\boldsymbol{\Omega}$ velocities,

$$\boldsymbol{w}'(\boldsymbol{x}_0) = \boldsymbol{U} + \boldsymbol{\Omega} \times (\boldsymbol{x}_0 - \boldsymbol{x}_c), \tag{C.16}$$

where $\boldsymbol{x}_c$ is the surface centroid,

$$\boldsymbol{x}_c = \frac{1}{S} \int_S \boldsymbol{x} \, \mathrm{d}S(\boldsymbol{x}), \tag{C.17}$$

$$\boldsymbol{U} = \frac{1}{S} \int_S \boldsymbol{w}(\boldsymbol{x}) \, \mathrm{d}S(\boldsymbol{x}), \tag{C.18}$$

$$\boldsymbol{\Omega} = \boldsymbol{M}^{-1} \cdot \int_S (\boldsymbol{x} - \boldsymbol{x}_c) \times \boldsymbol{w}(\boldsymbol{x}) \, \mathrm{d}S(\boldsymbol{x}), \tag{C.19}$$

and the matrix $\boldsymbol{M}$ is,

$$\boldsymbol{M} = \int_S \{\boldsymbol{I}|\boldsymbol{x} - \boldsymbol{x}_c|^2 - (\boldsymbol{x} - \boldsymbol{x}_c)(\boldsymbol{x} - \boldsymbol{x}_c)\}\, \mathrm{d}S(\boldsymbol{x}). \tag{C.20}$$

Putting everything together we obtain the desired integral equation for $\boldsymbol{w}$ that we solve iteratively using GMRES,

$$\begin{aligned} &\boldsymbol{w}(\boldsymbol{x}_0) + \frac{(\lambda-1)}{8\pi}\left[\int_S [\boldsymbol{w}(\boldsymbol{x}) - \boldsymbol{w}(\boldsymbol{x}_0)] \cdot \boldsymbol{T}(\boldsymbol{x};\boldsymbol{x}_0) \cdot \boldsymbol{n}(\boldsymbol{x})\, \mathrm{d}S(\boldsymbol{x})\right. \\ &+ \frac{4\pi}{S}\int_S \boldsymbol{w}(\boldsymbol{x})\, \mathrm{d}S(\boldsymbol{x}) + 4\pi\left(\boldsymbol{M}^{-1} \cdot \int_S (\boldsymbol{x} - \boldsymbol{x}_c) \times \boldsymbol{w}(\boldsymbol{x})\, \mathrm{d}S(\boldsymbol{x})\right) \times (\boldsymbol{x}_0 - \boldsymbol{x}_c) \\ &\left. - \frac{4\pi}{S}\boldsymbol{n}(\boldsymbol{x}_0)\int_S \boldsymbol{w}(\boldsymbol{x}) \cdot \boldsymbol{n}(\boldsymbol{x})\, \mathrm{d}S(\boldsymbol{x})\right] = -\frac{1}{8\pi Ma}\int_S \Delta \boldsymbol{f}^h(\boldsymbol{x}) \cdot \boldsymbol{G}(\boldsymbol{x};\boldsymbol{x}_0)\, \mathrm{d}S(\boldsymbol{x}) \end{aligned} \tag{C.21}$$

Finally, the interfacial velocity is computed as,

$$\boldsymbol{u} = \boldsymbol{w} + \frac{\lambda - 1}{2}\boldsymbol{w}'. \tag{C.22}$$

Bibliography

[1] Abramowitz, M. & Stegun, I. A. 1972 *Handbook of Mathematical Functions: with Formulas, Graphs, and Mathematical Tables*. Dover.

[2] Ajayi, O. O. 1978 A note on Taylor's electrohydrodynamic theory. *Proc. R. Soc. Lond. A* **364**, 499–507.

[3] Albert, J. D., Comiskey, B., Jacobson, J. M., Zhang, L., Loxley, A., Feeney, R., Drzaic, P. & Morrison, I. 2000 Multi-color electrophoretic displays and materials for making the same. US Patent 6,017,584.

[4] Allan, R. S. & Mason, S. G. 1962 Particle behaviour in shear and electric fields. I. Deformation and burst of fluid drops. *Proc. R. Soc. Lond. A* **267**, 45–61.

[5] Anderson, J. L. 1985 Droplet interactions in thermocapillary motion. *Int. J. Multiphase Flow* **11**, 813–824.

[6] Bandopadhyay, A., Mandal, S., Kishore, N. K. & Chakraborty, S. 2016 Uniform electric-field-induced lateral migration of a sedimenting drop. *J. Fluid Mech.* **792**, 553–589.

[7] Bart, S. F., Tavrow, L. S., Mehregany, M. & Lang, J. H. 1990 Microfabricated electrohydrodynamic pumps. *Sens. Actuators A* **21** (1), 193–197.

[8] Basaran, O. A., Gao, H. & Bhat, P. P. 2013 Nonstandard inkjets. *Annu. Rev. Fluid Mech.* **45**, 85–113.

[9] Batchelor, G. K. 2000 *An introduction to fluid dynamics*. Cambridge university press.

[10] Baygents, J. C., Rivette, N. J. & Stone, H. A. 1998 Electrohydrodynamic deformation and interaction of drop pairs. *J. Fluid Mech.* **368**, 359–375.

[11] Baygents, J. C. & Saville, D. A. 1990 The circulation produced in a drop by an electric field: a high field strength electrokinetic model. In *In Drops & Bubbles, Third International Colloquium, Monterey 1988 (ed. T. Wang), AIP Conference Proceedings*, , vol. 197, pp. 7–17. American Institute of Physics.

[12] Bialké, J., Speck, T. & Löwen, H. 2012 Crystallization in a dense suspen-

sion of self-propelled particles. *Phys. Rev. Lett.* **108** (16), 168301.

[13] Bird, R. B. 1976 Useful non-newtonian models. *Annu. Rev. Fluid Mech.* **8** (1), 13–34.

[14] Bird, R. B., Armstrong, R. C., Hassager, O. & Curtiss, C. F. 1977 *Dynamics of polymeric liquids*. Wiley New York.

[15] Bird, R. B. & Wiest, J. M. 1995 Constitutive equations for polymeric liquids. *Annu. Rev. Fluid Mech.* **27** (1), 169–193.

[16] Bjorklund, E. 2009 The level-set method applied to droplet dynamics in the presence of an electric field. *Comput. Fluids* **38**, 358–369.

[17] Blake, J. R. & Chwang, A. T. 1974 Fundamental singularities of viscous flow. *J. Engng. Math.* **8**, 23–29.

[18] Boissy, C., Atten, P. & Foulc, J.-N. 1995 On a negative electrorheological effect. *J. Electrostat.* **35** (1), 13–20.

[19] Brazier-Smith, P. R. 1971 Stability and shape of isolated and pairs of water drops in an electric field. *Phys. Fluids* **14**, 1–6.

[20] Brazier-Smith, P. R., Jennings, S. G. & Latham, J. 1971 An investigation of the behaviour of drops and drop-pairs subjected to strong electrical forces. *Proc. R. Soc. Lond. A* **325**, 363–376.

[21] Brenner, H. 1970 Rheology of a dilute suspension of dipolar spherical particles in an external field. *J. Colloid Interface Sci.* **32** (1), 141–158.

[22] Bricard, A., Caussin, J.-B., Das, D., Savoie, C., Chikkadi, V., Shitara, K., Chepizhko, O., Peruani, F., Saintillan, D. & Bartolo, D. 2015 Emergent vortices in populations of colloidal rollers. *Nat. Commun.* **6**.

[23] Bricard, A., Caussin, J.-B., Desreumaux, N., Dauchot, O. & Bartolo, D. 2013 Emergence of macroscopic directed motion in populations of motile colloids. *Nature* **503**, 95–98.

[24] Buttinoni, I., Volpe, G., Kümmel, F., Volpe, G. & Bechinger, C. 2012 Active brownian motion tunable by light. *J. Phys. Condens. Matter* **24** (28), 284129.

[25] Castellanos, A. 2014 *Electrohydrodynamics*. Springer.

[26] Cebers, A., Lemaire, E. & Lobry, L. 2000 Internal rotations in dielectric suspensions. *Magnetohydrodynamics (N.Y.)* **36** (4), 347–364.

[27] Chen, Y., Au, J., Kazlas, P., Ritenour, A., Gates, H. & McCreary, M. 2003 Electronic paper: Flexible active-matrix electronic ink display. *Nature* **423** (6936), 136–136.

[28] Collins, R. T., Jones, J. J., Harris, M. T. & Basaran, O. A. 2008 Electrohydrodynamic tip streaming and emission of charged drops from liquid cones. *Nat. Phys.* **4** (2), 149–154.

[29] Collins, R. T., Sambath, K., Harris, M. T. & Basaran, O. A. 2013 Universal scaling laws for the disintegration of electrified drops. *Proc. Natl. Acad. Sci.* **110** (13), 4905–4910.

[30] Comiskey, B., Albert, J. D., Yoshizawa, H. & Jacobson, J. 1998 An electrophoretic ink for all-printed reflective electronic displays. *Nature* **394** (6690), 253–255.

[31] Couzin, I. D., Krause, J., James, R., Ruxton, G. D. & Franks, N. R. 2002 Collective memory and spatial sorting in animal groups. *J. Theor. Biol.* **218** (1), 1–11.

[32] Crocker, J. C. & Grier, D. G. 1996 Methods of digital video microscopy for colloidal studies. *J. Colloid Interface Sci.* **179** (1), 298–310.

[33] Darabi, J., Ohadi, M. M. & DeVoe, D. 2001 An electrohydrodynamic polarization micropump for electronic cooling. *J. Microelectromech. Syst.* **10** (1), 98–106.

[34] Das, D. 2012 Electrohydrodynamic interactions of colloidal particles undergoing quincke rotation. Master's thesis, University of Illinois at Urbana-Champaign.

[35] Das, D. & Saintillan, D. 2013 Electrohydrodynamic interaction of spherical particles under Quincke rotation. *Phys. Rev. E* **87**, 043014.

[36] Das, D. & Saintillan, D. 2016 Electrohydrodynamics of drops in strong electric fields: Numerical simulations. *J. Fluid Mech. (to be submitted)* .

[37] Das, D. & Saintillan, D. 2016 A nonlinear small-deformation theory for transient droplet electrohydrodynamics. *J. Fluid Mech. (under review)* .

[38] DeCamp, S. J., Redner, G. S., Baskaran, A., Hagan, M. F. & Dogic, Z. 2015 Orientational order of motile defects in active nematics. *Nat. Mater.* **14** (11), 1110–1115.

[39] Deseigne, J., Dauchot, O. & Chaté, H. 2010 Collective motion of vibrated polar disks. *Phys. Rev. Lett.* **105** (9), 098001.

[40] Dolinsky, Y. & Elperin, T. 2012 Dipole interaction of the quincke rotating particles. *Phys. Rev. E* **85** (2), 026608.

[41] Dommersnes, P. & Fossum, J. O. 2016 Surface structuring of particle laden drops using electric fields. *Eur. Phys. J. Special Topics* **225** (4), 715–728.

[42] Dommersnes, P., Mikkelsen, A & Fossum, J. O. 2016 Electrohydrodynamic propulsion of counter-rotating pickering drops. *Eur. Phys. J.*

Special Topics **225** (4), 699–706.

[43] Dommersnes, P., Rozynek, Z., Mikkelsen, A., Castberg, R., Kjerstad, K., Hersvik, K. & Fossum, J. O. 2013 Active structuring of colloidal armour on liquid drops. *Nat. Commun.* **4**.

[44] Dubash, N. & Mestel, A. J. 2007 Behaviour of a conducting drop in a highly viscous fluid subject to an electric field. *J. Fluid Mech.* **581**, 469–493.

[45] Dubash, N. & Mestel, A. J. 2007 Breakup behavior of a conducting drop suspended in a viscous fluid subject to an electric field. *Phys. Fluids* **19**, 072101.

[46] Dunkel, J., Heidenreich, S., Drescher, K., Wensink, H. H., Bär, M. & Goldstein, R. E. 2013 Fluid dynamics of bacterial turbulence. *Phys. Rev. Lett.* **110** (22), 228102.

[47] Einstein, A. 1911 Berichtigung zu meiner Arbeit: Eine neue Bestimmung der Moleküldimensionen. *Ann. Physik.* **339** (3), 591–592.

[48] Esmaeeli, A. & Sharifi, P. 2011 Transient electrohydrodynamics of a liquid drop. *Phys. Rev. E* **84**, 036308.

[49] Feng, J. Q. 1999 Electrohydrodynamic behaviour of a drop subjected to a steady uniform electric field at finite electric Reynolds number. *Proc. R. Soc. Lond. A* **455**, 2245–2269.

[50] Feng, J. Q. & Scott, T. C. 1996 A computational analysis of electrohydrodynamics of a leaky dielectric drop in an electric field. *J. Fluid Mech.* **311**, 289–326.

[51] Gast, A. P. & Zukoski, C. F. 1989 Electrorheological fluids as colloidal suspensions. *Adv. Colloid Interface Sci.* **30**, 153–202.

[52] Giomi, L., Hawley-Weld, N. & Mahadevan, L. 2013 Swarming, swirling and stasis in sequestered bristle-bots. *Proc. R. Soc. Lond. A* **469** (2151).

[53] Goldman, A. J., Cox, R. G. & Brenner, H. 1967 Slow viscous motion of a sphere parallel to a plane wallâĂŤi motion through a quiescent fluid. *Chem. Engng. Sci.* **22** (4), 637–651.

[54] Golestanian, R., Liverpool, T. B. & Ajdari, A. 2005 Propulsion of a molecular machine by asymmetric distribution of reaction products. *Phys. Rev. Lett.* **94** (22), 220801.

[55] Golestanian, R., Liverpool, T. B. & Ajdari, A. 2007 Designing phoretic micro-and nano-swimmers. *New J. Phys.* **9** (5), 126.

[56] Grégoire, G. & Chaté, H. 2004 Onset of collective and cohesive motion. *Phys. Rev. Lett.* **92** (2), 025702.

[57] Guazzelli, E. & Morris, J. F. 2011 *A physical introduction to suspension dynamics*. Cambridge University Press.

[58] Ha, J.-W. & Yang, S.-M. 2000 Deformation and breakup of Newtonian and non-Newtonian conducting drops in an electric field. *J. Fluid Mech.* **405**, 131–156.

[59] Ha, J.-W. & Yang, S.-M. 2000 Electrohydrodynamics and electrorotation of a drop with fluid less conductive than that of the ambient fluid. *Phys. Fluids* **12**, 764–772.

[60] Halsey, T. C. 1992 Electrorheological fluids. *Science* **258** (5083), 761–766.

[61] Halsey, T. C. & Toor, W. 1990 Structure of electrorheological fluids. *Phys. Rev. Lett.* **65** (22), 2820.

[62] Harris, F. E. & O'Konski, C. T. 1957 Dielectric properties of aqueous ionic solutions at microwave frequencies. *J. Phys. Chem.* **61**, 310–319.

[63] Haywood, R. J., Renksizbulut, M. & Raithby, G. D. 1991 Transient deformation of freely-suspended liquid droplets in electrostatic fields. *AIChE J.* **37**, 1305–1317.

[64] He, H., Salipante, P. F. & Vlahovska, P. M. 2013 Electrorotation of a viscous droplet in a uniform direct current electric field. *Phys. Fluids* **25**, 032106.

[65] Hirata, T., Kikuchi, T., Tsukada, T. & Hozawa, M. 2000 Finite element analysis of electrohydrodynamic time-dependent deformation of dielectric drop under uniform DC electric field. *J. Chem. Engng. Japan* **33**, 160–167.

[66] Howse, J. R., Jones, R. A. L., Ryan, A. J., Gough, T., Vafabakhsh, R. & Golestanian, R. 2007 Self-motile colloidal particles: from directed propulsion to random walk. *Phys. Rev. Lett.* **99** (4), 048102.

[67] Hu, C. & Shu, C.-W. 1999 Weighted essentially non-oscillatory schemes on triangular meshes. *J. Comput. Phys.* **150** (1), 97–127.

[68] Hu, W.-F., Lai, M.-C. & Young, Y.-N. 2015 A hybrid immersed boundary and immersed interface method for electrohydrodynamic simulations. *J. Comput. Phys.* **282**, 47–61.

[69] Huang, H.-F., Zahn, M. & Lemaire, E. 2010 Continuum modeling of micro-particle electrorotation in couette and poiseuille flows-The zero spin viscosity limit. *J. Electrostat.* **68** (4), 345–359.

[70] Huang, H.-F., Zahn, M. & Lemaire, E. 2011 Negative electrorheological responses of micro-polar fluids in the finite spin viscosity small spin velocity limit. I. Couette flow geometries. *J. Electrostat.* **69** (5), 442–455.

[71] Huang, Z.-M., Zhang, Y.-Z., Kotaki, M. & Ramakrishna, S. 2003

A review on polymer nanofibers by electrospinning and their applications in nanocomposites. *Compos. Sci. Technol.* **63**, 2223–2253.

[72] Jackson, J. D. 1999 *Classical electrodynamics*. Wiley.

[73] Jacobson, J. M., Drzaic, P. S., Morrison, I. D., Pullen, A. E., Wang, J., Zehner, R. W., Gray, C. L., Duthaler, G. M., McCreary, M. & Pratt, E. J. 2003 Electrophoretic displays using nanoparticles. US Patent 6,538,801.

[74] Jaswon, M. A. 1963 Integral equation methods in potential theory. I. *Proc. R. Soc. Lond. A* **275**, 23–32.

[75] Jibuti, L., Rafaï, S. & Peyla, P. 2012 Suspensions with a tunable effective viscosity: a numerical study. *J. Fluid Mech.* **693**, 345–366.

[76] Jones, Thomas B 1984 Quincke rotation of spheres. *IEEE Trans. Ind. Appl.* **IA-20** (4), 845–849.

[77] Jones, T. B. & Washizu, M. 1996 Multipolar dielectrophoretic and electrorotation theory. *J. Electrostat.* **37** (1), 121–134.

[78] Joseph, D. D. 1967 Parameter and domain dependence of eigenvalues of elliptic partial differential equations. *Arch. Ration. Mech. Anal.* **24** (5), 325–351.

[79] Karyappa, R. B., Deshmukh, S. D. & Thaokar, R. M. 2014 Breakup of a conducting drop in a uniform electric field. *J. Fluid Mech.* **754**, 550–589.

[80] Keber, F. C., Loiseau, E., Sanchez, T., DeCamp, S. J., Giomi, L., Bowick, M. J., Marchetti, M. C., Dogic, Z. & Bausch, A. R. 2014 Topology and dynamics of active nematic vesicles. *Science* **345** (6201), 1135–1139.

[81] Kennedy, M. R., Pozrikidis, C. & Skalak, R. 1994 Motion and deformation of liquid drops, and the rheology of dilute emulsions in simple shear flow. *Comput. & Fluids* **23**, 251–278.

[82] Kim, S. & Karrila, S. J. 2013 *Microhydrodynamics: Principles and Selected Applications*. Dover.

[83] Koehler, S., Schaller, V. & Bausch, A. R. 2011 Collective dynamics of active cytoskeletal networks. *PloS ONE* **6** (8), e23798.

[84] Krause, S. & Chandratreya, P. 1998 Electrorotation of deformable fluid droplets. *J. Colloid Interface Sci.* **206** (1), 10–18.

[85] Kudrolli, A., Lumay, G., Volfson, D. & Tsimring, L. S. 2008 Swarming and swirling in self-propelled polar granular rods. *Phys. Rev. Lett.* **100** (5), 058001.

[86] Kumar, A., Khusid, B., Qiu, Z. & Acrivos, A. 2005 New electric-field-driven mesoscale phase transitions in polarized suspensions. *Phys. Rev. Lett.* **95** (25), 258301.

[87] Kundu, P. K. & Cohen, I. M. 2008 *Fluid Mechanics*. 4th edn. Academic.

[88] Lac, E. & Homsy, G. M. 2007 Axisymmetric deformation and stability of a viscous drop in a steady electric field. *J. Fluid Mech.* **590**, 239–264.

[89] Lanauze, J. A., Walker, L. M. & Khair, A. S. 2013 The influence of inertia and charge relaxation on electrohydrodynamic drop deformation. *Phys. Fluids* **25**, 112101.

[90] Lanauze, J. A., Walker, L. M. & Khair, A. S. 2015 Nonlinear electrohydrodynamics of slightly deformed oblate drops. *J. Fluid Mech.* **774**, 245–266.

[91] Landau, L. D., Lifshitz, E. M. & Pitaevskiĭ, L. P. 1984 *Electrodynamics of continuous media*. Elsevier.

[92] Laser, D. J. & Santiago, J. G. 2004 A review of micropumps. *J. Micromech. Microengng.* **14**, R35.

[93] Lauga, Eric 2016 Bacterial hydrodynamics. *Annu. Rev. Fluid Mech.* **48** (1), 105–130.

[94] Lemaire, E. & Lobry, L. 2002 Chaotic behavior in electro-rotation. *Physica A* **314** (1), 663–671.

[95] Lemaire, E., Lobry, L. & Pannacci, N. 2006 Flow rate increased by electrorotation in a capillary. *J. Electrostat.* **64** (7), 586–590.

[96] Lemaire, E., Lobry, L., Pannacci, N. & Peters, F. 2008 Viscosity of an electro-rheological suspension with internal rotations. *J. Rheol.* **52** (3), 769–783.

[97] LeVeque, R. J. 2002 *Finite Volume Methods for Hyperbolic Problems*. Cambridge University Press.

[98] Lobry, L. & Lemaire, E. 1999 Viscosity decrease induced by a DC electric field in a suspension. *J. Electrostat.* **47** (1), 61–69.

[99] Loewenberg, M. & Hinch, E. J. 1996 Numerical simulation of a concentrated emulsion in shear flow. *J. Fluid Mech.* **321**, 395–419.

[100] López-Herrera, J. M., Popinet, S. & Herrada, M. A. 2011 A charge-conservative approach for simulating electrohydrodynamic two-phase flows using volume-of-fluid. *J. Comput. Phys.* **230**, 1939–1955.

[101] Lorenz, E. N. 1963 Deterministic nonperiodic flow. *J. Atmos. Sci.* **20** (2), 130–141.

[102] Marchetti, M. C., Joanny, J. F., Ramaswamy, S., Liverpool, T. B., Prost, J., Rao, M. & Simha, R. A. 2013 Hydrodynamics of soft active matter. *Rev. Mod. Phys.* **85** (3), 1143.

[103] Melcher, J. R. & Taylor, G. I. 1969 Electrohydrodynamics: a review of the role of interfacial shear stresses. *Annu. Rev. Fluid Mech.* **1**, 111–146.

[104] Miksis, M. J. 1981 Shape of a drop in an electric field. *Phys. Fluids* **24**, 1967–1972.

[105] Moriya, S., Adachi, K. & Kotaka, T. 1986 Deformation of droplets suspended in viscous media in an electric field. I. Rate of deformation. *Langmuir* **2**, 155–160.

[106] Niu, X., Liu, L., Wen, W. & Sheng, P. 2006 Hybrid approach to high-frequency microfluidic mixing. *Phys. Rev. Lett.* **97** (4), 044501.

[107] Niu, X., Wen, W. & Lee, Y.-K. 2005 Electrorheological-fluid-based microvalves. *Appl. Phys. Lett.* **87** (24), 243501.

[108] O'Konski, C. T. & Thacher, H. C. 1953 The distortion of aerosol droplets by an electric field. *J. Phys. Chem.* **57**, 955–958.

[109] Ouriemi, M. & Vlahovska, P. M. 2014 Electrohydrodynamics of particle-covered drops. *J. Fluid Mech.* **751**, 106–120.

[110] Ouriemi, M. & Vlahovska, P. M. 2015 Electrohydrodynamic deformation and rotation of a particle-coated drop. *Langmuir* **31** (23), 6298–6305.

[111] Palacci, J., Sacanna, S., Steinberg, A. P., Pine, D. J. & Chaikin, P. M. 2013 Living crystals of light-activated colloidal surfers. *Science* **339** (6122), 936–940.

[112] Pannacci, N., Lemaire, E. & Lobry, L. 2007 Rheology and structure of a suspension of particles subjected to Quincke rotation. *Rheol. Acta* **46** (7), 899–904.

[113] Pannacci, N., Lobry, L. & Lemaire, E. 2007 How insulating particles increase the conductivity of a suspension. *Phys. Rev. Lett.* **99** (9), 094503.

[114] Panton, R. L. 2006 *Incompressible flow*. Wiley.

[115] Park, J. S. & Saintillan, D. 2010 Dipolophoresis in large-scale suspensions of ideally polarizable spheres. *J. Fluid Mech.* **662**, 66–90.

[116] Park, J. S. & Saintillan, D. 2011 Electric-field-induced ordering and pattern formation in colloidal suspensions. *Phys. Rev. E* **83** (4), 041409.

[117] Park, J. S. & Saintillan, D. 2011 From diffusive motion to local aggregation: Effect of surface contamination in dipolophoresis. *Soft Matter* **7** (22), 10720–

10727.

[118] Park, J.-U., Hardy, M., Kang, S. J., Barton, K., Adair, K., Mukhopadhyay, D. K., Lee, C. Y., Strano, M. S., Alleyne, A. G., Georgiadis, J. G., Ferreira, P. M. & Rogers, J. A. 2007 High-resolution electrohydrodynamic jet printing. *Nat. Mater.* **6**, 782–789.

[119] Parthasarathy, M. & Klingenberg, D. J. 1996 Electrorheology: mechanisms and models. *Mater. Sci. Eng.* **17** (2), 57–103.

[120] Pascall, A., Sullivan, K. T. & Kuntz, J. D. 2012 Morphology of electrophoretically deposited films on electrode strips. *J. Phys. Chem. B* .

[121] Paxton, W. F., Kistler, K. C., Olmeda, C. C., Sen, A., St. Angelo, S. K., Cao, Y., Mallouk, T. E., Lammert, P. E. & Crespi, V. H. 2004 Catalytic nanomotors: autonomous movement of striped nanorods. *J. Am. Chem. Soc.* **126** (41), 13424–13431.

[122] Pearce, D. J. G., Miller, A. M., Rowlands, G. & Turner, M. S. 2014 Role of projection in the control of bird flocks. *Proc. Natl. Acad. Sci.* **111** (29), 10422–10426.

[123] Pelekasis, N. A., Tsamopoulos, J. A. & Manolis, G. D. 1990 Equilibrium shapes and stability of charged and conducting drops. *Phys. Fluids* **2** (8), 1328–1340.

[124] Peters, F. & Lobry, L.and Lemaire, E. 2005 Experimental observation of Lorenz chaos in the Quincke rotor dynamics. *Chaos* **15** (1), 013102.

[125] Peters, F., Lobry, L. & Lemaire, E. 2010 Pressure-driven flow of a micro-polar fluid: measurement of the velocity profile. *J. Rheol.* **54** (2), 311–325.

[126] Pohl, H. A. & Crane, J. S. 1971 Dielectrophoresis of cells. *Biophys. J.* **11** (9), 711.

[127] Pozrikidis, C. 1992 *Boundary Integral and Singularity Methods for Linearized Viscous Flow*. Cambridge University Press.

[128] Pozrikidis, C. 2002 *A Practical Guide to Boundary Element Methods with the Software Library BEMLIB*. CRC Press.

[129] Pozrikidis, C. 2011 *Introduction to Theoretical and Computational Fluid Dynamics*. Oxford University Press.

[130] Quincke, G. 1896 Ueber rotationen im constanten electrischen felde. *Ann. Phys. Chem.* **59**, 417.

[131] Rallison, J. M. 1984 The deformation of small viscous drops and bubbles in shear flows. *Annu. Rev. Fluid Mech.* **16**, 45–66.

[132] Rallison, J. M. & Acrivos, A. 1978 A numerical study of the deformation and burst of a viscous drop in an extensional flow. *J. Fluid Mech.* **89**, 191–200.

[133] Richter, A. & Sandmaier, H. 1990 An electrohydrodynamic micropump. In *Proceedings of micro electro mechanical systems*, pp. 99–104. IEEE.

[134] Rozynek, Z., Mikkelsen, A., Dommersnes, P. & Fossum, J. O. 2014 Electroformation of janus and patchy capsules. *Nat. Commun.* **5**.

[135] Rutledge, G. C. & Fridrikh, S. V. 2007 Formation of fibers by electrospinning. *Adv. Drug Delivery Rev.* **59** (14), 1384–1391.

[136] Saad, Y. & Schultz, M. H. 1986 GMRES: A generalized minimal residual algorithm for solving nonsymmetric linear systems. *SIAM J. Sci. Stat. Comput.* **7**, 856–869.

[137] Saintillan, D. 2008 Nonlinear interactions in electrophoresis of ideally polarizable particles. *Phys. Fluids* **20** (6), 067104.

[138] Saintillan, D. & Shelley, M. J. 2008 Instabilities, pattern formation, and mixing in active suspensions. *Phys. Fluids* **20** (12), 123304.

[139] Saintillan, D. & Shelley, M. J. 2008 Instabilities, pattern formation, and mixing in active suspensions. *Phys. Fluids* **20**, 123304.

[140] Saintillan, D. & Shelley, M. J. 2013 Active suspensions and their nonlinear models. *C. R. Physique* **14** (6), 497–517.

[141] Salipante, P. F. & Vlahovska, P. M. 2010 Electrohydrodynamics of drops in strong uniform dc electric fields. *Phys. Fluids* **22**, 112110.

[142] Salipante, P. F. & Vlahovska, P. M. 2013 Electrohydrodynamic rotations of a viscous droplet. *Phys. Rev. E* **88**, 043003.

[143] Sanchez, T., Chen, D. T. N., DeCamp, S. J., Heymann, M. & Dogic, Z. 2012 Spontaneous motion in hierarchically assembled active matter. *Nature* **491** (7424), 431–434.

[144] Sato, H., Kaji, N., Mochizuki, T. & Mori, Y. H. 2006 Behavior of oblately deformed droplets in an immiscible dielectric liquid under a steady and uniform electric field. *Phys. Fluids* **18**, 127101.

[145] Saville, D. A. 1997 Electrohydrodynamics: the Taylor-Melcher leaky dielectric model. *Annu. Rev. Fluid Mech.* **29**, 27–64.

[146] Schaller, V., Weber, C., Semmrich, C., Frey, E. & Bausch, A. R. 2010 Polar patterns of driven filaments. *Nature* **467** (7311), 73–77.

[147] Schnitzer, O. & Yariv, E. 2015 The Taylor-Melcher leaky dielectric model as a macroscale electrokinetic description. *J. Fluid Mech.* **773**, 1–33.

[148] Scott, T. C. 1989 Use of electric fields in solvent extraction: a review and prospectus. *Sep. Purif. Meth.* **18**, 65–109.

[149] Sellier, A. 2006 On the computation of the derivatives of potentials on a boundary by using boundary-integral equations. *Comput. Methods Appl. Mech. Eng.* **196**, 489–501.

[150] Sheng, P. & Wen, W. 2012 Electrorheological fluids: mechanisms, dynamics, and microfluidics applications. *Annu. Rev. Fluid Mech.* **44**, 143–174.

[151] Sherwood, J. D. 1988 Breakup of fluid droplets in electric and magnetic fields. *J. Fluid Mech.* **188**, 133–146.

[152] Shimada, K. & Fujita, T. 2000 A device to regulate rotational speed using a rotating regulator with electrorheological fluid. *Exp. Mech.* **40** (2), 231–240.

[153] Shkadov, V. Y. & Shutov, A. A. 2002 Drop and bubble deformation in an electric field. *Fluid Dyn.* **37**, 713–724.

[154] Shutov, A. A. 2002 The shape of a drop in a constant electric field. *Tech. Phys.* **47**, 1501–1508.

[155] Stanway, R., Sproston, J. L. & El-Wahed, A. K. 1996 Applications of electro-rheological fluids in vibration control: a survey. *Smart Mater. Struct.* **5** (4), 464.

[156] Supeene, G., Koch, C. R. & Bhattacharjee, S. 2008 Deformation of a droplet in an electric field: Nonlinear transient response in perfect and leaky dielectric media. *J. Colloid Interface Sci.* **318**, 463–476.

[157] Symm, G. T. 1963 Integral equation methods in potential theory. II. *Proc. R. Soc. Lond. A* **275**, 33–46.

[158] Taylor, G. I. 1964 Disintegration of water drops in an electric field. *Proc. R. Soc. Lond. A* **280**, 383–397.

[159] Taylor, G. I. 1966 Studies in electrohydrodynamics. I. The circulation produced in a drop by electrical field. *Proc. R. Soc. Lond. A* **291**, 159–166.

[160] Taylor, G. I. 1969 Electrically driven jets. *Proc. R. Soc. Lond. A* **313**, 453–475.

[161] Toner, J., Tu, Y. & Ramaswamy, S. 2005 Hydrodynamics and phases of flocks. *Ann. Phys.* **318** (1), 170–244.

[162] Torza, S., Cox, R. G. & Mason, S. G. 1971 Electrohydrodynamic deformation and burst of liquid drops. *Phil. Trans. R. Soc. Lond. A* **269**, 295–319.

[163] Tsamopoulos, J .A., Akylas, T. R. & Brown, R. A. 1985 Dynamics of charged drop break-up. *Proc. R. Soc. Lond. A* **401** (1820), 67–88.

[164] Tsebers, A. O. 1980 Internal rotation in the hydrodynamics of weakly conducting dielectric suspensions. *Fluid Dynamics* **15** (2), 245–251.

[165] Tsukada, T., Katayama, T., Ito, Y. & Hozawa, M. 1993 Theoretical and experimental studies of circulations inside and outside a deformed drop under a uniform electric field. *J. Chem. Engng. Japan* **26** (6), 698–703.

[166] Vicsek, T., Czirók, A., Ben-Jacob, E., Cohen, I. & Shochet, O. 1995 Novel type of phase transition in a system of self-driven particles. *Phys. Rev. Lett.* **75** (6), 1226.

[167] Vizika, O & Saville, D. A. 1992 The electrohydrodynamic deformation of drops suspended in liquids in steady and oscillatory electric fields. *J. Fluid Mech.* **239**, 1–21.

[168] Wan, J. T. K., Yu, K. W. & Gu, G. Q. 2000 Dynamic electrorheological effects and interparticle force between a pair of rotating spheres. *Phys. Rev. E.* **62** (5), 6846.

[169] Wang, L., Zhang, M., Li, J., Gong, X. & Wen, W. 2010 Logic control of microfluidics with smart colloid. *Lab Chip* **10** (21), 2869–2874.

[170] Washizu, M. 1993 Precise calculation of dielectrophoretic force in arbitrary field. *J. Electrostat.* **29** (2), 177–188.

[171] Weiler, W. 1893 Zur darstellung elektrischer kraftlinien. *Z. Phys. Chem. Unterricht* **4** (194).

[172] Wilson, C. T. R. & Taylor, G. I. 1925 The bursting of soap-bubbles in a uniform electric field. *Math. Proc. Cambridge Philos. Soc.* **22**, 728–730.

[173] Wioland, H., Woodhouse, F. G., Dunkel, J., Kessler, J. O. & Goldstein, R. E. 2013 Confinement stabilizes a bacterial suspension into a spiral vortex. *Phys. Rev. Lett.* **110** (26), 268102.

[174] Woodhouse, F. G. & Goldstein, R. E. 2013 Cytoplasmic streaming in plant cells emerges naturally by microfilament self-organization. *Proc. Natl. Acad. Sci.* **110** (35), 14132–14137.

[175] Xie, J., Li, X. & Xia, Y. 2008 Putting electrospun nanofibers to work for biomedical research. *Macromol. Rapid Commun.* **29** (22), 1775–1792.

[176] Yariv, Ehud & Frankel, Itzchak 2016 Electrohydrodynamic rotation of drops at large electric reynolds numbers. *J. Fluid Mech.* **788**, R2.

[177] Yon, S. & Pozrikidis, C. 1998 A finite-volume/boundary-element method for flow past interfaces in the presence of surfactants, with application to shear flow past a viscous drop. *Comput. & Fluids* **27**, 879–902.

[178] Yoshida, K., Kikuchi, M., Park, J.-H. & Yokota, S. 2002 Fabrication of

micro electro-rheological valves (er valves) by micromachining and experiments. *Sens. Actuators A* **95** (2), 227–233.

[179] Zhang, J., Zahn, J. D. & Lin, H. 2013 Transient solution for droplet deformation under electric fields. *Phys. Rev. E* **87**, 043008.

[180] Zinchenko, A. Z. & Davis, R. H. 2000 An efficient algorithm for hydrodynamical interaction of many deformable drops. *J. Comput. Phys.* **157** (2), 539–587.

[181] Zinchenko, A. Z., Rother, M. A. & Davis, R. H. 1997 A novel boundary-integral algorithm for viscous interaction of deformable drops. *Phys. Fluids* **9**, 1493–1511.